UNIVERSITY OF CALIFORNIA

Los Angeles

Observing the Feedback from Embedded Super Star Clusters with NIRSPEC

A dissertation submitted in partial satisfaction

of the requirements for the degree

Doctor of Philosophy in Astronomy and Astrophysics

by

Daniel Parke Cohen

2020

ABSTRACT OF THE DISSERTATION

Observing the Feedback from Embedded Super Star Clusters with NIRSPEC

by

Daniel Parke Cohen
Doctor of Philosophy in Astronomy and Astrophysics
University of California, Los Angeles, 2020
Professor Jean L. Turner, Chair

As the birth places of super star clusters (SSCs), starbursts provide a testbed of astrophysics on a vast range of scales, from the microphysics of star formation to the macrophysics describing the evolution of galaxies and ultimately the Universe as a whole. SSCs represent the dominant mode of star formation in the early Universe. In the local Universe, these $\sim$1-10 Myr old systems host dense concentrations of thousands of massive stars, offering an unprecedented view of the likely progenitors of globular clusters. This dissertation investigates the influence of SSCs on the gas that they ionize and subsequent effect of their starbursts on the galaxies in which they form. In particular, I explore the following questions: how does massive star feedback clear natal gas from SSCs? What conditions allow a cluster to remain bound through this gas dispersal phase or form multiple generations of stars? Through what mechanisms do starbursts regulate the central mass evolution of disk galaxies? How do SSCs drive chemically enriched, galaxy-scale winds from starbursts? To study the launching of winds, we need tracers that can penetrate the dusty clouds around young SSCs, and both high spatial and spectral resolution. The Brackett α line (4.05μm) is ideal, but not available to most observers. Using NIRSPEC (Keck II) we can map Br α and probe the dynamics of heavily embedded H II regions near SSCs. In this thesis, we present NIRSPEC observations in a variety of starburst environments, with the aim of providing an empirical basis for the emerging paradigm in the formation of the most massive stellar systems.

The dissertation of Daniel Parke Cohen is approved.

James E. Larkin

Mark R. Morris

Matthew A. Malkan

Jean L. Turner, Committee Chair

University of California, Los Angeles

2020

“For small creatures such as we the vastness is bearable only through love.”

– Carl Sagan

TABLE OF CONTENTS

LIST OF FIGURES

LIST OF TABLES

ACKNOWLEDGMENTS

This dissertation would not have been possible without the people in my life who share their love, support, and joyful curiosity. Scientific research is built around embracing uncertainty and ignorance, a perspective that gives much meaning to life. However the ego can often misinterpret uncertainty as inability. I would like to acknowledge the people who believed in me and helped me believe in myself and my scientific contributions.

I would like to thank my family. My parents have always given me the confidence and freedom to explore my curiosity, shaping my love and appreciation for the natural world. Dad, you instilled the importance and unique joy of scientific discovery – a feat all parents should aspire to. Frank, you are a gifted story-teller and are by far the most creative person I know – I've drawn from your strengths in this dissertation and continue to draw from them in my approach to life. Sammy, you were a daily source of support and emotional guidance throughout graduate school, and your empathy and vulnerability continue to inspire me every day.

I would like to thank my advisor Jean Turner. You bring a creativity and joy to science which served as constant inspiration for this dissertation, while simultaneously providing constant personal support. Your mentorship shaped me into a scientist, giving me the open-minded self-confidence to seek new scientific discovery.

Lastly, I'd like to acknowledge the UCLA graduate students – particularly those in my class. My journey through graduate school was shared and my education collaborative. Even as the pandemic hit earlier this year, you were a network of constant support. Thank you for giving true meaning to this degree.

The data presented herein were obtained at the W. M. Keck Observatory, which is operated as a scientific partnership among the California Institute of Technology, the University of California, and the National Aeronautics and Space Administration. The observatory was made possible by the generous financial support of the W. M. Keck Foundation. The authors wish to recognize and acknowledge the very significant cultural role and reverence that the summit of Maunakea

has always had within the indigenous Hawaiian community. We are most fortunate to have the opportunity to conduct observations from this mountain.

Chapter 2 of this dissertation is a version of Cohen et al. (2018) and is reproduced by permission of the AAS. This work was supported in part by National Science Foundation Astronomical Sciences Grant 15155070 awarded to JLT. The authors thank the anonymous referee for valuable discussion and recommendations for the manuscript.

Chapter 3 of this dissertation is a version of Cohen et al. (2020) and is reproduced by permission of Oxford University Press. This work was supported in part by National Science Foundation Astronomical Sciences Grant 15155070 awarded to JLT. DC was additionally supported by the UCLA Dissertation Year Fellowship. The authors thank the anonymous referee for valuable discussion and recommendations for the manuscript.

Chapter 4 of this dissertation is a version of a soon-to-be published article based off of data acquired through W.M. Keck Observatory proposal 2017B_U048. This work was supported in part by National Science Foundation Astronomical Sciences Grant 2006433 awarded to JLT. DC was additionally supported by the UCLA Dissertation Year Fellowship.

Chapter 5 of this dissertation is a version of a soon-to-be published article based off of data acquired through W.M. Keck Observatory proposal 2017B_U048. This work was supported in part by National Science Foundation Astronomical Sciences Grant 2006433 awarded to JLT. DC was additionally supported by the UCLA Dissertation Year Fellowship.

Chapter 6 is a version of an article in-preparation based off of data acquired through W.M. Keck Observatory proposal 2019B_U197. This work was supported in part by National Science Foundation Astronomical Sciences Grant 2006433 awarded to JLT. DC was additionally supported by the UCLA Dissertation Year Fellowship.

VITA

2013	Bachelor of Arts, Physics and Bachelor of Arts, Astrophysics, University of California, Berkeley.
2016	Masters of Science, Astronomy, University of California, Los Angeles.
2014-2020	Graduate Student Researcher, Department of Physics and Astronomy, University of California, Los Angeles.
2019-2020	Dissertation Year Fellowship, University of California, Los Angeles.

PUBLICATIONS AND PRESENTATIONS

Ionized Gas Motions and the Structure of Feedback near a Forming Globular Cluster in NGC 5253. Cohen, D. P. et al., 2018, ApJ, 860, 47

Unveiling kinematic structure in the starburst heart of NGC 253. D. P. et al., 2020, MNRAS, 493, 627

The Subarcsecond Structure of Feedback Near a Forming Globular Cluster: An AO View of the Supernebula in NGC 5253 with NIRSPEC. Cohen, D. P. et al., Astrophysical Frontiers in the Next Decade and Beyond: Planets, Galaxies, Black Holes, and the Transient Universe, Poster, Portland, OR, June 2018.

Unveiling a Starburst's Kinematic Structure with NIRSPEC: Ionized Gas Motions in the Nucleus of NGC 253. Cohen, D. P. et al., Keck Science Meeting, Poster, UCLA, Los Angeles, CA, September 2019.

CHAPTER 1

Introduction

Giant star clusters have played a fundamental role in shaping the baryon cycle and evolution of galaxies across all of cosmic time(e.g., Lada & Lada 2003; Portegies Zwart et al. 2010). Our own Galaxy hosts a swarm of $\sim$150 ancient globular clusters (GCs) old enough to comprise the first generation of Galactic stars (e.g., Harris 1996; Marín-Franch et al. 2009). In the earliest stages of their lives, the most massive clusters harbor tightly packed multitudes of massive stars which can provide a significant source of energy in the form of radiation, stellar winds and supernovae, potentially leading to the formation of superwinds and regulation of star formation across entire galaxies. GCs in the early Universe are even thought to significantly contribute to reionization of the IGM at $z > 6$ (e.g., He et al. 2020).

The only observable young clusters of comparable mass to GCs, $M \gtrsim 10^5$ $M_\odot$, are extragalactic super star clusters (SSCs) found within starbursts in the local Universe (Turner 2009; Consiglio 2018). Of particular interest are SSCs that are still embedded in their molecular clouds and thus opaque to visible light. Little is known about this "gas-clearing" phase, including how a massive cluster can not only remain bound but also continue to form multiple generations of stars while gas is dispersed by feedback from massive stars. The disruptive influence of individual Galactic O stars has been well-established through observations of stellar winds accelerated to thousands of km s^{-1} and expanding H II regions that will dissolve molecular birth clouds within timescales of a few Myr. Moreover, superwinds extending well over a kpc are observed to be nearly ubiquitous in starburst galaxies. How then may a collection of thousands of O stars within a few parsecs fail to dissolve its cluster or parent cluster-forming cloud?

Within the past few years, simulations of forming SSCs have converged on the notion that gas clearing fundamentally differs for the densest, most massive clusters (GC progenitors). Gas pres-

sure appears to be the distinguishing factor: the dense cores of the most massive clusters form out of highly pressurized gas, which prevents expansion and merging of ionized wind regions around individual massive stars (e.g., Silich & Tenorio-Tagle 2017, 2018; Krause et al. 2016). Rather, the shocked stellar winds in such environments lose energy through radiative cooling and remain trapped within the cluster's potential (Silich & Tenorio-Tagle 2018). With a newly established and quickly evolving theoretical framework of the mechanisms of massive cluster formation, direct observation of the dynamical influence of SSCs is extremely prescient.

My dissertation investigates the kinematic state of ionized gas near embedded SSCs using high-resolution spectroscopy at IR wavelengths obtained with NIRSPEC on Keck II. The goal is to provide some of the first direct observations of feedback from embedded SSCs on individual cluster scales, and use such observations to constrain the latest models of SSCs. The target SSCs are forming in a variety of environments within the local Universe, from blue compact dwarf galaxies (Ch. 2 and 4) to massive, gas-rich barred spiral galaxies (Ch. 3, 5, and 6). What does the real Universe have to say about the emerging paradigm of massive cluster formation and its importance in shaping galaxies?

CHAPTER 2

Ionized Gas Motions and the Structure of Feedback Near a Forming Globular Cluster in NGC 5253

This chapter presents a paper that has already been published on feedback near a SSC in NGC 5253 (Cohen et al. 2018), star formation that appears to be fed by an inflowing circumgalactic filament.

We observed Brackett α 4.05μm emission towards the supernebula in NGC 5253 with NIRSPEC on Keck II in adaptive optics mode, NIRSPAO, to probe feedback from its exciting embedded super star cluster (SSC). NIRSPEC's Slit-Viewing Camera was simultaneously used to image the K-band continuum at $\sim$0$''$.1 resolution. We register the IR continuum with HST imaging, and find that the visible clusters are offset from the K-band peak, which coincides with the Br α peak of the supernebula and its associated molecular cloud. The spectra of the supernebula exhibit Br α emission with a strong, narrow core. The linewidths are 65–76 km s^{-1}, FWHM, comparable to those around individual ultra-compact H II regions within our Galaxy. A weak, broad (FWHM$\simeq$150-175 km s^{-1}) component is detected on the base of the line, which could trace a population of sources with high-velocity winds. The core velocity of Br α emission shifts by +13 km s^{-1} from NE to SW across the supernebula, possibly indicating a bipolar outflow from an embedded object, or linked to a foreground redshifted gas filament. The results can be explained if the supernebula comprises thousands of ionized wind regions around individual massive stars, stalled in their expansion due to critical radiative cooling and unable to merge to drive a coherent cluster wind. Based on the absence of an outflow with large mass loss, we conclude that feedback is currently ineffective at dispersing gas, and the SSC retains enriched material out of which it may continue to form stars.

2.1 Introduction

Massive star clusters are fundamental components of galactic evolution. Details of gas retention or expulsion during cluster formation must be reconciled with the existence of long-lived massive clusters, globular clusters (GCs), and with multiple stellar populations observed in the GCs (Piotto et al. 2015; Silich & Tenorio-Tagle 2017). Massive clusters contain concentrations of the most massive stars (Kroupa & Boily 2002; Kroupa et al. 2013), whose evolution can potentially induce great radiative, dynamical, and chemical changes in their host galaxies. To probe the formation of GCs, we can utilize observations of local protoglobular cluster candidates, super star clusters (SSCs). They can be as young as ∼1-10 Myr (e.g., Turner 2009).

One of the most thoroughly studied forming GCs is the compact radio/IR nebula, the "supernebula", in the dwarf starburst galaxy NGC 5253. First discovered in the radio from its compact, thermal free-free emission (Beck et al. 1996), this giant H II region (Beck et al. 1996; Calzetti 1997; Turner et al. 1998) is powered by a massive SSC ($M_{vir} = 2.5 \times 10^5$ M$_\odot$) with $L \sim 5 \times 10^8$ $L_\odot$ and ∼2000 O stars (Turner et al. 2000; Meier et al. 2002; Turner et al. 2003; Vanzi & Sauvage 2004; Hunt et al. 2005; Calzetti et al. 2015; Smith et al. 2016; Turner et al. 2017). The supernebula may be part of the core of a larger star-forming region containing 4000-7000 O stars (Meier et al. 2002). What we refer to as the supernebula is its ∼3 pc core (Turner & Beck 2004; Bendo et al. 2017; Consiglio et al. 2017).

The supernebula is still deeply embedded within its natal cloud. Extinction from dust is so high that it is invisible in wavelengths shorter than the NIR, and is the brightest source in the galaxy at wavelengths longer than the H-band (Turner et al. 2003; Alonso-Herrero et al. 2004; Martín-Hernández et al. 2005). Its dustiness ($A_V \gtrsim 16 - 18$), together with detection of Wolf-Rayet signatures (Conti 1991; Schaerer et al. 1997; López-Sánchez et al. 2007; Monreal-Ibero et al. 2010; Westmoquette et al. 2013), suggest the presence of stars ∼1-3 Myr in age (e.g., Alonso-Herrero et al. 2004; Calzetti et al. 2015; Smith et al. 2016). Submillimeter observations found a warm CO(J=3–2) cloud, Cloud "D1", that is coincident to within 0.6 pc of the H II region and within 2 km s^{-1} of IR and radio recombination line velocities (Turner et al. 2015, 2017). This gives the first indication that there are potential star-forming molecular clouds within the cluster itself.

The CO gas is remarkably quiescent ($\sim$22 km s^{-1} FWHM) considering its extreme environment, within a 3 pc region containing thousands of O stars. The linewidth of Cloud D1 reflects only the gravitational motions of the cluster, with no evidence for molecular outflow. The supernebula thus does not appear to be launching a galactic wind of the kind seen, for example, in NGC 253 (Sakamoto et al. 2006; Bolatto et al. 2013).

Observations of the supernebula suggest feedback is similarly ineffective in driving outflows of ionized gas from the exciting SSC. Turner et al. (2003) observed the Brackett α and γ recombination lines in the supernebula with a 0.″5 slit using NIRSPEC and found, in addition to high extinction, a relatively small linewidth (FWHM of 76 km s^{-1}), similar to widths seen in Galactic H II regions and comparable to the escape velocity of the cluster. Measurements of mid-IR emission lines (Beck et al. 2012) and radio recombination lines (RRLs; Rodríguez-Rico et al. 2007; Bendo et al. 2017) confirm this measurement. The gravity of the massive cluster clearly has a large role in shaping the gas motions and could potentially launch a cluster wind. However, numerical wind models suggest that if the NGC 5253 supernebula is sufficiently chemically enriched, strong radiative cooling can suppress a starburst wind (Silich et al. 2003, 2004; Silich & Tenorio-Tagle 2017). Localized chemical enrichment has in fact been indicated in NGC 5253 by nuclear abundance studies (Walsh & Roy 1989; Kobulnicky et al. 1997; López-Sánchez et al. 2007; Monreal-Ibero et al. 2010; Westmoquette et al. 2013) and by submillimeter continuum emission from dust (Turner et al. 2015), and in other SSCs (Consiglio et al. 2016).

In this study we present high resolution (0.1″) observations of Br α emission across the NGC 5253 supernebula, made with the NIRSPEC spectrograph on Keck II using laser-guided adaptive optics (NIRSPAO). At 4 μm, the Br α line is less effected by extinction than H α or Br γ, allowing us to probe gas embedded within the SSC. What is happening to the gas in this potential proto-GC, which appears to be in its infant phase? The goal of this investigation is to use our Br α observations to infer the kinematics of the supernebula and determine the influence and fine structure of feedback from the cluster. At the 3.8 Mpc distance of NGC 5253 (Sakai et al. 2004), $0.1'' = 1.8$ pc.

2.2 Observations & Data

The supernebula in NGC 5253 was observed with NIRSPAO (McLean et al. 1998) in the second half-night on May 1, 2015. Spectra were taken in high-resolution mode (R$\sim$25,000), in the KL band, using the $2.26'' \times 0.068''$ slit. The echelle and cross-disperser angles were set to 64.5° and 34.12°, respectively, yielding a wavelength coverage of roughly 4.03-4.08 μm in the 19th echelle order. The spatial resolution of the observations is $\simeq 0\farcs12$, determined from the continuum spectra of several calibration stars.

The slit was oriented at a position angle of 113.5° (so that the slit-parallel direction is close to the E-W axis), with each position separated by the slit width ($\simeq 0\farcs07$). The slit positions are hereafter labelled: N2, N1, S1, S2 from north to south. During spectral exposures, the the Slit-Viewing Camera (SCAM) was used to simultaneously and continuously image the slit on the sky in the K band, giving a record of the slit position relative to the NIR continuum.

A stacked, reduced SCAM image was constructed to study the spatial distribution of gas and determine registration of slit positions with respect to the radio supernebula. To form this image, raw SCAM images with the supernebula on-slit were subtracted by images taken with the supernebula off-slit (at the end of the night during sky exposures). Then, for each separate slit position, clusters visible in the field-of-view were used to align all sky-subtracted SCAM images. The slits were masked out in each of the four images, which were then aligned, and the average was computed over each pixel to form a combined, slit-free SCAM image.

To reduce the NIRSPAO spectra, we applied spatial and spectral rectification to all raw NIRSPEC images using the IDL-based REDSPEC pipeline[1]. Arc lamps used for calibration were not functioning properly for the observing run, yielding no emission lines in the Br α order. New arc lamp spectra obtained on a later date (with the same configuration) detect emission lines in this order, but the resulting wavelength calibration is inaccurate in its wavelength zero-point. The issue can be partially corrected by determining the offset between the rest wavelength of Br α and the Br α absorption line detected in a calibrator star spectrum. However, there is no measurement of radial velocity for the calibrator. Centroid velocities inferred from the Br α emission of the su-

[1] https://www2.keck.hawaii.edu/inst/nirspec/redspec.html

pernebula are $\sim$30-40 km s^{-1} higher than the previously-determined velocity of 391 ± 2 km s^{-1} (heliocentric), measured for the H30α line (Bendo et al. 2017) and for the narrow component on the [S IV] 10.5 μm line (Beck et al. 2012). Fortunately, we have He I and Br α lines to determine the wavelength scale, and the measured and expected separation between these lines are consistent to within 2-3%, or $\lesssim$6 km s^{-1}. Because we are only interested in the velocity linewidths and the *relative* variation of centroid velocity across the supernebula region, the velocity zero-point does not change any of our results or conclusions. To facilitate comparison with other studies, we shift the spectra so that the Br α line in the average spectrum across the four slit positions is at a centroid velocity of 391 km s^{-1}.

Following rectification, individual spectra were sky-subtracted and divided by a median-normalized flat-field image, and hot/cold pixels were removed. Reduced exposures were median-combined to form the the 2D spectrum, or echellogram, for each of the four slit positions. Fringe patterns due to interference within the detector are apparent in the echellograms. We tested a correction for fringing but find that it does not significantly change any results or derived quantities. Since these are slit spectra made through AO observations it is difficult to estimate the absolute calibration of line strength, which has been done elsewhere (Turner et al. 2003). The resulting four echellograms have spectral resolution of $\sim$12 km s^{-1} and spatial resolution of $\simeq$0.″1 (with pixel size 0.″018 pix^{-1} in the spatial direction).

For analysis of kinematics (§ 2.4), 1D spectra are extracted by summing or averaging rows in the echellograms. Gaussian models are fit to the emission in the extracted spectra to infer line properties.

2.3 Nature of the NIR Continuum and Relation to Optical Clusters

The NIRSPAO echellograms (spectrum along the x-axis, slit along the y-axis) are shown in Figure 2.1 along with the positions of the slits on the stacked SCAM image. The spectra reveal strong Br α emission arising from the supernebula, which is spatially coincident with the 4μm continuum. Blueward of Br α, there is a detection of the He I 4.04899,4.04901 μm emission line doublet (Hamann & Simon 1986; Tokunaga 2000) from the supernebula. The SCAM imaging, shown in

Figure 2.2, detects K-band continuum associated with the features in the Br α spectra, and can be used to provide an astrometric and morphological context for the supernebula.

The Br α line and surrounding 4 μm continuum emission are strongest in slit position S1, confirming that this position is centered closest to the core of the supernebula. Although interpolation between slits to determine an exact peak is nontrivial, the intensity variation implies a Br α peak that is $\lesssim$0.05″ north of the center of the S1 slit. The peak of the brightest K-band source is likewise located between S1 and N1, and coincident with the Br α peak to within half a 0.07″ slit.

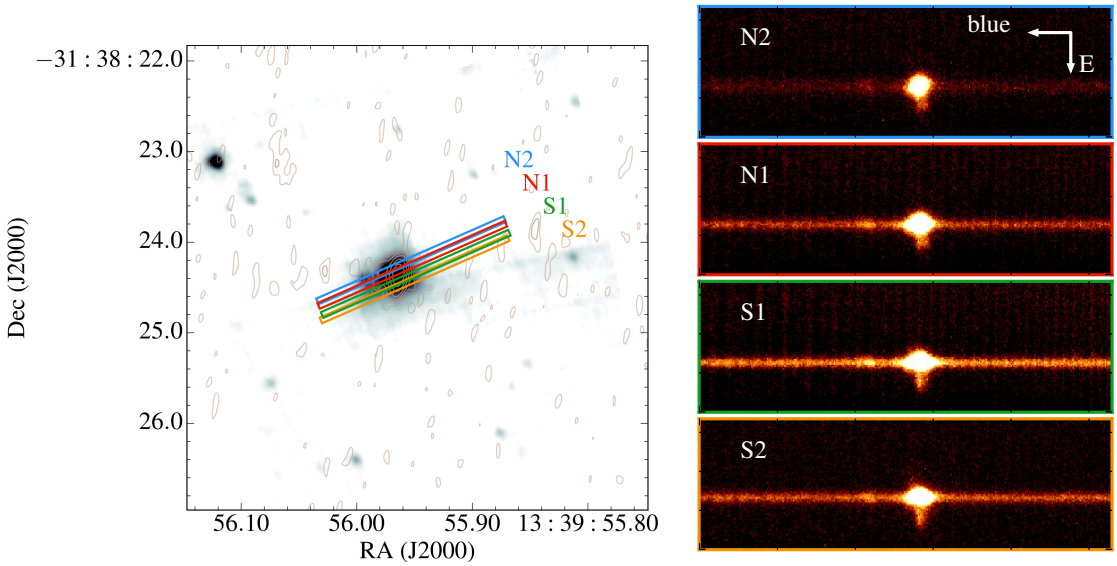

Figure 2.1: Echellograms of the supernebula in NGC 5253 . *Left*) K-band continuum from SCAM showing slit positions. Contours show the 1.3 cm continuum map from Turner et al. (2000), which traces free-free radiation. *Right*) In each spectrum, east runs vertically downward, and the spectral direction runs horizontally with wavelength increasing to the right. The spectra show: (*i*) strong Br α emission and continuum from the supernebula, (*ii*) weaker He I emission from the supernebula, and (*iii*) an extension of Br α emission primarily to the east of the supernebula's continuum (extending down in the figure). 0.1″ = 1.8 pc.

The relative positions of the embedded radio/IR supernebula with the optical clusters in the region has been an issue of some debate, since it is clear that there is significant extinction in the region (Calzetti et al. 1997; Turner et al. 2003). The coordinates in HST images are not known to subarcsecond precision relative to the International Celestial Reference System (ICRS) coordinates, which are determined to $\lesssim$50 mas coordinates in the VLA and ALMA images of the free-free and CO(3–2) emission: $(\alpha,\delta)_{7mm}$=($13^h39^m55^s.9631$, 31°38′24.″388) (Turner & Beck 2004) and $(\alpha,\delta)_{CO}$=($13^h39^m55^s.9651$, 31°38′24.″364) (Turner et al. 2017). Our new AO view of the region's NIR continuum from SCAM taken simultaneously with the Br α can now tell us how the

visible light and IR-radio light within the vicinity of the supernebula are related by linking the K-band peak, hence the bright Br α source, to the optical clusters.

Registration of the SCAM and HST images is determined by aligning the bright NIR clusters in the SCAM images (some of these clusters can be seen in Fig 2.2), with optical counterparts in the HST F814W image from the LEGUS survey (Calzetti et al. 2015). Registration of the SCAM and radio images is determined by noting that the bright free-free source in the radio images is the same source responsible for the brightest Br α emission, which we have found is coincident with the K-band peak. We can then align the HST images with the VLA and ALMA images to within $\sim$50 mas. This registration is reinforced by visually aligning these registered HST images with bright clumps in the CO map of Turner et al. (2017); the bright CO peak associated with Cloud D1 is coincident with the supernebula and Br α peak. Aligned this way, the CO clouds coincide with regions of visual extinction.

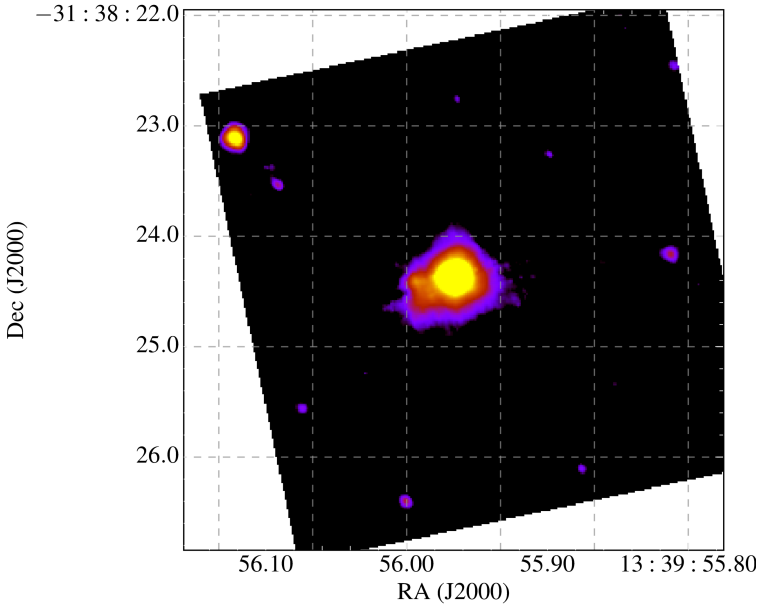

Figure 2.2: K-band continuum of the supernebula and surrounding clusters. The slit-free, stacked SCAM image, with resolution $\simeq$0.″1, is shown here in log scale to highlight extended features. The size of the supernebula core is 0.″2 FWHM in this image, derived from a Gaussian fit to the emission profile. A secondary K-band peak is detected $\simeq$0.″4 east of the peak emission of the supernebula.

In Figure 2.3, we overlay the registered slit-free SCAM image with the HST F814W image and the ALMA CO(3–2) map. Here we identify visible clusters #5 and #11 from Calzetti et al. (2015) and cluster #105 from de Grijs et al. (2013). Clusters #5 and #11 possibly contain stars with ages of

$\lesssim$1 Myr, based on radio fluxes and SED modeling by Calzetti et al. (2015), who suggest that these visible point-like sources could be the SSCs that power the supernebula. As seen in Figure 2.3, these clusters are not coincident with the K-band/Br α peak emission of the supernebula: cluster #5 is offset by 0.″35 or 6.4 pc, while cluster #11 is a closer 0.″14 or 2.6 pc. The compact radio core of the supernebula (Turner & Beck 2004) requires an extremely luminous cluster – even the small offset of cluster #5 to the edge of the nebula would introduce a solid angle-induced luminosity augmentation that is inconsistent with the already "too large" cluster luminosity, given the dynamical mass constraints imposed by the CO linewidth (Turner et al. 2017).

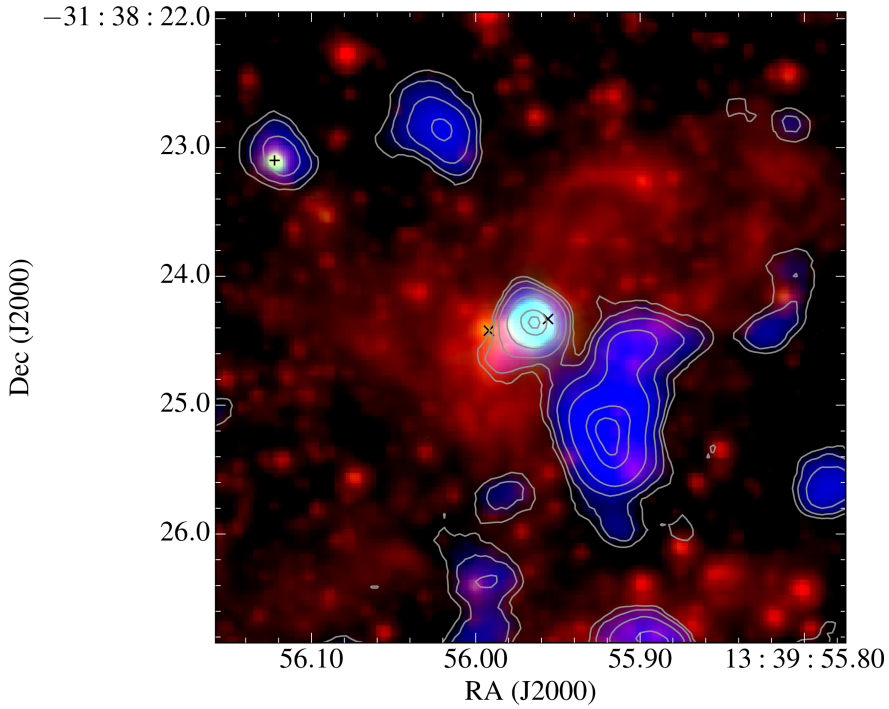

Figure 2.3: Overlay of the K-band continuum, visible continuum, and CO emission near the supernebula. The SCAM K-band image is in green, the F814W continuum from HST/LEGUS (Calzetti et al. 2015) is in red, and ALMA CO(3–2) is shown as blue and with contours (Turner et al. 2017). The coincidence of the NIR continuum with the CO cloud D1 and visible extinction causes the embedded supernebula to appear light blue. Positions of visible clusters near the supernebula from Calzetti et al. (2015) are shown as black X's: cluster #5 and #11 are offset 0.″35 east and 0.″14 west of the supernebula peak, respectively. Cluster 105 from de Grijs et al. (2013) is shown with a black cross. Positions of the optical clusters have been shifted based on radio registration as described in the text.

The perfect coincidence of the NIR continuum peak with the compact radio supernebula and Cloud D1, its extended appearance, and correspondence with the visible extinction, imply that the 2μm continuum is from dust emission. The presence of localized dust in the supernebula is supported by the detection of strong submillimeter continuum indicating a substantial ($10^{4.2}$ $M_\odot$)

amount of dust (Turner et al. 2015). If even a small fraction of this dust is at temperatures of $T_d \sim 750$ K, the emission is easily explained. Furthermore, there is excess NIR flux from the supernebula that cannot be accounted for by purely stellar+nebular models, requiring a dust emission component (Alonso-Herrero et al. 2004; Calzetti et al. 2015). The extended nature of the K-band emission, with a size of 0.″2 FWHM = 3.7 pc, suggests that the hot dust is not concentrated to the core of the supernebula cluster, especially if the eastern component (near cluster #5) is also from dust.

Although offset east from the supernebula core, cluster #5 is coincident with a weaker, secondary K-band peak detected with SCAM, apparent in Fig. 2.2. This source has also been detected in VLA radio continuum images (Turner et al. 2000). The NIR continuum emission around this component is extended out to $\sim$0.″3 south from its peak. Br α is also detected from the eastern component, seen in Fig. 2.1 as a tail of emission extending out to $\sim$0.″6 or 12 pc to the east of the supernebula peak (well past the position of cluster #5). Such extended morphology calls into question whether this NIR source is indeed starlight from a cluster, or, like the supernebula K-band source, has a significant contribution from hot dust.

In summary, our high resolution images and spectra reveal no visible clusters at the center of the supernebula that are likely to be the origin of the exciting UV photons. A strong dust continuum at 2μm can affect inferred properties of the SSC that rely on NIR emission lines and continuum, as noted by Calzetti et al. (2015) . Specifically, measurements of age based on the equivalent widths of NIR recombination lines such as Br γ become upper limits, since the contribution to the continuum from the older non-ionizing population will be overestimated. Thus, our observations are consistent with previous suggestions the radiation fields powering the radio/IR supernebula are due to very young stars, of age $\lesssim$ 1-2 Myr (Calzetti et al. 2015; Smith et al. 2016).

2.4 Recombination Line Spectroscopy

The Br α line profile and its spatial variation encode detailed gas motions, from which we can infer the presence of feedback and how it is affecting the SSC formation. Although we focus on the Br α line, the He I 4.04899,4.04901 μm emission present in the spectra represents the

first detection of this doublet in an extragalactic source, to our best knowledge. Other He I lines have been observed in the supernebula at visible and NIR wavelengths (Smith et al. 2016; Cresci et al. 2010), indicative of massive exciting stars with high effective temperatures and sizeable He^+ zones. The echellograms suggest that the He I emission is more confined to the nebular core than the Br α.

To study the detailed line profile of Br α and its variation between slit positions (§2.4.1 and §2.4.2.1), we first analyze integrated spectra, which are extracted by summing 12 rows=0.″215 in each echellogram centered on the peak Br α emission. The extraction box is chosen to be wide enough to detect faint features but small enough to probe emission from the core, matching the K-band size of the supernebula (§2.3). The signal-to-noise at the line peak in these spectra is estimated from the rms, which includes fringing: $(S/N)_{peak}$ = 67, 45, 42, and 43 for slits N1, S1, N2, and S2 respectively. We follow our analysis of integrated spectra with investigation of the more detailed spatial variation of Br α velocity as probed by a map of the emission, extracted by averaging spectra in bins of 6 rows=0.″108 across each echellogram (§2.4.2.2 and §2.4.3).

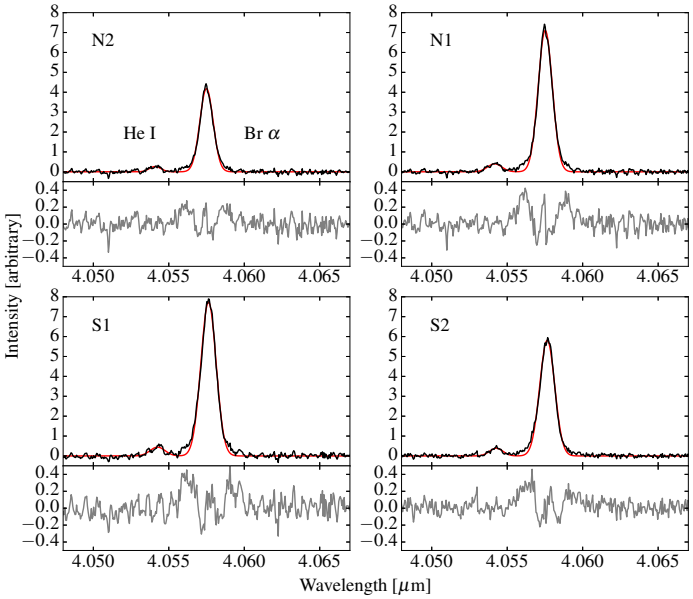

Figure 2.4: Continuum-subtracted, 1D spectrum extracted with a 0.″2 aperture from the echellograms for each of the four slit positions. For each spectrum, the top panel shows the data (black curve) and best-fit models of single Gaussian profiles for the Br α and He I lines (red curve), and the bottom panel shows the fit residuals data−model (grey curve). We only fit Br α emission at above 10% of the line peak to account for faint wings.

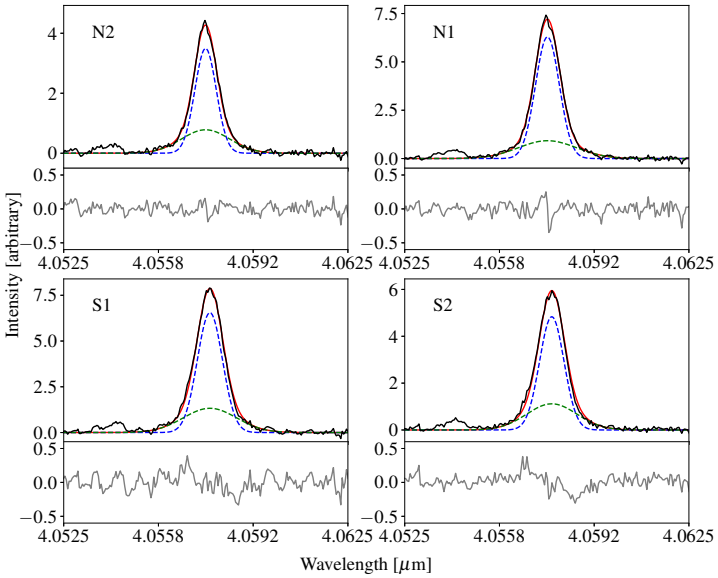

Figure 2.5: Same as in Fig. 2.4, except the Br α is fit with a two-component Gaussian model: a weak, broad component (dashed green line) for the shoulders at the base of the line, and a stronger, narrower component corresponding to the line core emission (dashed blue). The combined fit is in red. The two-component model yields smaller residuals (compared with Fig. 2.4) in both the wings and the very core of the line.

2.4.1 The Line Profile

The Br α emission detected for the four slit positions across the supernebula spans a range of just over 10 km s^{-1} in centroid velocity (about one resolution element of NIRSPEC) and exhibits linewidths of FWHM=75-87 km s^{-1}, based on best-fit models of a single Gaussian profile to emission at $>$10% of the line peak intensity (Table 2.1 and Figure 2.4). The profile is narrower in the northern slit positions (N1 and N2), comparable with the Br α linewidth of 76 ± 1 km s^{-1} presented in Turner et al. (2003). In slits S1 (closest to the peak of the supernebula) and S2, however, the line is broader by $\sim$10 km s^{-1}. This can be compared to lower spatial resolution radio recombination lines, with a FWHM of 58 ± 12 km s^{-1} for H53α (Rodríguez-Rico et al. 2007) for a 3″ beam, and 68 ± 3 km s^{-1} for H30α (Bendo et al. 2017) for a 0.″2 beam. In the MIR, Beck et al. (2012) inferred a linewidth of 65 km s^{-1} for the [S IV] 10.5 μm emission within a 1.″2 slit.

Table 2.1: Br α and He I line properties from NIRSPAO spectra for each slit position (0.″2 extraction box). Br α fit parameters are quoted both for the single Gaussian model, and the two-component model consisting of a strong, narrow core and weak, broad wings.

Position	$v_{\mathrm{Br}\alpha}$ [km s^{-1}][a]	FWHM$_{\mathrm{Br}\alpha}$ [km s^{-1}][b]	v_{HeI} [km s^{-1}] [c]	FWHM$_{HeI}$ [km s^{-1}] [d]	$I_{\mathrm{Br}\alpha}/I_{HeI}$ [e]
avg	391 ± 1	84 ± 1	382 ± 3	81 ± 10	16 ± 1
N2	384 ± 1	75 ± 1	374 ± 4	67 ± 11	15 ± 2
N1	386 ± 1	80 ± 1	380 ± 3	82 ± 8	17 ± 1
S1	394 ± 1	87 ± 1	386 ± 5	86 ± 12	17 ± 2
S2	396 ± 1	86 ± 1	387 ± 4	77 ± 10	14 ± 1
v_{core} [km s^{-1}][f]	FWHM$_{core}$ [km s^{-1}][g]	v_{wing} [km s^{-1}][h]	FWHM$_{wing}$ [km s^{-1}] [i]	I_{wing}/I_{core} [j]	
391 ± 1	77 ± 1	385 ± 5	189 ± 18	0.13 ± 0.03	
384 ± 1	65 ± 2	386 ± 3	147 ± 13	0.22 ± 0.05	
386 ± 1	73 ± 1	385 ± 3	177 ± 12	0.15 ± 0.02	
395 ± 1	76 ± 2	385 ± 5	163 ± 15	0.20 ± 0.05	
397 ± 1	74 ± 2	383 ± 5	154 ± 12	0.23 ± 0.06	

[a] Centroid velocity (heliocentric) of the Brα line (from single fit). A wavelength shift was applied to the spectra so that the Br α emission is at a velocity of 391 km s^{-1} in the average spectrum across the four slit positions, to match the velocity determined from H30α in a 0.″2 beam. [b] FWHM of Br α emission (from single Gaussian fit).
[c] Centroid velocity (heliocentric) of the He I line. The velocity offset of about -10 km s^{-1} for He I relative to Br α could reflect our use of 4.049μm as the He I rest-wavelength, while in-reality the line is a blended doublet.
[d] FWHM of the blended He I doublet. [e] Intensity ratio of Brα to He I. [f] Centroid velocity of narrow Br α component. [g] FWHM of the narrow Br α component. [h] Centroid velocity of broad Br α component.
[i] FWHM of the broad Br α component. [j] Peak intensity ratio of broad wings to the core.

Figure 2.4 shows that our high-S/N spectra detect wings on the base of the Br α line at $\sim$10-15% of the peak line intensity, which cannot be fit well by a single Gaussian model. To account for this feature, the Br α profiles are additionally fit with a model consisting of two Gaussians: a weak, broad component and a stronger narrow core. The resulting best-fit parameters are reported in Table 2.1. The two-component model, shown in Figure 2.5, provides a better fit in the wings and core of the observed Br α line, suppressing the residuals that result from the single-Gaussian fits. The narrow Br α component is found to have FWHM$_{core}$ =65-76 km s^{-1}, smaller than the linewidths from the single-Gaussian models, and consistent with previous recombination line measurements which did not detect broad shoulders. We discuss the implications of the Br α linewidths in § 3.4.

In the context of cluster feedback, the high-velocity shoulders on the base of the Br α emission line are very intriguing. Our two-component models suggest broad-component widths of FWHM$_{wing}\simeq$150-175 km s^{-1}. Broad components with FWHM$\simeq$100-250 km s^{-1} have been detected on the H α line in the supernebula region, but on a larger scale and for an extended gas component that is much less extincted than the supernebula gas (Monreal-Ibero et al. 2010; Westmoquette et al. 2013). The Br α wings are roughly symmetric about the core in slits N1 and N2, but appear to be stronger on the blue side for slits S1 and S2, supported by a slight blueward shift in the broad component centroid in S1/S2 relative to N1/N2 (Fig. 2.5 and Tab 2.1). The [S IV] emission from the supernebula exhibits excess emission extending on the blue side out to -100 km s^{-1} from the peak (Beck et al. 2012), suggesting that the slit used for these TEXES observations could have been positioned south of the supernebula peak. However, the discrepancy in velocity is significant: a blue wing is clearly detected for the [S IV] line and extends to high velocity, while the Br α wings are weak and more confined in velocity. Nonetheless, a broad pedestal of emission appears to be a common feature for ionized gas lines in SSCs, previously observed in the Brackett lines from clusters in He 2-10 and other systems (e.g., Henry et al. 2007). As discussed in § 3.4, this feature could reflect a population of individual young stellar objects (YSOs) with broad line profiles or other stars that are driving high-velocity winds (Beck 2008).

2.4.2 Velocity Structure of the Supernebula

The spatial variation of Br α emission, particularly its centroid velocity, traces the motions of gas associated with the supernebula. We can analyze the velocity structure and determine if it supports a consistent scenario to that implied by the integrated line profile.

2.4.2.1 North-South Velocity Shift

The centroid velocity of the supernebula core (Tab. 2.1) exhibits a clear shift from northern to southern slit positions, shown in the left panel of Figure 2.6. The magnitude of this shift is +13 km s^{-1} across the $\sim$0.″3=5.5 pc between N2 and S2, about one full resolution element of NIRSPEC. Subtraction between the southern and northern echellograms, shown in the right panel of Fig. 2.6, supports the Br α core shift inferred from the 1D spectra. The most intriguing feature in this figure is the negative arc that curls around the blue side of the southern Br α peak. This profile results from the line core shift to the blue of the northern portion, and because the northern emission is more spatially extended than the southern portion. Indeed, the intensity profiles along each slit indicate that the Br α emission is more extended by $\sim$0.″15 in N2 relative to that in S2.

Similar velocity structure is suggested by the H53α line, which exhibits a NW-SE gradient of 10 km s^{-1} arcsec^{-1} on much larger (3″) scales (Rodríguez-Rico et al. 2007), along with channel maps of the H30α line, which reveal blueshifted emission in the NE edge of the supernebula (Bendo et al. 2017). To the south of the supernebula/Cloud D1, there is another CO cloud, D4, that is redshifted relative to D1 (Consiglio et al. 2017). The CO(3–2) morphology suggests a potential connection between D1 and D4 (Fig. 2.3), which could explain the Br α velocity shift. Alternatively the Br α gradient could indicate cluster rotation, or an outflow with a bipolar morphology. We discuss these possibilities in Section 3.4.

The velocity shifts described above apply to the narrow line core, the strongest portion of the Br α, but not necessarily to the broad component of the line described in Section 2.4.1. As indicated in Fig. 2.5, the Br α wings are more apparent on blue side of the line for slits S1 and S2. This could result from a slight blueshift in the velocity centroid of the broad emission from north to south, although the Gaussian fits suggest that the broad component is static across the superneb-

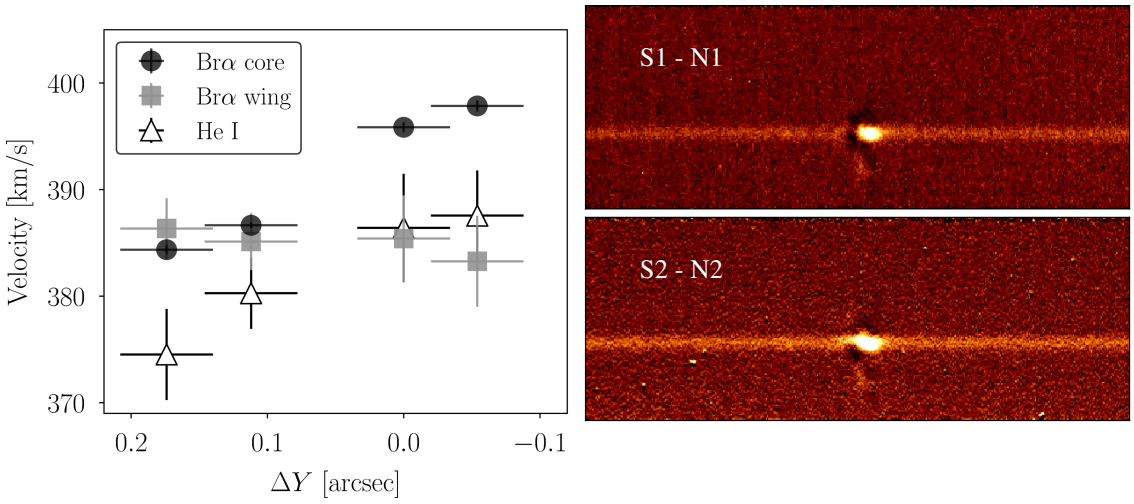

Figure 2.6: Velocity shift across the supernebula. *Left)*: Centroid velocity (heliocentric) of the Br α line (narrow and broad components) and He I doublet as a function of slit position in the slit-offset direction; north is left and south is right, and the zero-point is set to slit position S1. There is a clear blueshift of the Br α core and He I doublet in the northern slit positions relative to southern by $\simeq$13 km s^{-1}. We note that He I centroids are offset blueward of Br α; this likely arises from use of a single reference wavelength to derive the velocity of the He I doublet. *Right)*: Difference between southern (S1/S2) and northern (N1/N2) echellograms. The negative arc curling around the blue side of the supernebula's Br α emission is due to the N-S line core shift along with the emission in the north being more extended relative to that in the south.

ula (Fig. 2.6). Alternatively, there could be an asymmetry of the broad component in the south, possibly owing to extinction or inherent variance between the populations of broad-line sources contained in each slit. That there are still features present in the residuals of Fig. 2.5 supports such an asymmetry. Ultimately, more sensitive observations of the Br α wings are required to study their variation near the cluster.

2.4.2.2 2D Variation in Line Core Velocity

Figure 2.7 shows the map of the Br α spectrum in $\sim$0.″1 bins across the full $\gtrsim$1″ extent of emission. The map reveals the changes in line profile across the region. The centroid velocity of Br α is inferred with best-fit single-component Gaussian models to each spectrum within the map.

The Br α map provides a more detailed picture of the velocity structure near the supernebula, including variations of the emission parallel to the slits. Fig. 2.8 shows the Br α centroid as a function of position along the slit, for each of the four slits. This plots recovers the blueshift of emission in slits N1/N2 relative to that in S1/S2, within the extent of the supernebula. Moreover,

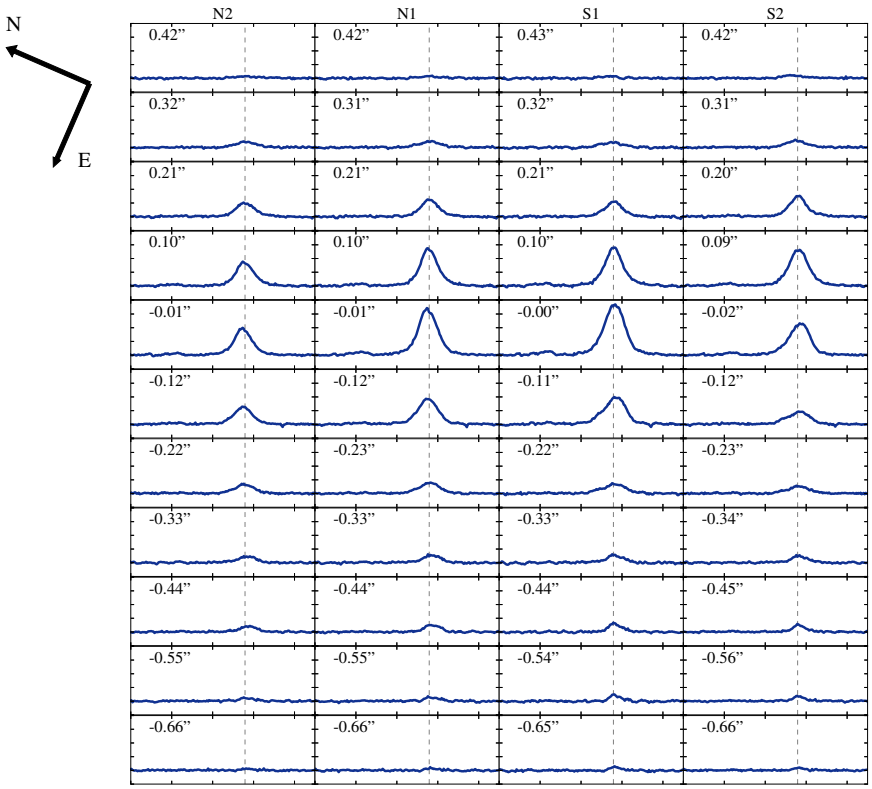

Figure 2.7: Map of the Br α line across the supernebula, extracted in bins of $\simeq 0.11''$ across each echellogram. Each column is a separate slit position, running north to south from left to right, and rows are such that east is down and west is up. For reference, we mark the Br α centroid derived for the average of all four echellograms as a dashed vertical line in each plot. Within each panel, we quote the distance from the peak Br α emission for the corresponding echellogram.

for a given slit, there is velocity shift from the edges the towards the center of the supernebula, with the northern emission being blueshifted in the center relative to the edges while the southern emission is redshifted. This structure disfavors spherically symmetric expansion of the ionized gas.

The full 2D velocity structure is visualized in the context of the K-band continuum (§ 2.3) in Figure 2.9, which overlays filled contours of centroid velocity on the SCAM image and its intensity contours (akin to a moment-one map). The NE-SW velocity gradient across the supernebula represents the only potential detected signature of an outflow from the cluster, aside from the broad wings on the Br α line (see § 3.4).

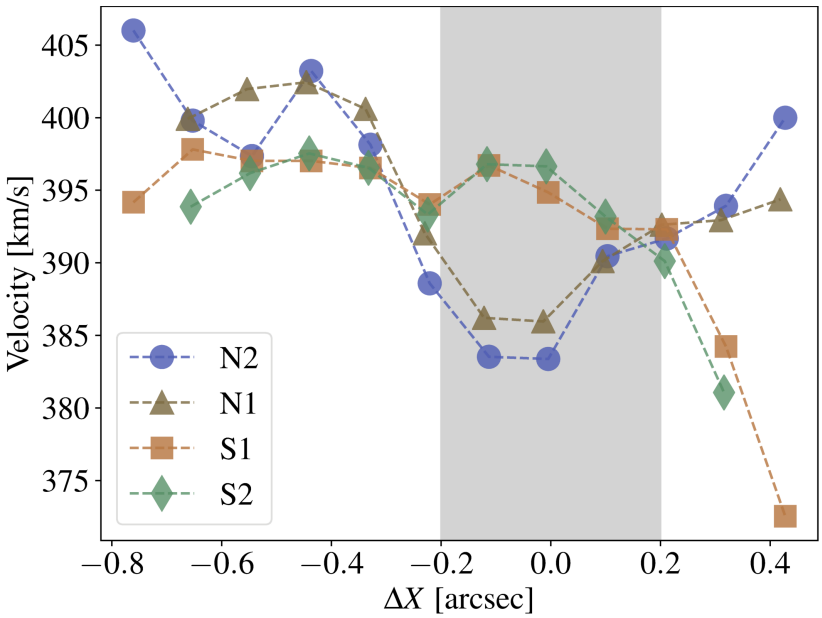

Figure 2.8: Centroid Br α velocity (heliocentric) versus position along the slit, showing the E-W velocity variation; east is left and west is right. The zero-point defines the position of the Br α peak along each slit. The supernebula is shaded in grey.

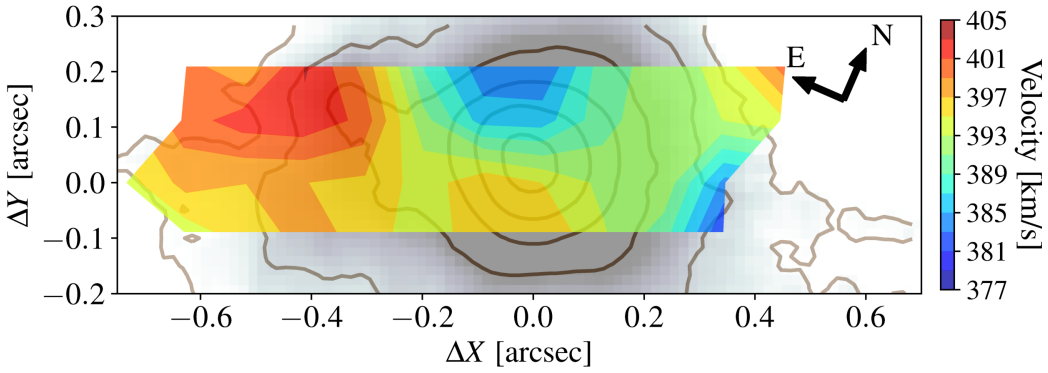

Figure 2.9: Map of the Br α velocity centroid (heliocentric) near the supernebula. The velocity map is visualized as colored, filled contours, which are overlaid on the SCAM K-band image shown in greyscale and as brown solid contours. This figure shows the correspondence between the gas kinematics and the morphology of the supernebula. ΔX is the slit-parallel direction, with zero-point defined by the peak emission in the echellograms, and ΔY is the slit-perpendicular position, with zero-point defined by the center of slit S1. To overlay the SCAM image, we match the K-band peak to the origin of these axes.

2.4.3 Extended Emission

The NIRSPAO spectra (Fig. 2.1) show that the Br α emission extends $\gtrsim$10 pc (projected) to the SE of the supernebula's peak, well past the core radius. As shown in § 2.3, the eastern Br α emission is detected in the K-band imaging as a secondary peak that is coincident with the position of visible

cluster #5, surrounded by more diffuse continuum.

Gas from the eastern component is redshifted by $\sim$5-15 km s^{-1} relative to the supernebula, easily distinguished from the supernebula core (Fig. 2.9). The maximal redshift of this eastern gas is concentrated to the position of the eastern K-band peak and cluster #5. The velocity exhibits a smooth decrease with distance from away this emission peak. That the eastern component is redshifted and has much lower extinction relative to the supernebula suggests that it is on the near side of the supernebula and infalling, with the more compact emission region (cluster #5) leaving behind a wake of gas. Whether or not the gas in the east is related to gas to the south, which is also redshifted (Sec 2.4.2.1), is unclear.

Previous observations have found evidence for NW-SE velocity variations near the supernebula. Channel maps of H53α support the presence of redshifted gas extending east from the supernebula, although the lower resolution cannot identify the eastern gas as a separate component (Rodríguez-Rico et al. 2007). Furthermore, ALMA observations of CO(3–2) and CO(2–1) reveal a tail of molecular gas extending east from Cloud D1 on the red side of the line (Turner et al. 2017). In the optical, a NW-SE velocity gradient is measured for a broad component and weaker narrow component of H α, but with opposite orientation to that exhibited by Br α, such that gas is blueshifted to the east (Monreal-Ibero et al. 2010; Westmoquette et al. 2013). However, the H α is from gas associated with the optical lobes running SE-NW (Fig. 2.3), on scales much larger than the supernebula, while the bright Br α is from heavily reddened gas associated directly with the supernebula. Moreover, the H α velocity gradient is most apparent for the *broad* component of H α, while we only detect velocity structure for the *narrow* component of Br α. The H α structure is potentially a signature of an accelerating outflow (Westmoquette et al. 2013); a comparison with velocity structure for the Br α wings would be informative but requires more sensitive observations.

2.5 Discussion: The State of Feedback in NGC 5253

With recent subarcsecond observations, including those we present here for the ionized gas, and for the CO and ionized gas from from ALMA (Turner et al. 2017; Consiglio et al. 2017; Bendo et al. 2017), we can begin to understand the physical mechanisms occurring at the sub-cluster scale

in the forming SSC in NGC 5253.

Our NIRSPAO observations reveal a recombination linewidth of 65-76 km s^{-1} (FWHM) in the line core, along with a broad wings with linewidth $\sim$150-175 FWHM. The broad component is weaker, constituting $\sim$25-30% of the total line flux. The core emission is relatively narrow, considering that it is convolved both with the thermal linewidth of 22-23 km s^{-1}, corresponding to an H II region temperature of 11,000-12,000 K (Kobulnicky et al. 1997), and the dynamical linewidth due to the cluster mass, also 21.7 km s^{-1}. The deconvolved linewidth of $\sim$58-70 km s^{-1} is comparable to the linewidths of individual recombination lines in individual Galactic H II regions (e.g., Jaffe & Martín-Pintado 1999; De Pree et al. 2004; Sewilo et al. 2004a; De Pree et al. 2011).

2.5.1 The Supernebula as a Compact H II Region

Feedback from H II regions can be effective at disrupting GMCs and regulating star formation, depending on the details of their dynamical evolution and interaction with the winds from their exciting massive stars (e.g., Matzner 2002). The simplest model of H II region evolution, spherically symmetric pressure-driven expansion, cannot account for the large number of ultra-compact H II regions (UCH II) found embedded within massive-cluster forming regions in the Milky Way, such as in W49 (e.g., Dreher et al. 1984; De Pree et al. 2000).

Realistic models of H II region dynamics solve this well-known "lifetime problem" (e.g., Wood & Churchwell 1989) by invoking dense, molecular gas that can prolong the expansion of the ionized region out of its compact phase. For example, "champagne flows" from blister H II regions can account for much of the observed population of UCH II and their morphology (Tenorio-Tagle 1979). Models that can additionally explain the broad recombination lines observed for a large fraction of the UCH II population invoke photoevaporation of circumstellar disks (e.g., Hollenbach et al. 1994; Lizano et al. 1996) or mass-loading of O star winds by photoevaporation of circumstellar clumps (Dyson et al. 1995).

The Br α linewidth may seem small considering the extreme cluster luminosity and youth, as noted previously (Turner et al. 2003; Rodríguez-Rico et al. 2007; Beck et al. 2012; Bendo et al. 2017). However, if the supernebula comprises thousands of compact H II regions within the cluster,

the line is perfectly consistent with the line profile of an individual compact H II region convolved with the thermal linewidth of HI and the gravitational linewidth of the cluster (Turner et al. 2017), as first pointed out by Beck (2008).

Molecular gas, traced by CO, is present in the NGC 5253 SSC (Turner et al. 2015, 2017; Consiglio et al. 2017). The small CO linewidth, only tracing the stellar motions due to gravity, suggests that the molecular gas is bound to individual stars. Thus, we suggest that the embedded SSC contains thousands of massive stars which are currently accreting in the form of large molecular disks, or heating molecular clumps. These O stars ionize surrounding gas and form compact H II regions, which much like Galactic H II regions, can be sustained at their sizes of $\sim$0.1 pc for the cluster age ($\sim$1 Myr or less) through replenishment of the expanding plasma via photoevaporation and ablation of the bound molecular gas. As discussed further in Sec. 2.5.2, radiative cooling is likely to play a fundamental role in preventing the ionized wind regions from merging, and can result in the formation of enriched molecular clumps.

The narrow Br α component suggests that most of the H II regions in the SSC are expanding slowly, similar to Galactic H II regions. However, the broad pedestal on the base of the Br α line provides a potential channel for gas escape, with linewidths that are similar to those observed around individual YSOs, which exhibit FWHM$_{\mathrm{Br}\alpha}$=50-250 km s^{-1} (Persson et al. 1984). Despite potential high-velocity winds that could be breaking out of the cluster, these broad-line sources contain a small fraction of the cluster's gas, and are not likely to drive a mass-loss rate that is presently large enough to disrupt the SSC. Nonetheless, the cluster might still influence its environment through these sources by losing mass and thereby polluting the surroundings with enriched material.

2.5.2 The Suppression of Winds

The details of how a forming cluster disperses its gas shape its evolution and survival. Gas is expelled through winds and supernova explosions (SNe) from massive stars, and the structure and evolution of these outflows are determined by the competing effects of the outward overpressure of thermalized gas, the inwardly-directed collective gravity, and energy losses due to radiative

cooling. Simulations of feedback-driven winds typically assume the winds are adiabatic, where cooling is negligible. In this case, stellar winds and SNe can merge to form a coherent cluster wind, clearing all gas from a SSC soon after formation of massive stars (e.g., Chevalier & Clegg 1985; Cantó et al. 2000). In reality, radiative cooling will significantly affect the operation of mechanical feedback and substantially alter this scenario.

Cooling losses are enhanced in chemically enriched gas, and there is strong evidence that the SSC in NGC 5253 cluster has enriched its environment with products of stellar evolution (Walsh & Roy 1989; Kobulnicky et al. 1997; Schaerer et al. 1997; Monreal-Ibero et al. 2010; Westmoquette et al. 2013; Turner et al. 2015). Our K-band imaging (§ 2.3) likely traces hot dust emission, localized to the supernebula and extended up to $\lesssim$10 pc to its east. Based on numerical simulations, Silich et al. (2004) conclude that if the gas metallicity in the supernebula is enhanced to $1.5Z_{\odot}$, winds can be entirely inhibited by cooling. Turner et al. (2015) estimate that the metallicity of cloud D1 is the $\simeq$2-3$Z_{\odot}$, indicating that the SSC is near or above the critical cooling regime.

Recent modeling of cluster formation find that in the most massive and dense clusters, stellar winds and even SNe around individual stars can potentially stall due to radiative cooling, and fail to merge with their neighbors (Tenorio-Tagle et al. 2013, 2015; Silich & Tenorio-Tagle 2017; Wünsch et al. 2017; Silich & Tenorio-Tagle 2018). Our Br α observations, suggesting that the supernebula comprises thousands of individual H II regions rather than a single, merged giant H II region, is consistent with critically radiative winds/SNe around the SSC's massive stars. Indeed, NGC 5253 is in the critical density regime defined in Silich & Tenorio-Tagle (2017) in which it will retain its enriched stellar products due to wind stalling. The stalling mechanism can additionally explain the apparent lack of SNe signatures in the SSC without requiring an extremely young cluster age. Another massive embedded SSC, Mrk 71-A (in the dwarf starburst galaxy NGC 2366), is similarly found to exhibit no signs of a cluster-scale outflow or superwind (Oey et al. 2017). This cluster is analogous to NGC 5253, with a mass of M$\sim$$10^5$ $M_{\odot}$ and an age of $\lesssim$3 Myr. Whether the suppression of winds and resulting gas retention is standard for the most massive clusters, or whether there are other key factors such as host galaxy environment, remains a vital question in our understanding of cluster formation.

The ability of the embedded SSC in NGC 5253 to hold onto its enriched gas has significant im-

plications for the cluster's survival and potential evolution into GC. For one, continued formation of stars out of enriched material will lead to a spread in age and abundance in the stellar population, analogous to the multiple stellar populations inferred for many GCs (e.g., Renzini 2013; Piotto et al. 2015, and references therein). Moreover, the suppression of winds forces a slow expulsion of gas, preventing explosive dispersal. Removal of gas from the SSC could occur on a timescale much longer than the crossing time, allowing the cluster to respond adiabatically to changes in the gravitational potential. Along with a high star formation efficiency SFE$\gtrsim 50\%$ (Turner et al. 2015), the long gas removal timescale should allow the SSC to maintain most of its stars and remain bound, potentially surviving for Gyrs (e.g., Lada et al. 1984; Kroupa & Boily 2002; Goodwin & Bastian 2006; Bastian & Goodwin 2006; Baumgardt et al. 2008; Allison et al. 2010; Smith et al. 2013; Krause et al. 2012; Kim et al. 2016).

2.5.3 Origin for the Velocity Gradient Across the SSC

In § 2.4.2, we report a velocity gradient in the Br α core of $\simeq$2.4 km s^{-1} pc^{-1} from the NE to SW edges of the supernebula, oriented perpendicular to the NIRSPAO slits. We suggest the following possible explanations for this feature: bulk rotation of the cluster, an outflow from an embedded source in the cluster, or a foreground infalling gas filament.

2.5.3.1 Rotation of the SSC

Stellar dynamical studies of Galactic GCs have revealed that bulk rotation is common amongst the population (e.g., Kamann et al. 2018). These investigations find evidence for a correlation between the rotation and mass of GCs, consistent with a scenario in which a forming globular cluster inherits angular momentum from its collapsing parent molecular cloud. Simulations of massive cluster formation agree with this picture, finding rotation in newborn clusters (e.g., Lee & Hennebelle 2016; Mapelli 2017). Direct dynamical evidence for rotation exists for a handful of young massive clusters (YMCs). For example, R136 within the LMC exhibits a typical rotation velocity of $\sim$3 km s^{-1} based on stars within a radius of 10 pc (Hénault-Brunet et al. 2012). A velocity gradient of $\sim$1 km s^{-1} pc^{-1} is found for the stellar surface population in the Galactic

star-forming region L1688 (Rigliaco et al. 2016).

The magnitude of the Br α shift across the supernebula is similar to those measured in YMCs for which rotation is suggested. However, the mass of the SSC in NGC 5253 is orders of magnitude larger than that of such YMCs (which have M$\lesssim 10^4$M$_\odot$). The formation mechanism of SSCs is likely to differ from that of Galactic YMCs, along with the details by which angular momentum of the parent cloud is imprinted on the cluster as rotation. The CO(3–2) line, associated with hot cores and individual forming stars within the cluster, may show a slight systematic shift in its spatial centroid across the line, in the same sense as the Br α, with the bluer side of the line shifted about 0.″07 to the north of the red side of the line.

2.5.3.2 A Bipolar Ionized Outflow

The Br α gradient could alternatively provide evidence for a bipolar outflow oriented along NE-SW axis. The implied outflow is slow, traveling at a projected speed of $\sim$10 km s^{-1}, likely with a true velocity of up to a few tens of km s^{-1}. Bipolar ionized outflows are commonly observed around other massive protoclusters, and can be caused by a the breaking out of winds from an embedded source, such as a massive protostellar object with an accretion disk, or a star escaping from the cluster. The outflow could even be a supernova remnant that has punched through a low density channel in the SSC.

A similar ionized outflow is observed around the IRS2 protocluster in the Galactic star forming region W51 (Lacy et al. 2007; Ginsburg et al. 2016). The implied mass loss rate from this cluster is $\lesssim 10^{-3}$ M$_\odot$ yr^{-1}. NGC 5253 is an order of magnitude more massive than IRS2 and has an escape velocity that is correspondingly larger. At the same mass loss rate, only $\sim$2% of the $\sim$60,000 M$_\odot$ of gas in Cloud D1 would escape from the SSC over 1 Myr. Thus, the potential bipolar outflow is likely negligible in suppressing star formation, but could provide another channel through which the SSC enriches its environment.

2.5.3.3 A Foreground Redshifted Gas Filament

The nuclear starburst in NGC 5253 is thought to be fueled by infalling filaments of cold gas, as suggested by redshifted CO clouds extending hundreds of parsecs along the galaxy's minor axis, associated with a prominent dust lane (Meier et al. 2002; Turner et al. 2015). On smaller scales there are a number of filamentary CO(3–2) clouds detected within nucleus, one or more of which could be linked to a direct flow of gas into the central SSC (Turner et al. 2017; Consiglio et al. 2017). Most intriguing is Cloud D4, identified in Consiglio et al. (2017). Located $\sim$10-20 pc to the south of Cloud D1 and the supernebula, Cloud D4 hosts no obvious star formation, is $\sim 3\times$ more massive than Cloud D1, and is redshifted relative to it by $\sim$15-20 km s^{-1}. As apparent in Fig. 2.3, the CO(3–2) emission forms a bridge between clouds D1 and D4, possibly tracing gas accreting into D1 from D4.

The velocity gradient of Br α, redshifted in the SW relative to the NE, could be linked to infalling gas from Cloud D4. In this scenario the Br α originates in gas that is flowing from D4 to D1, ionized by the SSC. The observed gradient might then be due entirely to the gas inflow, although outflow from mechanical feedback in the NE is still possible. Unfortunately our NIRSPAO slits do not cover any positions to the south of the supernebula. Sensitive mapping of Br α across the region joining clouds D1 and D4, and around the other CO(3–2) clouds nearby, is necessary to provide more direct evidence of cold filament accretion.

2.6 Summary

We have obtained 0.″1 resolution NIRSPAO observations of the Br α 4.05 μm recombination line of the supernebula in NGC 5253, one of the most promising candidates for a young globular cluster. Our echelle spectra (R$\sim$25,000) taken with laser-guided AO on Keck II in four slit positions across the nebula allow for a detailed investigation of ionized gas kinematics in the region. Our findings are the following.

1. The K-band continuum peak is found to be coincident with the Br α peak within $\lesssim 0.''035$, or 0.6 pc. Thus the 2μm continuum is coincident with radio free-free emission, the "superneb-

ula" along with the molecular Cloud D1 (Turner et al. 2017). The peak lies in a region of high visible extinction, and we suggest that it is hot dust emission.

2. The visible nuclear SSC candidates #5 and #11 (Calzetti et al. 2015), are offset from the supernebula by 0.″35 (6 pc) and 0.″14 (2.6 pc), respectively. Given their separation, these sources are unlikely to power the luminous H II region. Cluster #5 coincides with a weak, secondary K-band peak.

3. The NIRSPAO spectra of the supernebula contain strong Br α emission, and He I emission that is $\sim$15$\times$ weaker. The Br α line exhibits a small core linewidth of FWHM$_{core}$=65-76 km s^{-1}. The profile is consistent with a collection of individual (non-overlapping) compact H II regions, embedded within the cluster and moving according to its gravitational potential.

4. A weak, broad pedestal is detected on the base of the Br α line, with a linewidth of 150-175 km s^{-1}. This feature could trace a population of massive stars expelling high-velocity winds that can escape the SSC.

5. The Br α emission is extended to the east of the supernebula, near cluster #5, and is redshifted by $\simeq$5-15 km s^{-1} relative to the supernebula. The extended gas is likely foreground to the supernebula and falling towards it. It remains unclear whether cluster #5 is indeed a star cluster which is in the process of merging with the central SSC, or a dense knot of gas/dust that reflects the visible light of the SSC and may be enriched with material that has been expelled from it.

6. The centroids of the narrow Br α component and the He I doublet exhibit a velocity shift of +13 km s^{-1} from the northeast to southwest edge of the supernebula. A similar velocity shift of smaller magnitude is seen in CO. The velocity profile is inconsistent with spherical expansion/outflow, but could be due to: rotation along the axis parallel to the slits, a biconical outflow from an embedded source breaking out of the cluster with a velocity of $\sim$10-50 km s^{-1}, or accretion of gas from a massive, redshifted molecular cloud to the south of Cloud D1.

We suggest that we see in the supernebula/Cloud D1 region the dynamics of individual ultra-compact H II regions around massive stars within the giant cluster that powers the supernebula. Winds and supernovae from these massive stars may be stalled due to critical radiative cooling, and cannot merge to generate a cluster-scale superwind. We detect two possible sources of outflow: the broad component of Br α along with the velocity gradient of the narrow component across the supernebula. Neither of these appear to be presently capable of rapidly removing a large amount of gas from the SSC. While NGC 5253 has been thoroughly studied, its context in the general formation of massive clusters (such as GCs) remains unclear. Is the embedded SSC unique in its lack of high-velocity gas dispersal, or is it typical of SSCs of a given mass along their evolutionary paths? Further high-resolution, infrared spectroscopic studies of forming massive clusters can probe ionized gas to sub-cluster scales, and peer past the veil of dust in which the stars of a young cluster are embedded.

Keck:II (NIRSPAO) IRAF, SAOImage DS9, Astropy (Astropy Collaboration et al. 2013)

CHAPTER 3

Unveiling Kinematic Structure in the Starburst Heart of NGC 253

This chapter presents a paper that has already been published on the kinematic structure of the nuclear starburst in the barred spiral galaxy NGC 253 (Cohen et al. 2020), an analog of the young Milky Way.

We investigate the kinematics of ionized gas within the nuclear starburst of NGC 253 with observations of the Brackett α recombination line at 4.05 μm. The goal is to distinguish motions driven by star-formation feedback from gravitational motions induced by the central mass structure. Using NIRSPEC on Keck II, we obtained 30 spectra through a $0\farcs5$ slit stepped across the central $\sim$5″×25″ (85 × 425 pc) region to produce a spectral cube. The Brα emission resolves into four nuclear sources: S1 at the infrared core (IRC), N1 at the radio core near nonthermal source TH2, and the fainter sources N2 and N3 in the northeast. The line profile is characterized by a primary component with $\Delta v_{\rm primary}\sim$90-130 km s^{-1} (FWHM) on top of a broad blue wing with $\Delta v_{\rm broad}\sim$300-350 km s^{-1}, and an additional redshifted narrow component in the west. The velocity field generated from our cube reveals several distinct patterns. A mean NE-SW velocity gradient of +10 km s^{-1} arcsec^{-1} along the major axis traces the solid-body rotation curve of the nuclear disk. At the radio core, isovelocity contours become S-shaped, indicating the presence of secondary nuclear bar of total extent $\sim$5″(90 pc). The symmetry of the bar places the galactic center near the radio peak TH2 of the galaxy rather than the IRC, and makes this the most likely location of a SMBH. A third kinematic substructure is formed by blueshifted gas on the southeast side of the IRC. This feature likely traces a $\sim$100-250 km s^{-1} starburst-driven outflow, linking the IRC to the galactic wind observed on kpc scales.

3.1 Introduction

The nuclear regions of disk galaxies are singular environments, in the sense that they serve as a distinct destination for the inward flow of matter in disk galaxies. Internal secular processes shape the continuing evolution of present-day disk galaxies (Kormendy & Kennicutt 2004). Radial gas flow induced by nonaxisymmetric structures such as bars, together with star formation and feedback from active galactic nuclei, all serve to shape a constantly evolving central mass structure in spiral galaxies.

Due to the inward flow of gas, barred galaxies often host intense nuclear star formation or starbursts, often taking the form of nuclear rings of super star clusters (SSCs; e.g., Athanassoula 1984; Buta & Combes 1996; Buta & McCall 1999; Böker et al. 2008; Comerón et al. 2010), as predicted by simulations (Athanassoula 1992; Shlosman 2002; Regan & Teuben 2003; Li et al. 2015; Sormani et al. 2018; Seo et al. 2019). Star formation in barred galaxies can serve as a sink of the inwardly drifting gas, thus preventing this gas from reaching a central supermassive black hole. However, star formation is never a pure gas sink; it is inefficient and can disperse gas via winds. Young SSCs are likely responsible for the multi-phase, large-scale galactic winds observed in starburst galaxies (e.g., Heckman 2001). Hydrodynamic simulations of barred galaxies find that such intense feedback can shape the growth of galactic bulges (e.g., Renaud et al. 2013; Athanassoula et al. 2013; Carles et al. 2016; Li et al. 2015; Seo et al. 2019). AGN feedback from an accreting SMBH can also regulate star formation in the galactic center and its host bulge (e.g., Robichaud et al. 2017). On the other hand, remnant, post star-forming molecular clouds can potentially assist the inward drift of their natal embedded clusters via a nuclear bar (Tsai et al. 2013). These are only a few of the possible effects governing gas flows and secular evolution in the centers of disk galaxies.

To investigate the processes of gas inflow and feedback in a barred galaxy, we have studied ionized gas kinematics in NGC 253, one of the closest starburst galaxies (D=3.5 Mpc; Rekola et al. 2005). NGC 253 is a nearly edge-on ($i = 78.5°$) spiral with a strong bar that feeds its nuclear starburst (e.g., Scoville et al. 1985; Peng et al. 1996; Arnaboldi et al. 1995; Engelbracht et al. 1998; Das et al. 2001; Paglione et al. 2004; Meier et al. 2015; Ando et al. 2017). The central $\lesssim$200 pc

region drives a galactic superwind to a distance of $\sim$10 kpc at hundreds of km s^{-1}(Weaver et al. 2002; Strickland et al. 2002; Westmoquette et al. 2011; Bolatto et al. 2013; Walter et al. 2017). The starburst region hosts two regions that could host the forming galactic center: the radio core with the brightest radio source in the galaxy ("TH2"; e.g., Turner & Ho 1985; Ulvestad & Antonucci 1997), and the IR core ("IRC"; e.g., Watson et al. 1996; Kornei & McCrady 2009). There are a number of candidate large star clusters detected as radio or sub-mm knots and associated molecular gas clumps, near the radio and IR core (Turner & Ho 1983, 1985; Ulvestad & Antonucci 1997; Leroy et al. 2018; Mangum et al. 2019).

The gas velocity fields of the nuclear region of NGC 253 are complex, resulting from combinations of distinct dynamical origin. The extended ionized gas takes the form of a wind that accelerates with distance from the galaxy (Westmoquette et al. 2011). At radii $\sim$10$''\simeq$170 pc, the ionized gas kinematics are consistent with solid-body rotation of the nuclear disk, with a velocity gradient along the galaxy major axis PA=51°. However at the radio core and to a lesser extent the IR core, the velocity field is dominated by a distinct pattern with a gradient nearly perpendicular to the major axis (Anantharamaiah & Goss 1996; Das et al. 2001; Rodríguez-Rico et al. 2006). These authors suggest that this central structure could trace outflow, an accreted object, or a secondary nuclear bar. The NGC 253 starburst powers a molecular outflow near the IR core (Weaver et al. 2002; Strickland et al. 2002; Bolatto et al. 2013; Walter et al. 2017). Kinematic evidence for nuclear outflow near the IRC were seen in high resolution Brackett γ observations by Günthardt et al. (2015, 2019); however, the location of the dynamical center of the galaxy remains ambiguous. Severe dust extinction ($A_V \gtrsim 20$) greatly complicates kinematic analysis of optical-NIR gas tracers.

In this project, the goal was to determine the dynamics of ionized gas in the starburst nucleus of NGC 253 and the forming star clusters using an emission line that is bright and relatively impervious to extinction. To this end, we observed the nucleus of NGC 253 with NIRSPEC on Keck II, obtaining slit-spectra of the Brackett α emission at 10 km s^{-1} resolution. Simultaneous imaging of the slit with SCAM allow registration of the slits spatially with respect to near-IR continuum emission. The resulting spectral cube covers the central $\sim$5 x 25$''$ (90 x 360) region with a 0$''$.5 slit, or ~ 8.5 pc at 3.5 Mpc.

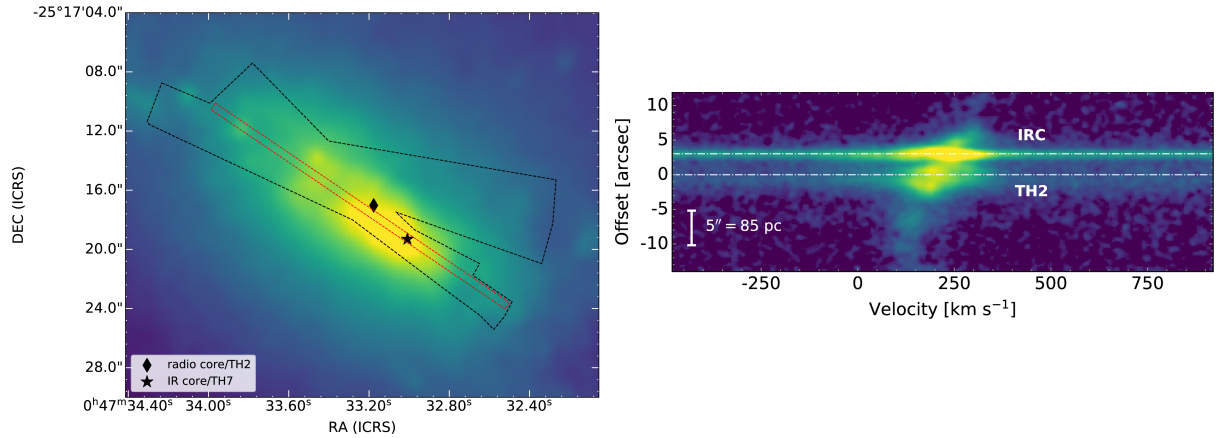

Figure 3.1: NIRSPEC observations of the starburst in NGC 253. *Left*) Stacked SCAM image of the K-band continuum (color), with the region bounded by all slits in our map (black outline). The nonthermal source TH2 at the starburst's radio peak, along with the IR peak in the IRC, are marked by diamond and star symbols, respectively. *Right*) Reduced 2D echelle spectrum from the single, central slit position highlighted in red on the left. The spectrum runs from NE to SW in the positive vertical direction, with the position of TH2 set as the origin. The brightest Br α emission is detected at the radio core (near TH2) and at the IRC. The spectrum displayed here was combined with the remaining 30 spectra acquired across the region to generate a Br α data cube (Sec. 6.2).

3.2 Observations and Data

We observed NGC 253 with NIRSPEC on Keck II (McLean et al. 1998) in the first half-night on Dec 7, 2017. Observing parameters and properties of NGC 253 are reported in Table 3.1. Spectra were taken in high-resolution (echelle) mode in the KL band, using the $0\farcs432\times24''$ slit. The echelle and cross-disperser angles were set to 64.42° and 34.3°, respectively, yielding a wavelength coverage of 4.031-4.086 μm in the 19th echelle order. The seeing ranged between $0\farcs7$ and $1\farcs1$.

We obtained a total of 31 120s exposures at slit positions spanning the central $\sim 18''\times30''$ of the nuclear region, shown in Figure 3.1. We initially orientated the slit along the galaxy's major axis, at PA$\simeq$45°. The slit PA drifted with Earth's rotation such that the slits for our final exposures were oriented at PA$\simeq$80°. Sky spectra were acquired by offsetting away from NGC 253 after the 8th science exposure and again after the final science exposure. Two calibration stars were observed prior to and after completing all NGC 253 observations (HD225200 and HD12365, respectively). Images of the slit on the sky in the K band were simultaneously acquired using the NIRSPEC Slit-Viewing Camera (SCAM). These images allowed for registration of the slits with respect to the near-IR background. In this way we were able to build a cube.

Each slit position yielded a 2D echelle spectrum which we rectified, reduced, and calibrated,

Table 3.1: Properties of NGC 253 and its two brightest nuclear sources, along with the NIRSPEC observing parameters.

Distance and angular scale	3.5 Mpc; 1″=17 pc[(1)]
Inclination of galactic disk i	78.5°[(2)]
PA of disk major axis	51°
PA of bar major axis / x_1 orbits	70°
PA of bar minor axis / x_2 orbits	45°
Systemic velocity (heliocentric) $v_{\rm sys}$	226 km s^{-1}[(3)]
Ionized galactic wind inclination	12°[(4)]
PA of galactic wind	140°
Opening angle of galactic wind	60°
Outflow speed of galactic wind	$\gtrsim$100-300 km s^{-1}
Predicted SMBH mass $M_{\rm BH}$	$\sim 2 \times 10^7$ M$_\odot$[(5)]
Radio center, source TH2 (ICRS)	$00^{\rm h}47^{\rm m}33\overset{s}{.}18$, $-25°17'16\overset{''}{.}94$[(6)]
Radio core mass $M_{\rm dyn}^{\rm TH2}$	$\sim 7 \times 10^6$ M$_\odot$[(7)]
Infrared center, IRC (ICRS)	$00^{\rm h}47^{\rm m}32\overset{s}{.}99$, $-25°17'19\overset{''}{.}74$[(8)]
IRC mass $M_{\rm dyn}^{\rm IRC}$	$\sim 5 \times 10^5$ M$_\odot$[(9)]
Observing wavelength	$\lambda = 4.052$ μm
Slit size	$0\overset{''}{.}432 \times 24''$
Echelle angle	64.42°
Cross-disperser angle	34.3°
Seeing	$0\overset{''}{.}7$-$1\overset{''}{.}1$
Velocity resolution	12 km s^{-1}
Mapping Area	$\sim 18'' \times 30''$[(10)]
Total exposure time	64 min[(11)]
Peak pixel S/N ratio	7-72[(12)]

[(1)] Rekola et al. (2005). [(2)] Galactic disk and bar properties adopted from Das et al. (2001), Paglione et al. (2004) and references therein. [(3)] This paper, Sec. 3.3.2.1.
[(4)] Ionized wind properties from Westmoquette et al. (2011) modeling of Hα outflow cone.
[(5)] Predicted using M-σ relation (Combes et al. 2019) with measured NGC 253 bulge stellar velocity dispersion from Oliva et al. (1995). The presence of a SMBH in NGC 253 is expected but unconfirmed. [(5)] Coordinates of radio peak in NGC 253, identified as nonthermal source TH2 in Turner & Ho (1985). [(6)] Estimate from Rodríguez-Rico et al. (2006) within $r < 7$ pc of TH2, using H92α mapping with a $\lesssim 0\overset{''}{.}5$ beam. [(7)] Coordinates of IR peak (IRC) from Leroy et al. (2018), their source #5. Coincident with thermal source TH7 (Turner & Ho 1985).
[(8)] Virial mass estimate from Leroy et al. (2018) using the resolved source size of 2.1 pc.
[(9)] Size of the NIRSPEC mapping region, with 31 slit positions.
[(10)] Combined NIRSPEC exposure time for all spectra across the nuclear starburst.
[(11)] Signal-to-noise ratio (S/N) of the brightest pixel in echelle spectra.

using our calibration star spectra along with arc lamp spectra acquired at the beginning of the night. We first subtracted raw NIRSPEC images by sky spectra, divided by a median-normalized flat-field image, and iteraitvely removed hot/cold pixels. We then spatially and spectrally rectified the images using an `Python`-based implementation the `REDSPEC` reduction code[1]. The reduced echelle spectra have spatial information in the vertical axis (along the slit) and spectral information in the horizontal axis, as shown by the example spectrum in Fig 3.1. Each pixel has a size of 5.482×10^{-5} μm along the spectral axis and $0\farcs192$, the nominal value, along the spatial axis. The spectral resolution is about 3 pix $\simeq$ 12 km s^{-1}.

3.2.1 The NIRSPEC Cube

To take full advantage of our data set, we combined the separate spectra into a spectral cube, with RA/DEC on the x- and y-axes and wavelength/velocity along the z-direction. Constructing the data cube involved mapping between pixels in each 2D spectrum and pixels on the cube grid, requiring astrometric registration of the slits. Registration was performed by creating a stacked, slit-free SCAM image in which a handful of IR sources are well-detected (Fig. 3.1). To create the stacked image, we sky-subtracted, rotated, and aligned all individual SCAM exposures (showing the slit trace) to a common reference image. We then masked out the slit trace in each image and median-combined all images of acceptable quality. During this process we tracked the position of each slit, shifting and rotating to the reference image. Once the stacked image was obtained, we measured the pixel positions of detected K-band sources, and matched them with sources with known sky coordinates detected in an archival HST F160W image (Proposal ID 12206, PI Westmoquette), yielding registration of the SCAM image and HST images accurate to $\lesssim0\farcs1$ (rms error).

Inferring the pixel mapping for each spectrum requires identification and measurement of a reference point, in addition to the sky positions of the slits (the center of the slit does not correspond to the center of the rectified spectrum). As such, we measured the pixel positions of Br α sources in each spectrum that we could match to known sources detected in the NIR imaging, and established the reference pixel required to map spectrum pixel coordinates to sky coordinates.

[1] `https://www2.keck.hawaii.edu/inst/nirspec/redspec.html`

After registration, we constructed the NIRSPEC cube in the following way. First, we interpolated each echelle spectrum across the slit width, assuming a constant light profile in that direction, and then mapped the data from each pixel in each wavelength slice onto the coordinate frame of the cube. We median-binned the mapped data to a regular grid, and applied smoothing with a Gaussian kernel to remove small-scale artifacts resulting from regions with sparse data. Finally, we interpolated each image slice to the final grid with a spatial scale of $0\farcs12$ pix^{-1}. The spatial resolution of the cube is $\simeq 1\farcs0$, approximately the same as in individual spectra. A map of the Brackett line emission was generated by fitting continuum-only pixels with a first order polynomial and subtracting this contribution from the data cube. The Br α cube is shown with channel maps in Figure 3.2.

3.3 Results

The cube of Br α emission in the starburst core in NGC 253, shown in Figure 3.2, reveals four sources within our slit coverage. We identify these sources as S1, N1, N2, and N3 from the SW to NE along the major axis, and label them on the velocity-integrated Br α intensity map in Figure 3.3.

Source S1 is at the IR core (IRC), a region hosting the starburst's brightest NIR source, a $\sim$6 Myr old, $M \sim 10^6$ M$_\odot$ SSC (e.g., Watson et al. 1996; Kornei & McCrady 2009; Fernández-Ontiveros et al. 2009; Davidge 2016; Günthardt et al. 2019). Several other candidate SSCs are identified near the bright SSC as fainter thermal IR-radio continuum knots (e.g., Fernández-Ontiveros et al. 2009; Günthardt et al. 2015; Leroy et al. 2018). Broad recombination lines suggest an ionized outflow driven by the SSC formation near the IRC (Günthardt et al. 2019). We assume Brackett source S1 primarily traces the HII region excited by the bright SSC in the IRC, with small contributions from fainter HII regions around nearby clusters.

Source N1 is associated with the radio core, which contains the galaxy's brightest radio source, TH2 (Turner & Ho 1985). TH2 is characterized by non-thermal radio continuum with brightness temperature $\gtrsim$50,000 K (Turner & Ho 1983, 1985; Ulvestad & Antonucci 1997), and no clear infrared counterpart (Günthardt et al. 2015), thus is unlikely to be an HII region. While its origin remains unclear, the bright radio source TH2 is potentially linked to the presence of a supermassive

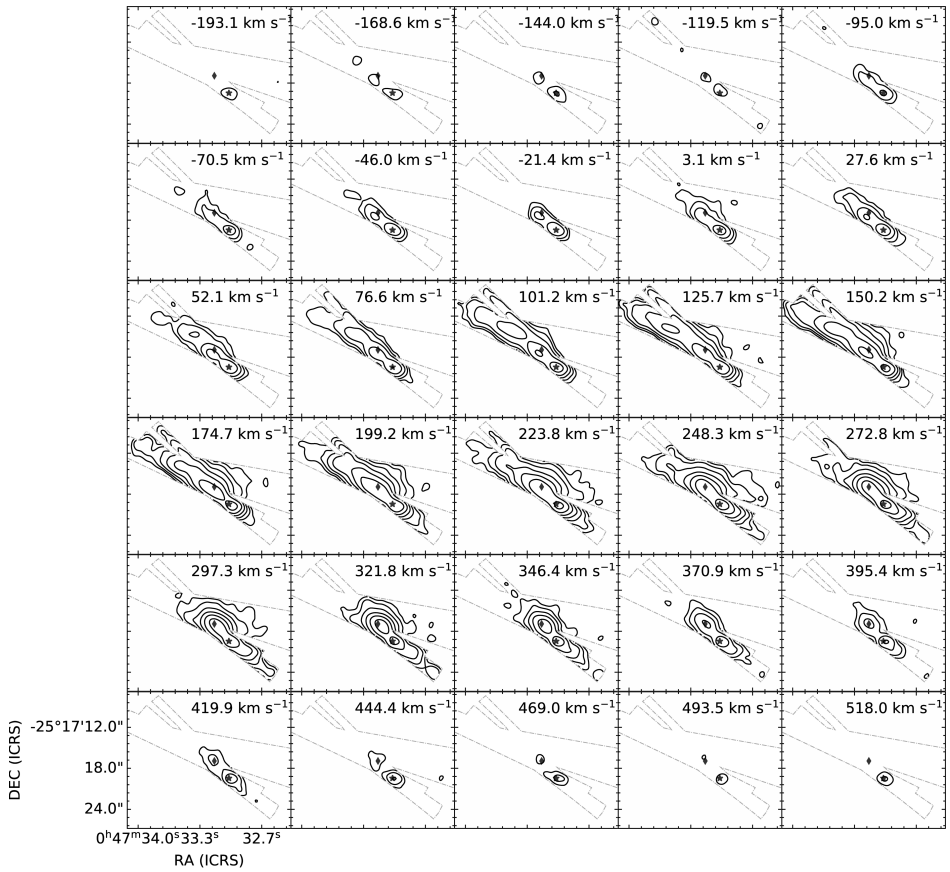

Figure 3.2: Channel maps of the NIRSPEC Br α cube. To produce this figure, channels are bin-averaged by 6 pixels, to a width of $\Delta v = 24.5$ km s^{-1}. Contours show $\sigma_{\rm rms} \times 2^{n/4}$, $n = 6, 10, 14, 18, ..., 44, 48$, where $\sigma_{\rm rms}$ is the rms noise in channels away from the Br α line. As in Fig. 3.1, the IRC and TH2 are marked as the star and diamond symbol, respectively. Four Br α sources are identifiable in these maps: a bright peak near IRC that has a broad component visible across all channels, another bright/broad source at the radio core near TH2 with an apparent gradient, a third clump of narrower emission to the NE of TH2 (apparent at 101.2 km s^{-1}), and a fourth clump towards the NE corner of the FoV (apparent at 52.1 km s^{-1}).

black hole (Turner & Ho 1985; Müller-Sánchez et al. 2010). Brackett source N1 should also trace candidate SSCs and their HII regions within the radio core, identified as compact thermal IR-radio sources (e.g., Turner & Ho 1985; Ulvestad & Antonucci 1997; Leroy et al. 2018; Mangum et al. 2019). The line profile of ionized gas within the radio core, only possible with spectroscopy at K band or longer wavelengths, has been measured for RRLs (Rodríguez-Rico et al. 2006; Kepley et al. 2011; Bendo et al. 2015) and IR emission lines (e.g., Rosenberg et al. 2013; Günthardt et al. 2015).

N2 and N3 comprise weaker Br α emission compared to N1 and S1, and are possibly linked to Günthardt et al. (2015) sources A5-6 and A3/10, respectively. Optical source 'spot *a*' from Watson

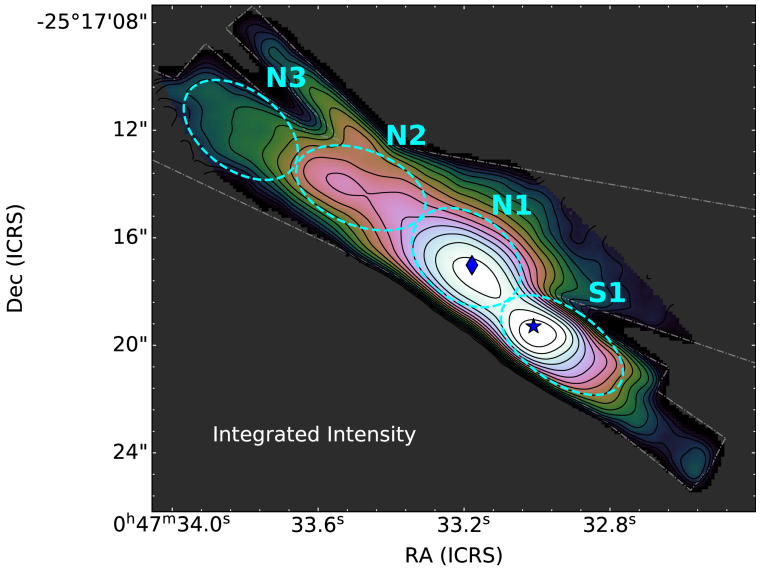

Figure 3.3: Velocity-integrated Brackett α emission (line flux map) in the core of NGC 253, generated from the NIRSPEC cube by summing pixels at $>1.5\sigma_{\rm rms}$ along the spectral axis. The slit coverage is indicated by the grey outline, and the IR core and TH2 are again marked as the star and diamond symbols, respectively. We detect four likely distinct Brackett sources: N3, N2, N1, and S1 (dashed cyan ellipses). The elliptical apertures shown here are used to extract the total spectrum of each source.

et al. (1996) might also contribute to the emission near N2 and N3.

3.3.1 Brackett Line Profile

Figure 3.4 shows the Br α profiles for S1, N1, and N2, N3 averaged over the $\sim 2\farcs4 \times 1\farcs4$ apertures in Fig. 3.3. To characterize the line profile, we first fit each spectrum with an oversimplified model of a single-component Gaussian profile and infer velocity centroids and line widths. We also estimated Br α equivalent width, a proxy for age in young massive clusters, by dividing these models by the best-fit models of the continuum (Sec. 3.2.1) and integrating over the line. The single-component models reveal a shift in Br α velocity centroid by roughly $+120$ km s^{-1} from N3 to S1 along with broad linewidths reaching FWHM$\sim$200 km s^{-1} near N1 and S1. Equivalent width is largest for N1, $W() \sim 250$Å, and decreases to $W() \sim 100 - 150$Å for S1, N2, and N3.

More realistic models of the Br α line comprising two or three Gaussian components rather than one, selected using the Bayesian Information Criterion, are shown in Fig. 3.4. Parameters for each component of these models are reported in Table 3.2. Generally the profile is characterized by a broad component (FWHM$_{\rm broad}$ $\sim$ 300-350 km s^{-1}) at the base of a primary emis-

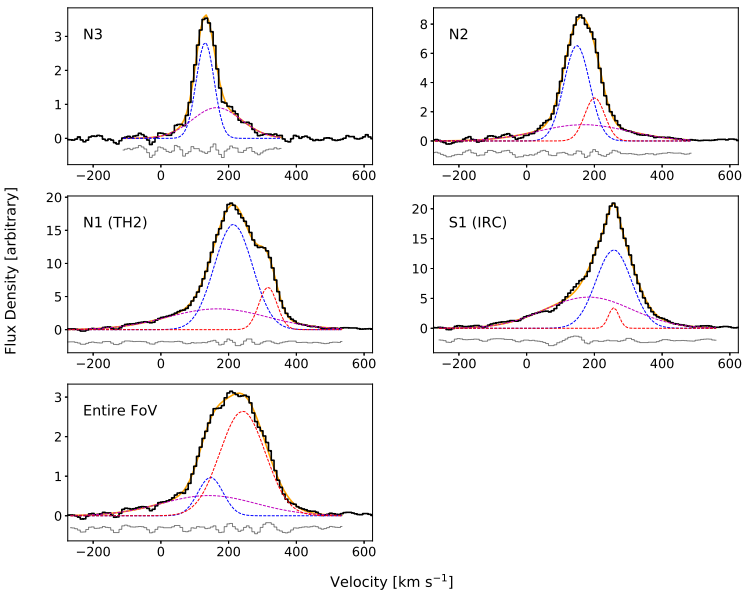

Figure 3.4: Br α spectrum of identified sources (along with the entire imaged region) and best-fit Gaussian models of the line profiles. Spectra (black line) were extracted by summing all pixels within apertures (Fig. 3.3) along the spatial dimensions of the Br α cube. Intensities in all panels are scaled by a common normalization factor. With clear asymmetries and structure in the line profiles, none of the sources can be modeled well with a single-component Gaussian profile. Models with two or more Gaussian components provide much better fits to the data, as shown in each panel by the best-fit model (solid orange line), its individual fit components (dashed lines), and the fit residuals (grey curve). All sources exhibit a "primary" bright peak component and a "broad" component that may appear as a blue wing extending out to large negative velocity away from line center with weak, if any, corresponding emission on the red side. A third, "narrow" and red component is additionally required to model N2, N1, and S1.

sion peak (FWHM$_{\rm primary}$ $\sim$ 90-130 km s^{-1}). The broad emission has the highest intensity and largest linewidth for sources N1 and S1 at the radio and IR cores, respectively, where it appears almost exclusively on the blue side of the line. A blue wing is similarly exhibited by the Br γ line in this region (Günthardt et al. 2019) and by Hα tracing more extended gas in regions of low extinction (Westmoquette et al. 2011). Blue wings are common in nebular lines from starburst regions, and suggest that extinction may be blocking the red wing from view, so these linewidths are lower limits. In addition to the broad and primary components, the line shows a third, narrow (FWHM$_{\rm narrow}$ $\sim$ 60 km s^{-1}) component strongest near N1 with a peak reaching an offset of $\Delta v_{\rm n,p} \equiv v_{\rm narrow} - v_{\rm primary} \simeq +100$ km s^{-1} from the primary component. The Br γ line shows evidence of this narrow feature, however it is not identified as a distinct peak (Günthardt et al. 2019).

Table 3.2: Properties of Brα sources identified in Fig. 3.3. Sky coordinates are based off of best-fit 2D profiles, while kinematic properties are from the best-fit Gaussian models shown in Fig. 3.4.

Source	0^h47^m (ICRS)[(1)]	-25°17′ (ICRS)	$v_{primary}$ [km s^{-1}][(2)]	FWHM$_{primary}$ [km s^{-1}][(3)]	$F_{primary}/F_{tot}$[(4)]
N3	$33^s.83$	12″	131 ± 2	62 ± 7	0.53
N2	$33^s.52$	14″	148 ± 14	89 ± 14	0.51
N1 (radio core)	$33^s.16$	17″	214 ± 1	133 ± 4	0.59
S1 (IRC)	$33^s.01$	19″	257 ± 1	123 ± 4	0.49

v_{broad} [km s^{-1}][(5)]	FWHM$_{broad}$ [km s^{-1}][(6)]	F_{broad}/F_{tot}[(7)]	v_{narrow} [km s^{-1}][(8)]	FWHM$_{narrow}$ [km s^{-1}][(9)]	F_{narrow}/F_{tot}[(10)]
165 ± 13	170 ± 23	0.47	...	...	...
168 ± 11	313 ± 35	0.30	201 ± 14	69 ± 14	0.18
168 ± 6	347 ± 14	0.30	316 ± 1	63 ± 2	0.11
182 ± 5	301 ± 7	0.47	257 ± 1	36 ± 4	0.04

[(1)] Source centroid coordinates have a 1-σ uncertainty of $\sim$1″. [(2),(5),(8)] Centroid velocity (heliocentric) for each Gaussian component of the best-fit two- or three-component model. The components are labeled as "primary", "broad", and "narrow" (the narrow component can be fit to all but source N3). [(3),(6),(9)] FWHM of each Gaussian component in the best-fit model. [(4),(7),(10)] Fraction of total line flux in each component of the best-fit model (ratio of each component flux that to the summed flux of all components).

While insightful, the average line profiles (Fig. 3.4) blend together systematic motions within the $\sim 2''$ apertures used for extraction. Figure 3.5 shows the line profile mapped across the central region. This map reveals a major axis velocity shift consistent with the change in line centroid between the sources, with velocity increasing (redshifted) from NE to SW. The picture is most complicated near N1, where the narrow third component is strongest. Interestingly, $\sim 0\farcs8$ east of TH2, the narrow red component reaches a peak intensity that is $\sim 1.4\times$ higher than that of the the primary component at that location. This narrow red feature could be a kinematically distinct source or a portion of a larger gas flow. We note that the irregular line profile near TH2 suggests the possibility of >3 components that would require higher resolution to distinguish and characterize.

The spectrum map (Fig. 3.5) also show that the broad blue wing increases in strength to the south and east of the peak positions in both N1 and S1, with a peak just east of S1, where the feature contributes $\sim 50\%$ of the line flux. The velocity centroid of broad emission reaches a minimum of $\Delta v_{\rm b,p} \equiv v_{\rm broad} - v_{\rm primary} \simeq -90$ km s^{-1} at a distance of 1-$1.5''$ around the eastern side of the IRC, corresponding to the panels immediately to the left of S1 in Fig. 3.5. Moving NE away from S1, the offset shifts positively, reaching $\Delta v_{\rm b,p} \sim 0$ km s^{-1} in the region north of N1 and west of N2 (in Fig. 3.5, panels above N1 and to the right of N2). Further NE, the broad component becomes a *red* wing with $\Delta v_{\rm b,p} \gtrsim 0$ km s^{-1} near N2 and N3 (any panels to the left of N2 in Fig. 3.5). This change in $v_{\rm b,p}$ is due to the major-axis shift in the primary component, while the broad component centroid remains constant to within $\lesssim$20 km s^{-1}. Nonetheless, the broad component shows a clear blueshift to the SE of N1 and S1, explaining the -90 km s^{-1} offset near the IRC. Heavy extinction near the IRC and radio core can explain the much of the blue-red asymmetry of the broad feature; the observed blue wing may not reflect the full kinematic structure.

3.3.2 Nuclear Velocity Structure

The NIRSPEC cube (Fig. 3.2) allows us to probe the detailed ionized gas kinematics using the standard methods of spectral cube analysis. First and second moment maps, representing the intensity-weighted line-of-sight velocity field and dispersion, respectively, were generated from the Br α cube using pixels at $> 6\sigma_{\rm rms}$ to identify distinct patterns in the velocity structure (Figure 3.6).

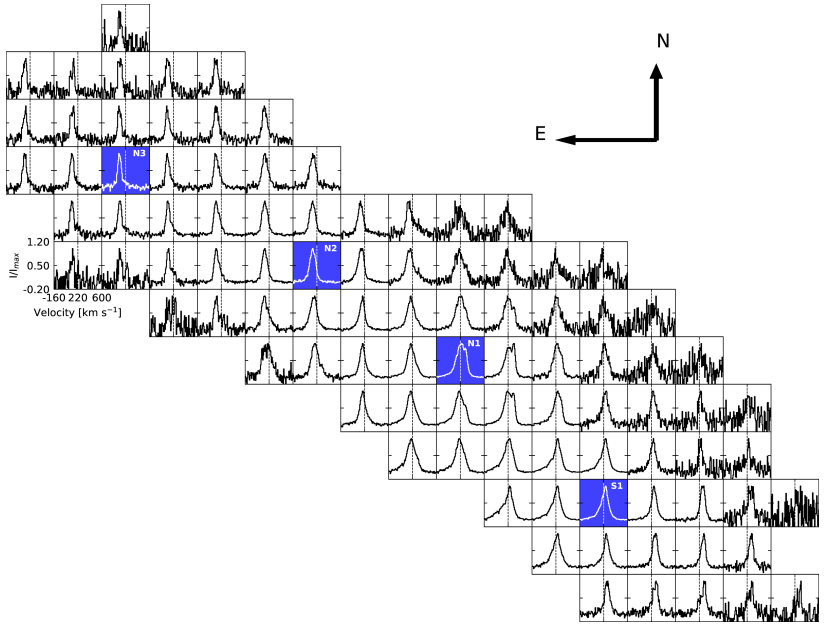

Figure 3.5: Map of Br α line profile across the NIRSPEC FoV. Each panel gives the summed spectrum within a $1\farcs2 \times 1\farcs2$ box centered at that location, and each of these spectra are individually normalized so that variation of the line shape across the region is clear (line peak intensities should not be compared between panels). Blue-highlighted panels show the location of Br α sources. The velocity axis is identical for all spectra, with a vertical line marking the heliocentric systemic velocity $v_{\rm sys} = 220$ km s^{-1}. Kinematic patterns are clear, in particular: an increase in strength of the broad blue component towards the SE, a double-peaked line structure just east of TH2, and a bulk shift in the line peak velocity centroid to higher velocity (redshift) from NE to SW, along the major axis.

3.3.2.1 Major-axis Velocity Gradient

The velocity field in Fig. 3.6 is complex, comprising several distinct kinematic structures rather than a single ordered pattern. The simplest of these structures is apparent as the velocity contours at the NE and SW edges of the field (away from TH2 and IRC). Perpendicular to the major axis, these contours indicate a positive gradient from NE to SW across the central $\sim$12$''\simeq$200 pc (projected). This signal is washed out near N1 and S1, where other kinematic structures clearly dominate the velocity field.

To further probe the rotation curve, we generated a PV image using a pseudoslit centered on TH2 oriented parallel to the major axis, at PA=51°. The resulting major-axis PV diagram (Fig. 3.7, left) more clearly exhibits solid-body rotational pattern across the regions of more complex kinematic structure. The major-axis rotation curve, or 1D velocity profile, is derived from best-fit models of multi-component Gaussian profiles to the spectrum in each column of the PV image.

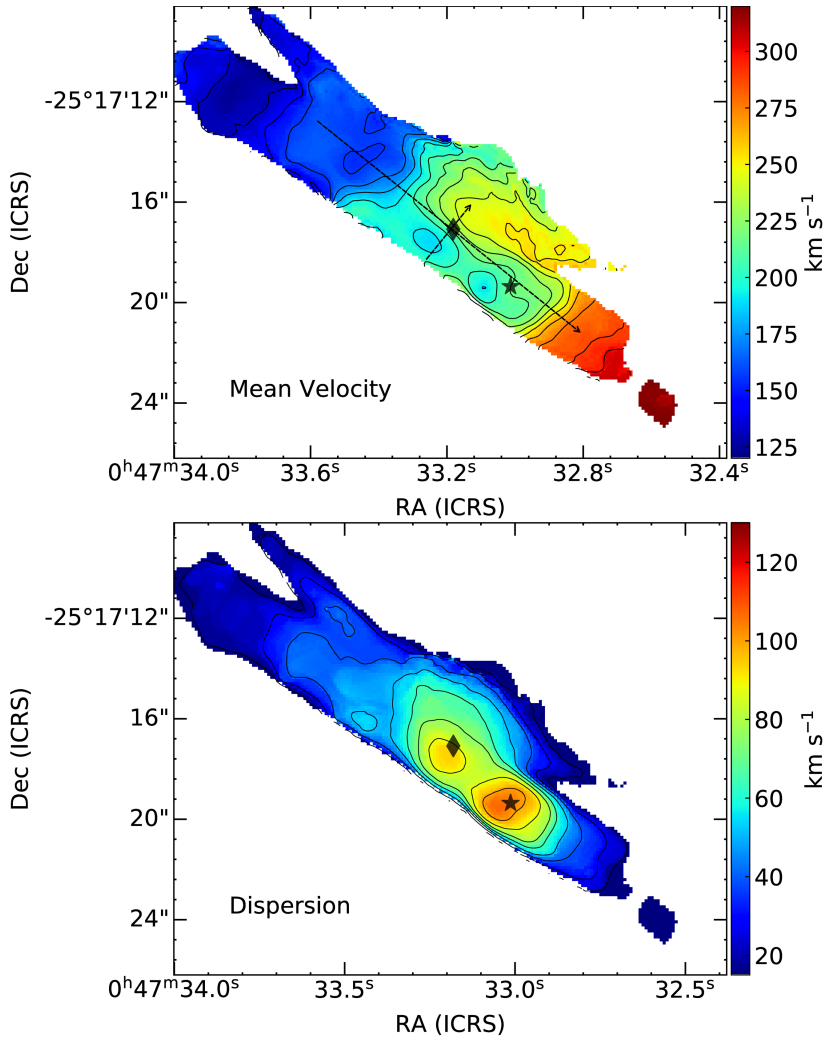

Figure 3.6: Velocity field of the nuclear region in NGC 253. The upper and lower panels show the intensity-weighted mean velocity (first moment) and dispersion (second moment, equivalent to the linewidth σ_v), respectively. Both maps were generated from the NIRSPEC cube using pixels detected at $> 6\sigma$. Contours mark intervals of 12 km s^{-1} and 10 km s^{-1} in the upper and lower panels, respectively. As in other figures, the star marks the IRC and the diamond marks the radio peak TH2. The dashed arrows mark pseudoslits used to generate major- and minor-axis PV images.

We take the primary fit component (as opposed to the broad wing or red narrow component) to generate the curve shown in the right-hand panel of Fig. 3.7. The best-fit velocity gradient is 10 km s^{-1} arcsec^{-1}. A major-axis gradient of this magnitude has been well-measured with many gas tracers, including in RRLs (Anantharamaiah & Goss 1996; Rodríguez-Rico et al. 2006), Br γ, H_2, and CO (Engelbracht et al. 1998; Günthardt et al. 2015; Leroy et al. 2015).

From Fig. 3.7 it is clear that the major-axis velocity profile of the primary Br α component is more complex than a simple gradient from solid-body rotation. The residuals show a sinusoidal

structure seemingly associated with sources; the largest residual peaks slightly precede positions of N1/TH2 and S1/IRC. Best-fit sinusoidal curves indicate residual amplitudes of 17 km s^{-1} and 12 km s^{-1} for N1 and S1, respectively. For both sources, residual peaks are offset by about $0\farcs5$ NE of the emission peaks (TH2 and IRC). This results in velocity gradients across the radio and IR cores of approximately -20 km s^{-1} arcsec^{-1} and -15 km s^{-1} arcsec^{-1}, flipped with respect to the underlying 10 km s^{-1} arcsec^{-1} gradient. Similar major-axis velocity residuals were reported in Anantharamaiah & Goss (1996) and Günthardt et al. (2015).

The kinematic center, systemic velocity, and position angle of the nuclear disk rotation are estimated using BBarolo (Di Teodoro & Fraternali 2015) to fit a tilted-ring model to the velocity field, with inclination fixed to $i = 78.5°$. The best-fit model has center ($\alpha_{\rm icrs}$, $\delta_{\rm icrs}$)=($00^{\rm h}47^{\rm m}33.09^{\rm s}$, $-25°17'17\farcs8$) with an uncertainty of $\sigma \simeq 1''$, $v_{\rm sys} = 226 \pm 11$ km s^{-1}, and PA $\phi_d = 51 \pm 6°$. The disk PA and systemic velocity are in close agreement with the literature (e.g., Anantharamaiah & Goss 1996; Das et al. 2001). The dynamical center is within $\lesssim 0\farcs7$ of previous determinations (Anantharamaiah & Goss 1996; Müller-Sánchez et al. 2010; Rosenberg et al. 2013), and is $\simeq 1\farcs5$ closer to TH2 than to the IRC. We note that tilted-ring modeling is limited in its ability to explain the nuclear kinematics, due to the significant non-rotational structure present in the velocity field.

3.3.2.2 Substructure of the Radio Core and Source N1

The most prominent pattern in the velocity field (Fig. 3.6) comprises the S-shaped velocity contours at source N1, centered close to the radio peak TH2. This kinematic substructure has a characteristic size of $\sim$2-3$''\simeq$30-50 pc, based on the contours. Unlike the underlying solid-body rotation pattern, the contours of N1 are nearly parallel to the major-axis, implying a velocity gradient of $\sim$+50 km s^{-1} arcsec^{-1} from SE to NW along the minor axis. Again, the Br α velocity structure is consistent with prior measurements of RRLs: Anantharamaiah & Goss (1996) find a minor-axis gradient of $\sim$20-30 km s^{-1} arcsec^{-1} for H92α, Rodríguez-Rico et al. (2006) similarly find a 25 km s^{-1} arcsec^{-1} for H92α but infer a larger value of 42 km s^{-1} arcsec^{-1} for H53α, closer to our estimate. The K band velocity fields presented in Rosenberg et al. (2013) are the closest comparison to our Br α field; their H_2 field resolves the same three substructures identified in our

map. Interestingly, their stellar velocity field also shows the S-shaped velocity contours, suggesting a common dynamical origin for the gas and stars in the radio core.

In the major-axis PV image (Fig. 3.7, left), source N1 is resolved into two bright components connected by fainter emission surrounding a central "hole". The bright components here were identified as the primary and narrow red component in the Br α line profiles (Fig. 3.4). The pv "hole" is centered at a position $\simeq$0.7-0.8$''$ to the SW of TH2 and heliocentric velocity $v \simeq 230$ km s^{-1}, with an extent of $\Delta x \sim 2''$ along the position axis and $\Delta v \sim$100 km s^{-1} along the velocity axis. This structure is likely related to the local maximum in velocity dispersion near TH2 (Fig. 3.6), which reaches $\sigma_v \simeq 90$ km s^{-1}. The major-axis PV morphology suggests that the radio core can be characterized by a single dynamical structure.

A PV image was extracted along the minor-axis (PA=141°) from a pseudo-slit centered on TH2 (Fig. 3.7, middle). The emission along this axis is resolved into the primary bright core following a steep velocity gradient, the extended blue tail on its SE side, and the red component in a bright clump on the NW side. The minor-axis velocity curve of the primary component, extracted in the same way as the major-axis velocity curve, is linear within [-0.″6,0.″6] of TH2 (Fig. 3.7) with a best-fit gradient of $+41$ km s^{-1} arcsec^{-1} from SE to NW. This gradient, however, spans a distance only slightly larger than the spatial resolution of our data. The true velocity curve for for R$\lesssim$5-10 pc might have an even steeper gradient or significantly depart from a linear profile, but such structures would be smeared out in our NIRSPEC cube. Indeed, Rodríguez-Rico et al. (2006) measure a minor-axis gradient of 110 km s^{-1}arcsec^{-1} in a high-resolution map ($\sim$0.″3 beam) of H92α.

3.3.2.3 Substructure of the IR Core and Source S1

A third, distinct kinematic substructure is exhibited by the velocity field of S1 as an arc of blue-shifted emission around the east side of the of the IRC (Fig. 3.6, top). The S1 blue flow corresponds to the maximum velocity dispersion in the NIRSPEC FoV, reaching $\sigma \simeq 110$ km s^{-1} (Fig. 3.6, bottom). The gas within the blue knot reaches a maximum LoS velocity shift of $\Delta v = -20$ km s^{-1} at distance of about $0.''8$ from the IRC peak. RRL velocity fields show a "kink" in the contours near

the S1 region likely related to this feature (Anantharamaiah & Goss 1996; Rodríguez-Rico et al. 2006). The blue wing in Figs. 3.4 and 3.5 contributes the most to the Br α line profile at the location of the blue flow, suggesting that these features are physically related.

The major-axis PV diagram (Fig. 3.7, left) detects S1 as a single brightest emission peak with broad, extended curved wings on both the red and blue sides of the line. The central peak shows a velocity gradient with opposite orientation to the smooth major-axis gradient, which is exhibited in Fig. 3.7, right, as a residual from the linear fit at $x \simeq 3''$, corresponding to a -15 km s^{-1} arcsec^{-1} gradient across the IRC. Günthardt et al. (2015) finds a similar negative gradient of about -20 km s^{-1} arcsec^{-1} for the $\sim$1.5$''$ across the IRC in their H_2 rotation curve. Unfortunately the NIRSPEC slit coverage does not extend more than $\sim$1-1.5$''$ to the SE side of the IRC, such that we cannot determine if the blue flow in Fig. 3.6 is part of a larger kinematic substructure.

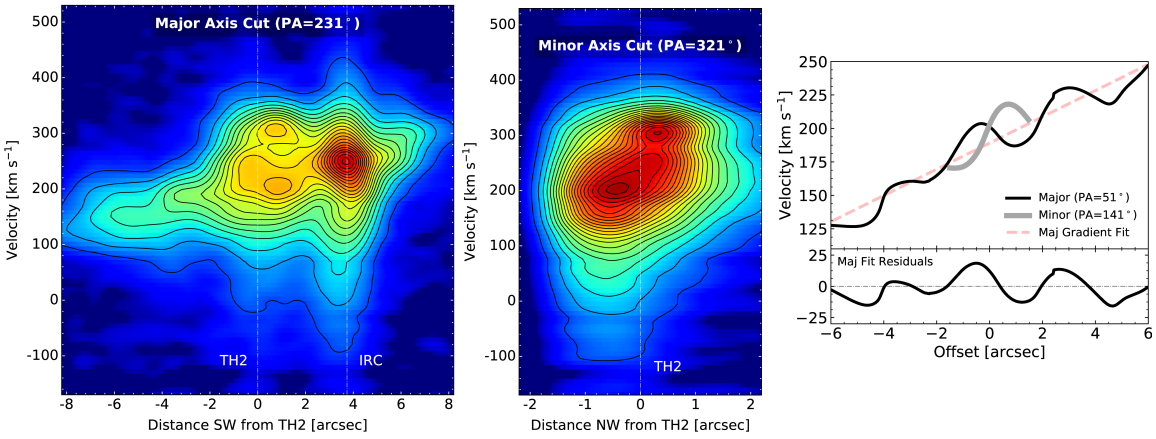

Figure 3.7: Position-velocity images along the major (left panel) and minor axes (middle panel), along with velocity profiles extracted from these PV images (right panel). The pseudoslits used to generate the PV images, shown in Fig. 3.6 as dashed black arrows, are centered on the radio peak TH2, which corresponds to $x = 0$ in all panels. The IRC/radio source TH7 is at a position $x \simeq 3\farcs3$ in the major-axis diagram.

3.4 Discussion

Kinematic structures in the Br α velocity field (Figs. 3.6 and 3.7) are linked primarily to the brightest sources sources in the region: N1 at the radio core and S1 at the IR core. These gas motions reflect the fundamental, complex mechanisms of secular galaxy evolution and the mass evolution of the centers of galaxies.

3.4.1 Gaseous Bar Structure Near the Radio Nucleus

The strongest kinematic substructure, associated with N1, is distinguished by S-shaped velocity contours. S-shaped contours are characteristic of motion in a barred potential (e.g., Athanassoula 1984; Athanassoula & Bureau 1999; Kormendy & Kennicutt 2004).

Contours in the Br α velocity field (Fig. 3.6) are oriented at PA$\simeq$45°, close to the disk major-axis (PA=51°) and aligned with the nuclear thermal radio continuum knots (Turner & Ho 1983, 1985; Ulvestad & Antonucci 1997). This is exactly the orientation of sky-projected inner x_2 orbits in the barred potential model from Das et al. (2001), which was used to explain the H92α (Anantharamaiah & Goss 1996) and CO velocity fields. In the Das et al. (2001) model, the x_1 orbits, along the bar's major axis, form the larger NIR bar structure observed at PA=70° (Scoville et al. 1985; Arnaboldi et al. 1995; Peng et al. 1996; Iodice et al. 2014). We suggest that gas within the inner ring of x_2 orbits (along the NIR bar's minor axis) comprises a secondary nuclear bar that dominates ionized gas velocity structure in the radio core.

The candidate nuclear bar in NGC 253 is small. Its length $L_{\rm bar} \simeq 5'' \sim 85$ pc (Fig. 3.6) is only $\sim 1\%$ the size of the primary galactic bar in NGC 253, which has length $\sim$7 kpc (e.g. Scoville et al. 1985; Arnaboldi et al. 1995; Das et al. 2001). The Br α velocity profile indicates that is it rapidly rotating. The angular speed of the solid-body disk rotation is constant at $\Omega \simeq 590$ km s^{-1} kpc^{-1}. However, the gradient is steeper across the bar region, roughly -20 km s^{-1} arcsec^{-1} along the major axis within $R \lesssim 1\farcs0$, corresponding to an angular speed of $\Omega \sim 1200$ km s^{-1} kpc^{-1} (Fig. 3.7). In reality, the secondary bar rotation speed is somewhere in between, $\Omega_{s,\rm bar} \sim$ 600-1200 km s^{-1} kpc^{-1}. At $R \sim 50$ pc, the angular speed is $\gtrsim$10$\times$ faster than the primary bar's pattern speed of $\Omega_{p,\rm bar} \sim 50$ km s^{-1} kpc^{-1}. The result, albeit uncertain due to inevitable contributions of star cluster feedback to the velocity field, may be compared with the few existing measurements of inner bar rotation speed. Velocity maps produced from H α observations generally suggest secondary nuclear bars rotate $\gtrsim$3$\times$ faster than primary bars, reaching $\Omega \sim$ 100-500 km s^{-1} kpc^{-1} (e.g., Font et al. 2014). Although this is slow compared to the rotation implied by Br α for NGC 253, the discrepancy might arise because the H α emission traces an unobscured, extended gas component, while Br α emission can originate in obscured gas within a dusty bar.

The Br α velocity structure presented here is perhaps the strongest evidence yet for a nuclear bar in NGC 253. While tentative evidence for arcing contours has been found in RRL velocity fields, beam smearing and insufficient velocity resolution wash out the characteristic S-shaped bending (e.g., Anantharamaiah & Goss 1996; Das et al. 2001; Rodríguez-Rico et al. 2006). Using K band observations, Rosenberg et al. (2013) is the only other investigation to unambiguously resolve this structure, to the best of our knowledge. Interestingly, the S-shaped pattern at the radio core was found not only in their H_2 velocity field, but also in their *stellar* velocity field, strongly suggesting a gravitational origin. Conversely, the IRC's blue flow identified in our Br α velocity field is marginally seen in the H_2 field but has no counterpart in the stellar field, indicating gas dynamics shaped by star formation. We conclude that the radio core comprises gas and forming massive star clusters, orbiting within the strong gravitational potential of a $\lesssim$100 pc long nuclear bar. Constraining the properties of the bar, such as pattern speed and morphology, will require further observational study.

3.4.2 The Radio Core as the Galactic Center

The build-up of massive galactic bulges is largely driven by the formation and feedback of SMBHs, which are ubiquitous in massive galaxies. The symmetry of velocity contours near N1 favors the radio core, close to the brightest radio source TH2, as the location of the galaxy's kinematic center, rather than the IRC. The nature of TH2 is elusive. Its high brightness temperature (Turner & Ho 1985) and lack of associated mid-infrared continuum emission indicates a non-thermal emission mechanism, strongly disfavoring a H II region powered by super star clusters as its origin. Rather, the two leading explanations of TH2 are: an unusually bright supernova remnant (SNR), or an AGN (Turner & Ho 1985; Ulvestad & Antonucci 1997; Mohan et al. 2002). TH2 would be an unusually bright SNR, $\sim$100 times brighter than the Galaxy's brightest SNR, Cas A. Although there is no X-ray or IR counterpart source associated with TH2 (Fernández-Ontiveros et al. 2009; Müller-Sánchez et al. 2010), the presence of high-J CO, HCN, and dust emission suggests very high extinctions (Bolatto et al. 2013; Meier et al. 2015; Leroy et al. 2018). If TH2 is indeed a weak AGN, it would be a valuable nearby example of the starburst-AGN interaction.

The Br α velocity profile across TH2 yields mass estimates for a potential central SMBH in the radio core (Fig. 3.7). The minor-axis velocity gradient, roughly 50 km s^{-1} over 1.″5, suggests $M_{\rm dyn}^{\rm TH2} \sim 1.4x10^7$ M$_\odot$. A similar mass of $M_{\rm dyn}^{\rm TH2} \sim 7 \times 10^6$ M$_\odot$, based on a $\sim$110 km s^{-1} arcsec^{-1} gradient, is derived from the 0.″3-beam H92α map in Rodríguez-Rico et al. (2006). Given the measured central stellar velocity dispersion of NGC 253 ($\sigma = 109$ km s^{-1}; Oliva et al. 1995), the M-σ relation (Combes et al. 2019) predicts a SMBH of mass $M_{\rm bh} \sim 2 \times 10^7$ M$_\odot$, consistent with the estimate from Br α. The predicted sphere of influence has radius $r_h \sim GM_{\rm bh}/\sigma^2 \sim 8$ pc (Merritt 2004). The true velocity profile within the black hole's sphere of influence could be characterized by a significantly steeper gradient than is measured after being smeared out by the PSF of our observations. Extremely high extinction ($A_V \gtrsim 50$) in the center of NGC 253 (e.g., Leroy et al. 2018), should also significantly affect measurements of the velocity field of IR emission lines and thus estimates of dynamical mass.

High-resolution observations of gas in the centers of Seyfert galaxies suggest nuclear bars may be intimately tied to AGN phenomena, closely linked to the feeding and growth of SMBHs (e.g., Onishi et al. 2015; Barth et al. 2016; Davis et al. 2017, 2018). Given the bar-like kinematic substructure from our Br α measurements, the radio core of NGC 253 near TH2 is an excellent target for high-resolution IR-radio gas spectroscopy.

3.4.3 Starburst Feedback: Outflow from the IRC?

The starburst region of NGC 253 is driving a large-scale galactic wind, with an ionized outflow extending to $\sim$10 kpc (e.g., Strickland et al. 2002; Weaver et al. 2002; Westmoquette et al. 2011; Günthardt et al. 2019) along with molecular outflow from the central $\lesssim$ 1kpc (e.g., Sakamoto et al. 2006; Bolatto et al. 2013; Walter et al. 2017). The galactic wind should be powered by feedback from SSCs identified in the central starburst region (e.g., Turner & Ho 1985; Watson et al. 1996; Ulvestad & Antonucci 1997; Engelbracht et al. 1998; Forbes et al. 2000; Fernández-Ontiveros et al. 2009; Leroy et al. 2018). Characterization of outflow sources in NGC 253 is key for understanding the link between feedback from its starburst and its galactic wind.

Source S1 at the IRC exhibits the best evidence for outflow from its line profile and kinematic substructure. Assuming a mass of 10^6 $M_\odot$ (Leroy et al. 2018), the predicted escape velocity from the IRC is $v_{\rm esc}(R = 20\ {\rm pc}) \sim 20$ km s^{-1}. This is significantly smaller than the Br α line width of S1, σ_v ~50, 130 km s^{-1} for the primary and broad Br α components, respectively (Fig. 3.4). A maximum outflow velocity can be estimated with the velocity offset between the broad and primary components and the broad-component line width: $v_{\rm max} = \Delta v_{b,p} - {\rm FWHM_{broad}}/2$ (e.g., Veilleux et al. 2005; Arribas et al. 2014; Wood et al. 2015). Using average values for S1, $\Delta v_{b,p} \simeq -75$ km s^{-1} and ${\rm FWHM_{broad}} \simeq 300$ km s^{-1}, yields $v_{\rm max} \sim -225$ km s^{-1}, consistent with the Br γ outflow (Günthardt et al. 2019).

The potential outflow from the IRC is identified as a blue-shifted substructure in the Br α velocity field distinct from the nuclear bar pattern (Fig. 3.6), and as a negative velocity gradient and with curving red and blue wings in the major-axis PV image (Fig. 3.7). These structures suggest de-projected outflow speeds of $\gtrsim 100$ km s^{-1}, consistent with estimates from the line profile. We conclude that the Br α outflow from the IRC forms the base of the $\sim 100 - 300$ km s^{-1} Hα outflow (Westmoquette et al. 2011). Feedback from ~6-8 Myr-old SSC in the IRC appears presently capable of powering the kpc-scale galactic wind.

Like the Br α emission from S1, the emission from N1 has a broad blue component with line width exceeding the local escape velocity, indicating star formation feedback. However, the nuclear bar clearly dominates the velocity structure in the radio core. Compared with the IRC, the radio core exhibits a significantly larger Brackett line equivalent width, $W({\rm Br}\alpha) \sim 250$ Å (Sec. 3.3.1), and extinction ($A_V \sim 20 - 4000$; Günthardt et al. 2015; Leroy et al. 2018). This suggests a younger stellar population within the radio core formed in a more recent starburst episode. Feedback might be correspondingly weaker in this region if clusters have not yet evolved WR winds and SNe capable of driving significant mass loss. Alternatively, feedback might be suppressed as newly formed clusters separate from their natal gas within the bar potential due to tidal interactions. NGC 253 demonstrates the complex interplay between nuclear gravitational structure and star formation shaping the evolution of its central bulge.

3.5 Summary

Using NIRSPEC we have mapped the Br α line in the core of NGC 253, the site of a forming galactic center and an intense starburst that is powering a galactic wind on much larger scales. The constructed Br α cube, with $1''$ and 12 km s^{-1} resolutions, reveals four sources associated with complex gas motions influenced by nuclear galactic structure along with feedback from forming massive clusters. The two brightest sources, which we identify as N1 and S1, are associated with the bright radio and IR cores, respectively. Our main findings are as follows:

1. An underlying gradient of 10 km s^{-1} arcsec^{-1} across $> 10''$ along the major-axis is identified as the solid-body rotation curve of the inner disk. Residuals of a linear fit appear sinusoidal, with peaks of amplitude $\sim$15 km s^{-1} offset roughly $0\farcs6 \simeq 10$ projected-pc to the NE of each Br α sources. The residuals reflect non-circular motions; likely tracing structure of an inner nuclear bar/nuclear spiral.

2. S-shaped contours in the velocity field near N1 provide strong evidence for a nuclear gaseous bar centered on the radio core oriented at PA$\simeq$45°, aligned with predicted inner x_2 orbits of the larger galactic bar (Das et al. 2001; Paglione et al. 2004). The inner bar has radius $R \sim 40 - 50$ pc and is rotating rapidly, with $\Omega \gtrsim 600$ km s^{-1}. Intense star formation indicated by candidate SSCs and SNRs suggests that the nuclear bar can induce inflow into the galactic center and fuel star formation.

3. The galactic center, expected to host a SMBH, is near the radio peak TH2 in the radio nucleus rather than in the IRC. Based on the minor-axis gradient of 41 km s^{-1} arcsec^{-1} across TH2, we derive a mass of $\sim 10^7$ M$_\odot$ across $1\farcs5 \simeq 25$ pc, which can be compared with $M \sim 7 \times 10^6$ M$_\odot$derived previously from subarcsecond resolution RRL observations (Rodríguez-Rico et al. 2006). The sphere of influence of this black hole is $\lesssim 8$ pc in radius. The values are in rough agreement, given the lower spatial resolution of these data. The mass expected from the M-σ relation, $M \sim 10^7$ M$_\odot$, is consistent with the measurements.

4. The kinematics of source S1 indicate outflow driven by the IRC. Broad emission contributes half of the total line flux here, and has a line width greatly exceeding local escape velocities

(FWHM$\sim$300-350 km s^{-1}). The velocity field shows the outflow as a blue-shifted arc-like substructure at the IRC, distinct from the nuclear bar pattern. The estimated maximum outflow speed is $|v_{\rm max}| \sim 200 - 250$ km s^{-1}, consistent with the H α outflow (Westmoquette et al. 2011). The results provide a plausible link between feedback from star formation in the IRC and the observed large-scale galactic wind.

With a potential nuclear bar and SMBH, the radio core of NGC 253 is an ideal target for high-resolution IR-radio spectroscopic observations. Such measurements will provide insight into the nature of the nonthermal radio source, the presence and influence of a SMBH, and operation of feedback from individual SSCs in the forming galactic center.

Keck:II (NIRSPEC) IRAF, SAOImage DS9, Astropy (Astropy Collaboration et al. 2013)

CHAPTER 4

Observations of the Newborn Super Star Clusters in NGC 1569 with NIRSPEC

This chapter is from a paper currently in-preparation for submission on feedback across the embedded star-forming region of NGC 1569 near two candidate SSCs, the more massive of which is buried deep within a hot molecular core. This will be a priority target in future proposals to Keck, ALMA, and the VLA.

We report NIRSPEC (Keck II) observations of the Br α 4.05 μm recombination line across the two candidate embedded super star clusters (SSCs) in NGC 1569. Br α is detected as a strong peak from the luminous H II region powered by the less massive cluster ($\sim$100 O stars), extending towards the second more massive cluster ($\gtrsim$2000 O stars). A non-detection of Br α from the latter is consistent with its previously measured bright MIR continuum in the case that the source is extremely obscured and optically thick, potentially in the earliest phase of its formation–a hot molecular core hosting many deeply buried ultra- or hypercompact H II regions bound to newborn massive stars. Despite the thousands of O stars in the clusters, the Br α emission exhibits a symmetric Gaussian line profile with an extremely narrow linewidth of only $\Delta v = 45$ km s^{-1}, FWHM. Feedback from the embedded SSCs in NGC 1569 appears to be currently incapable of dispersing gas, making them excellent candidates to form multiple stellar populations.

4.1 Introduction

As the birth places for nearly all massive stars, giant star clusters fundamentally shape the dynamics and chemistry of their host galaxies. Galactic observations of ancient globular clusters (GCs) give

a direct view into the final, gravity-dominated phase of massive star cluster evolution. Interestingly, these investigations have revealed unexpected properties of GCs that are determined entirely within their earliest evolutionary phase. Of particular interest are how massive clusters survive the first ~ 5 Myrs of intense feedback from massive stellar evolution and remain bound for Gyrs, and how they form multiple stellar populations, found to be ubiquitous in GCs (e.g., Piotto et al. 2015). However the only young clusters with comparable mass to GCs exist within rare extragalactic starburst regions. These super star clusters (SSCs) host 10^5-$10^6 M_\odot$ in stars and gas and are $\lesssim$10 Myr old, representing perhaps the only directly observable analogs of proto-globular clusters (e.g., Turner 2009).

The youngest SSCs are still deeply embedded within their natal clouds of gas and dust and suffer large internal extinction, rendering them unobservable in optical-NIR wavelengths. However, these clusters ionize luminous compact H II regions that are detected as radio-IR "supernebulae" (e.g., Beck 2008). The dynamics of such supernebulae reflect the collective influence of rapidly evolving massive stars, providing unparalleled insight into the mechanisms of retention or expulsion, hence survivability, of massive clusters like GCs (Elmegreen 2018; Gray et al. 2019). Requiring high spatial and spectral resolution in the IR/radio, direct measurements of supernebula kinematics have, until recently, been largely infeasible.

Observations of SSCs made within the last few years provide evidence for a fundamental difference in how feedback operates in the densest, most-massive star clusters. Of the most illuminating sources have been the supernebula in dwarf starburst galaxy NGC 5253, which exhibits a recombination linewidth of merely $\Delta v \sim 75$ km s^{-1} despite being powered by a $M \sim 2.5 \times 10^5 M_\odot$ cluster with $\sim$2000 O stars within its $\sim$3 pc core(Turner et al. 2000; Meier et al. 2002; Turner et al. 2003; Turner & Beck 2004; Calzetti et al. 2015; Smith et al. 2016; Consiglio et al. 2017; Turner et al. 2017; Cohen et al. 2018). Simulations have found that the most highly concentrated forming SSCs host ionized stellar wind regions that can stall in their expansion due to critical radiative cooling, preventing a coherent cluster wind and allowing the cluster to retain enriched fuel for ongoing star formation (Silich & Tenorio-Tagle 2018, 2017; Gray et al. 2019). Finding and studying more of SSCs like the NGC 5253 supernebula is critical to solving the unanswered questions of GC formation and galaxy evolution.

Perhaps the next best candidate of a proto-globular cluster after NGC 5253 is found within dwarf starburst NGC 1569, located at a distance of $D = 3.4$ Mpc (Grocholski et al. 2012). Despite being known for its two optically bright SSCs, A and B (e.g., Hunter et al. 2000), NGC 1569's most active star formation is concentrated to an obscured region characterized by high extinction (Pasquali et al. 2011). Intense thermal radio continuum coinciding with bright He I and Pa β emission here indicates the presence of H II regions excited by forming massive star clusters (Greve et al. 2002; Clark et al. 2013). The brightest H II region, identified as H II 2 in Waller (1991), is located near a group of CO clouds at the end of a Hα filament extending $\sim$2 kpc (Taylor et al. 1999). H I along this filament exhibits redshifted non-circular motion (Johnson et al. 2012), indicating a potential inflow into the embedded star-forming region. This could be an example of filament-fed star formation, much like the case suggested for NGC 5253(Turner et al. 2015; Consiglio et al. 2017).

Two candidate embedded forming massive clusters in NGC 1569, identified with [S IV] imaging in Tokura et al. (2006) as MIR1 and MIR2, may be responsible for ionizing H II 2 and its surrounding emission. The brighter source MIR1 has an ionizing photon luminosity consistent with $\gtrsim$100 O7 stars (revised for $D = 3.4$ Mpc). Interestingly MIR2 exhibits only a weak counterpart in the radio continuum but comparable MIR continuum emission originating from hot dust. The IR luminosity of MIR2 is consistent with $\sim$2000 O7 stars. Tokura et al. (2006) suggests MIR2 is a SSC in the earliest phases of formation, where extinction is so high that the nebula is optically thick even to free-free emission but has a bright dust emission continuum from the hot molecular core. The relation between MIR1 and MIR2, along with their gas kinematics, is unclear.

In this paper we present the Br α emission line spectrum across embedded SSC candidates MIR1 and MIR2 and the brightest H II region in NGC 1569, obtained with the NIRSPEC echelle spectrograph on Keck. At 4 μm, the Br α line is less effected by extinction than H α or Br γ. For the first time, the spectra reveal the dynamical nature of the embedded SSCs at a $\sim$20 km s^{-1} scale. We adopt a distance of $D = 3.4$ Mpc for NGC 1569 (Grocholski et al. 2012), which corresponds to a scale of 1$''$=16 pc.

4.2 Observations

We observed the embedded star-forming region in NGC 1569 with NIRSPEC on Keck II (McLean et al. 1998) during the first half-night on Dec 7, 2017. Two high-resolution (echelle) spectra, each with 240s integration, were acquired in the KL band through a $0\farcs432\times24''$ slit positioned on the galaxy's thermal radio continuum peak(Greve et al. 2002) and candidate embedded SSCs MIR1 and MIR2(Tokura et al. 2006), as shown in Fig. 4.1. The echelle and cross-disperser angles were set to 64.42° and 34.3°, respectively, to observe the Br α line in the 19th echelle order. The resulting wavelength coverage of this order was 4.032-4.085 μm. calibration star, HD12365, was observed with an ABBA nod sequence prior to observations of NGC 1569.

Each slit position yielded a 2D echelle spectrum which we rectified and reduced. Reduction involved the use of flat-field and ThArXeNe arc-lamp spectra acquired at the beginning of the night, the spectrum of a calibration star, HD12365, which observed with an ABBA nod sequence prior to NGC 1569, and a raw sky spectrum taken after NGC 1569 exposures at an offset of $\sim50''$. After first being cleaned of cosmic rays and bad pixels, raw science spectra were sky-subtracted (or $A - B$ subtracted in the case of HD12365) and divided by a median-normalized flat-field image. The spectra were then rectified – mapped from the curved echelle order onto a grid with orthogonal spatial and dispersion axes, using transformations generated with the `SPATMAP` and `SPECMAP` routines from the `REDSPEC` reduction code[1]. The wavelength calibration was determined as part of the `SPECMAP` procedure by identifying arc-lamp lines and fitting their positions with a 3rd-order polynomial.

The reduced echelle spectra have spatial information along the vertical axis and spectral information along the horizontal axis, with a pixels size of $0\farcs152$ by 5.44×10^{-5} μm. The instrumental spectral resolution at 4.051 μm is 12 km s^{-1}. The photometric calibration was estimated with the spectrum of HD12365 by summing the star's spectral trace and adopting a 65% flux loss by the $0\farcs5$ slit, allowing us to convert measured flux in counts s^{-1} to physical units. Wavelengths and velocities quoted in this paper have been converted to the heliocentric frame.

[1] `https://www2.keck.hawaii.edu/inst/nirspec/redspec.html`

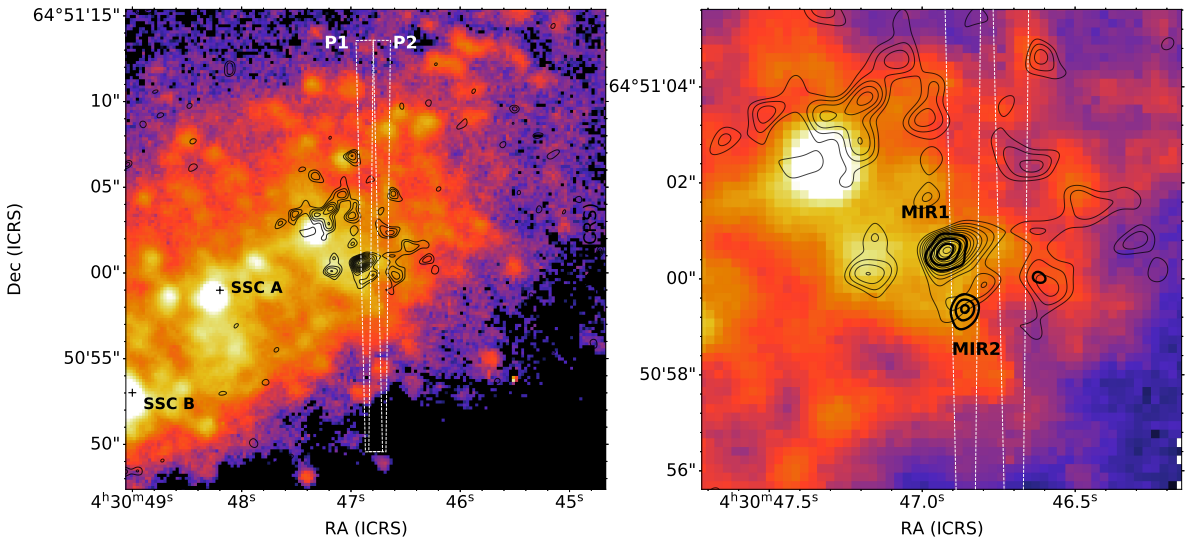

Figure 4.1: NIRSPEC observations of the embedded star-forming region in NGC 1569. Left) Positions of the $0\farcs432 \times 24''$ slits (white boxes) over the combined SCAM image of the KL-band continuum (colorscale). Slits were centered near the bright thermal radio continuum source (contours; Greve et al. 2002), coincident with [S IV] 10 μm sources MIR1 and MIR2 from Tokura et al. (2006). Optical SSCs A and B are shown for reference. *Right*) Zoom-in of target region, showing the relation between 10μm continuum (thick contours; Tokura et al. 2006), radio continuum (thin contours), and KL-band (colorscale). MIR1 and MIR2 stand out as the birightest MIR sources in the region by far. The seeing measured in the SCAM imaging is $0\farcs9 \simeq 13$ pc

4.3 Results

4.3.1 Spatial Morphology and Relation to MIR Sources

Imaging of the KL-band continuum was obtained with the NIRSPEC Slit-Viewing Camera (SCAM) during spectral exposures and used to determine accurate positioning of the slits on the sky (Fig. 4.2). To perform astrometric calibration, we first combined sky-subtracted SCAM images for each of the two on-target positions, and measured the pixel positions of bright IR sources detected within each image. The IR sources were then matched to sources with well-established ICRS coordinates from the Gaia DR2 catalog (Gaia Collaboration et al. 2016, 2018). Residuals (RMS) of the best-fit astrometric solutions are $\sim 0\farcs1$. The registered images were combined into the slit-free image shown in Figure 4.1.

The SCAM imaging indicates a seeing FWHM of $0\farcs9$, which should be capable of resolving separate contiuum emission peaks, however no KL-band emission source is clearly linked to MIR2 despite bright MIR emission (Fig. 4.1). Weak radio continuum is coincident with MIR2 but may

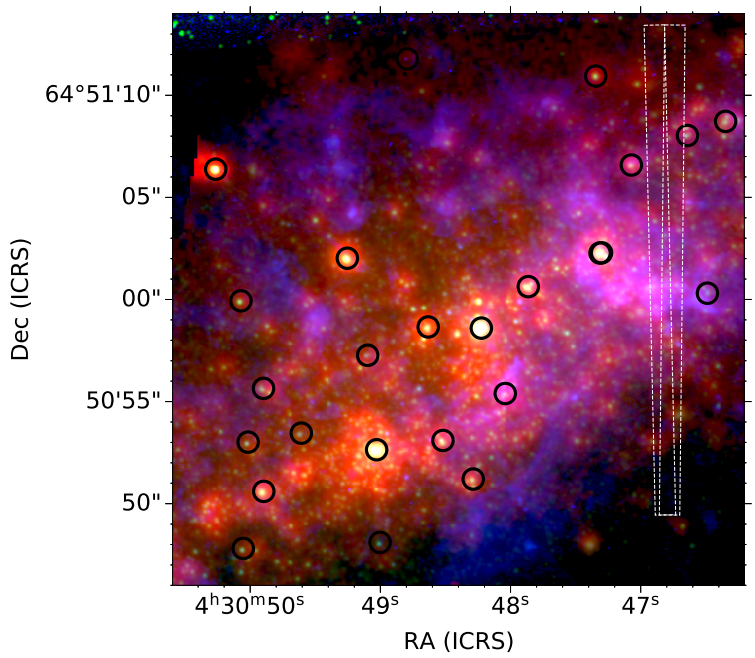

Figure 4.2: Registration of the slits (white boxes) with GAIA sources (black circles). The background three-color image shows archival HST F656N (blue) and F814W (green) along with the KL-band (red). The astrometric solution is accurate to $\sim 0\farcs1$

represent ionized gas associated with the extended H II at MIR1. MIR1 does coincide with a local peak KL-band continuum peak, however is still faint compared to the surrounding continuum, especially that directly to the NE near cluster #10. With a lack of strong emission even in the 2-4μ continuum, both sources are likely to be deeply embedded clusters, with MIR2 representing a potential example of an extremely obscured forming cluster.

Fig. 4.3 shows cutouts of the Br α emission in the two 2D spectra along with 1D spatial profiles extracted by collapsing the cutouts along the spectral axis. A dominant, intense peak is detected at the location of MIR1, with a shoulder of emission extending to its south in the direction of MIR2. The second brightest peak is detected about $3''$ north and is most pronounced in the second slit position. This source is mysterious, but is likely associated with the radio continuum detected in its vicinity (Fig. 4.1). We hereafter refer to the southern bright source, including the both the narrow peak near MIR1 and extended southern shoulder, as Br-S and the northern faint source as Br-N. The two peaks were fit with Gaussian profiles to derive their sizes and separations (Table 4.1). No continuum is detected across the slit. We note that Br-N has no relation to MIR2 nor MIR1, but could be linked to the radio emission near cluster #10 (Westmoquette et al. 2007).

Br-S is spatially extended, with a best-fit size $\Delta\theta = 2\farcs2$ of a single-component Gaussian spatial profile. A narrow bright peak is detected at the location of MIR1, and thus likely traces emission from the core of its H II region (HII 2; Waller 1991). With $0\farcs9$ seeing we would expect to separate Br α emission from MIR2, which is separated from MIR1 by $1\farcs5$. However, no clear secondary peak is detected– rather, the Br α exhibits a southern shoulder of emission extending $\simeq 0\farcs5$ past the expected location of MIR2 (Fig. 4.3). A two-component Gaussian fitted to the intensity profile of Br-S, shown as the dashed curves Fig. 4.2, yields an unresolved narrow peak at the origin and an extended ($\Delta\theta_{FWHM} \simeq 2\farcs5$) peak offset from the narrow peak by $-0\farcs6$. We suggest that Br-S comprises a two-component structure, with a compact bright core and an ionized extended envelope, both of which are powered by the embedded cluster MIR1. Additional weaker, tentative emission peaks exhibited by the spatial profile on either side of Br-S in its wings. Moreover, Br α emission is tentatively detected extending up to $\sim 9''$ north of Br-S. These smaller peaks could trace density enhancements such as a gas filament intersecting the slit or possibly a shell of ionized gas

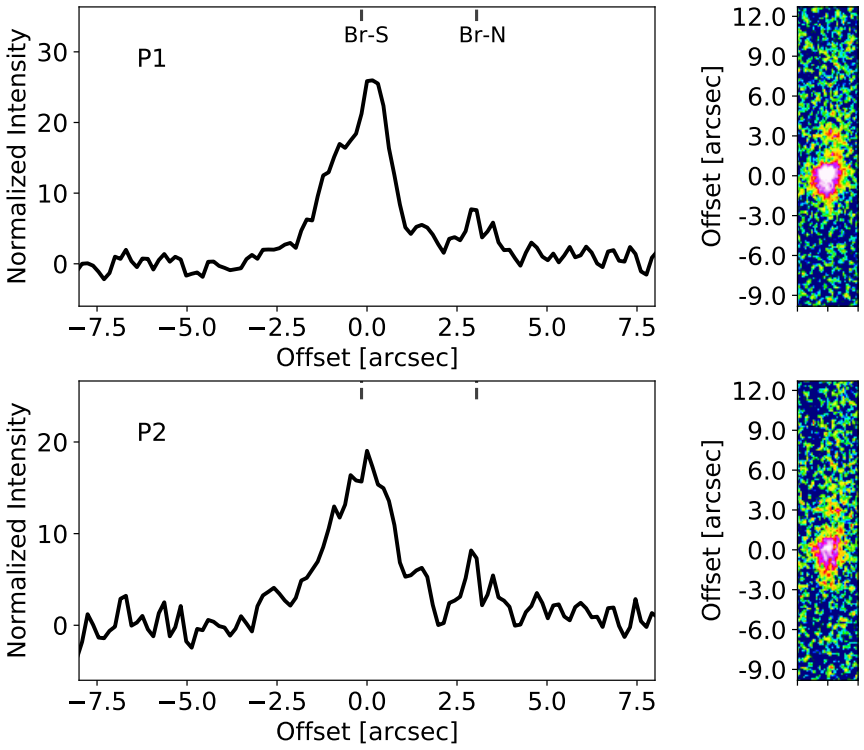

Figure 4.3: Spatial profile (intensity along the slit) of Br α for the two slit positions outlined in Fig. 4.1. The profile was extracted by averaging columns in the spectrum cutout displayed on the right panel. The peaks at offset $0''$ and $3''$ correspond to sources Br-S and Br-N identified in the text.

like those observed around many H II regions (Sewilo et al. 2004b).

The non-detection of MIR2 is consistent with the source being very heavily embedded, as suggested in Tokura et al. (2006). These authors detect MIR2 as weak unresolved [S IV] line emission with bright extended continuum ($\sim 0\farcs6$), suggesting a molecular core that is optically thick to the H II regions buried deep within. Using the revised distance (3.4 Mpc), the IR luminosities reported in Tokura et al. (2006) are consistent with ionization by $\sim$100 O7 and $\sim$2000 O7 stars for MIR1 and MIR2, respectively. Thus, the observed Br α is most likely tracing the smaller less obscured cluster MIR1, while proto-SSC MIR2 has not yet hatched from its gigantic egg. The shoulder extending from MIR1 to MIR2, however, presents a potential physical link between the two sources. That the shoulder is much less pronounced in the second position, which was offset from MIR2, strengthen this potential link. These sources could represent sub-clusters that will eventually merge into a giant cluster, similar to what may be occuring in NGC 5253(Smith et al. 2020).

4.3.2 Kinematics

Kinematic properties of the bright H II region in NGC 1569 were measured from spectra extracted for Br-S and Br-N with apertures of radius $r = 7$pix$\simeq 1\farcs1$ to include virtually all of the source flux (Fig. 4.4). The Br α lines from both sources appear remarkably symmetric; $\chi^2_\nu = 1.6$ and 1.2 for a best-fit Gaussian profile to the spectrum of Br-S and Br-N, respectively. A two-component Gaussian profile provides a better model for Br-S, however, to account for its broad wings ($\chi^2_\nu = 1.3$, Fig. 4.3). The measured properties of the Br α line, including both the single-component and two-component fit of Br-S, are reported in Table 4.1.

The most intriguing feature of the Br α line is the narrow linewidth of Br-S, only ΔV_{FHWM} $\sim$45 km s^{-1} or less across the entire H II complex. Atomic and molecular gas reach line widths of ΔV_{FWHM} $\sim$25-40 km s^{-1} and $\gtrsim$10 km s^{-1} for H I and CO gas, respectively, indicate a highly disturbed ISM but are not localized to H II 2 (Johnson et al. 2012; Taylor et al. 1999). The Br α observations in this work represents the first dynamical measurements of NGC 1569's giant H II region, H II 2, powered by embedded cluster MIR1. Westmoquette et al. (2007) report a line width of ~ 35 km s^{-1} for optical gas near cluster #10, possibly associated with source Br-N but unrelated

to H II 2 (their claimed association of cluster #10 with H II 2 is attributed a systematic error in the astrometry).

Source Br-S exhibits two velocity components: a narrow core with line width (FWHM) $\Delta V_n = 32 \pm 3$ km s^{-1} and a broader pedestal with $\Delta V_b = 74 \pm 12$. Each component contributes $\sim$50% of the total line flux. A narrow+broad Br α line profile is common for embedded SSCs, however such massive clusters are observed to have broad-component line widths of $\Delta V_b \sim 250 - 350$ km s^{-1}(Henry et al. 2007; Beck 2008; Cohen et al. 2018), much larger than that of Br-S. For comparison, the embedded supernebula in NGC 5253 exhibits a narrow component line width $\Delta V_n \sim 75$ km s^{-1} (Cohen et al. 2018). The line profile of Br-S is perhaps most comparable to Galactic hypercompact H II regions, which have typical linewidths of 30-50 km s^{-1}(e.g., Hoare et al. 2007; Sewilo et al. 2004a).

The heliocentric centroid velocity of Br-S is $V_{\rm helio} = -85$ km s^{-1}, consistent with the stellar and H I gas systemic velocities (Johnson et al. 2012). The velocity centroid shifts towards higher velocity to the north of Br-S, measured at $V_{\rm helio} = -72$ km s^{-1} for Br-N, suggesting a gradient of roughly $+5$ km s^{-1} arcsec^{-1} or ~ 0.3 km s^{-1} pc^{-1} from south to north across NGC 1569's embedded star-forming region.

The spatial dependence of centroid velocity and line width along the north-south slit axis, shown in Fig. 4.5, is investigated further by extracting 1D spectra from non-overlapping 4 pixel-wide ($0\farcs6$) apertures along the spatial axis of the 2D spectrum, and fitting the line with single-component Gaussian profiles. A change in the line shape and peak position is visible by eye in the observed spectra in Fig. 4.4, left. Best-fit $V_{\rm helio}$ and ΔV are shown as a function of offset in Fig. 4.4, right, revealing this pattern in more detail. A positive velocity gradient of $\simeq 2$ km s^{-1} arcsec^{-1} extends to the south of the peak of Br-S, along its shoulder. The slight redshift south along the shoulder corresponds to a sharp decrease in line width from ~ 45 km s^{-1} at the peak to ~ 30 km s^{-1} at $2''$.

A much steeper positive gradient of ~ 10 km s^{-1} arcsec^{-1} occurs to the north of Br-S, reaching a maximum $V_{helio} \simeq -65$ km s^{-1} at an offset of just over $2''$, and then reversing sign and decreasing until the location of Br-N (offset=$3''$), where $V_{\rm helio} \simeq -75$ km s^{-1}. The minimum velocity centroid

of the arc seemingly corresponds to a local maximum in the line width of roughly 45 km s^{-1}.

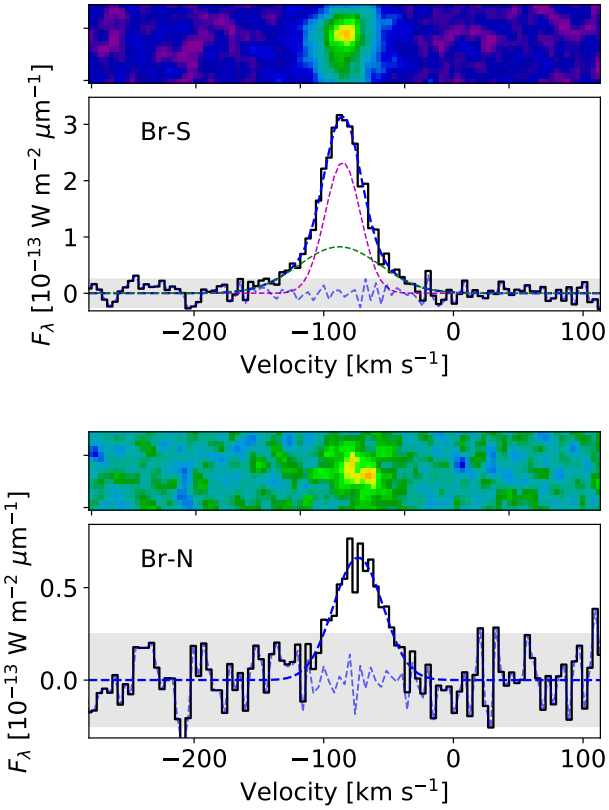

Figure 4.4: Br α spectrum of sources Br-S and Br-N, extracted by summing rows in the 2D spectra (colorscale) within a 14 pixel-wide box centered on each peak. The shaded grey band indicates 2σ; Br-S and Br-N are detected with peak S/N of $\sim$25 and 5, respectively. The dark and light blue dashed curves show the best-fit profile and residuals. Two Gaussian components (magenta and green dashed curves), while Br-N is fit with a single Gaussian profile.

4.4 Discussion: Properties of the Embedded Clusters

The recombination line flux of the H II region complex is dominated the bright, extended ($\sim 2\farcs2 \simeq 36$ pc) source Br-S. The spatial profile (Fig. 4.2) strongly suggests that Br-S comprises emission powered by candidate embedded cluster MIR1 and is distributed as an unresolved core ($\lesssim 1''$) along with an extended southern shoulder. This suggests a link to its more massive, much more heavily embedded neighbor MIR2 $1\farcs5 \sim 25$ pc away.

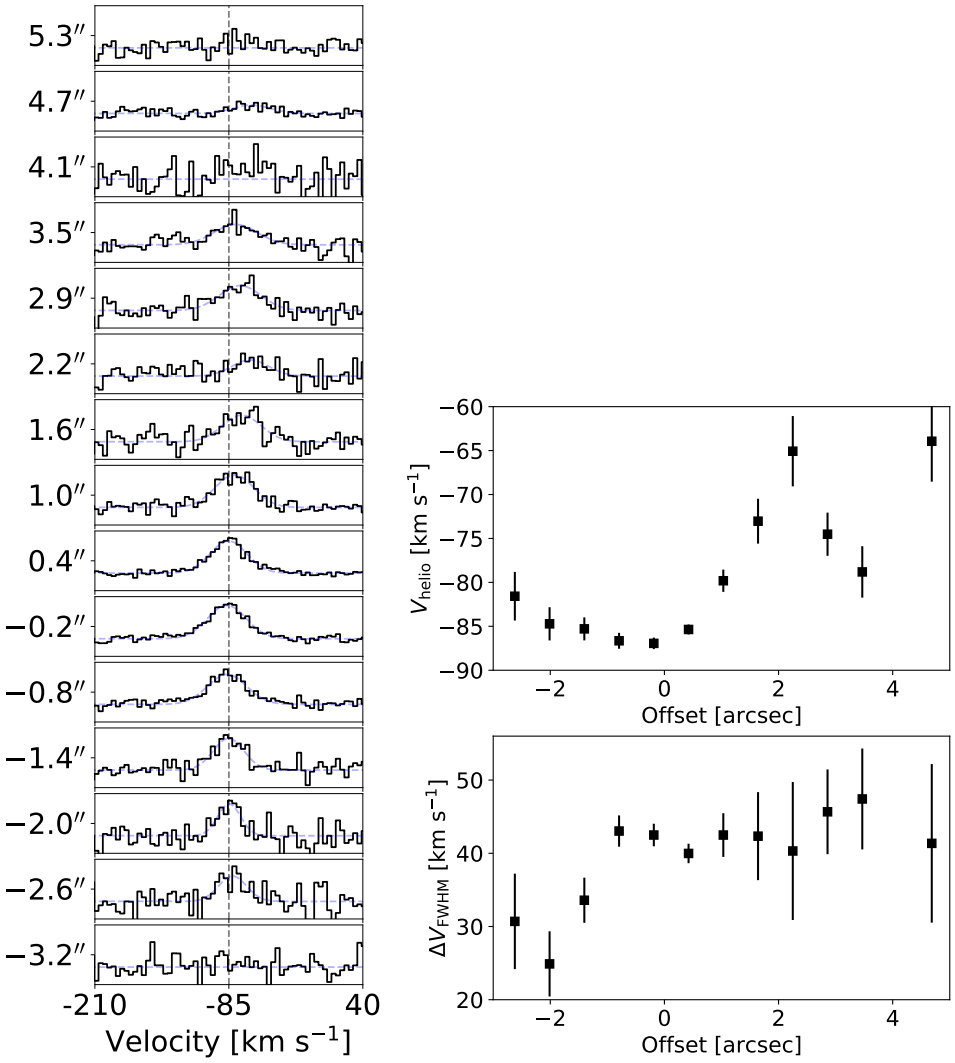

Figure 4.5: The Br α spectrum as a function of position along the slit (north-south). Left) Observed spectrum extracted every $0\farcs6 = 4$ pix along the slit axis (black line) and fit with a Gaussian profile (blue-dashed line) to measure velocity centroid and line width. The vertical black dashed line shows the systemic velocity, $V_{sys} = -85$ km s^{-1}. Right) Centroid velocity (top) and line width (bottom) versus position along the slit (offset increases north).

4.4.1 Ionization of the Giant H II Region

We can estimate the ionizing photon rate of Br-S from the Br α flux as outlined in Ho et al. (1990). Without correcting for extinction the flux is $F = (2.0 \pm 0.4) \times 10^{-16}$ W m^{-2} (Table 4.1). Assuming a temperature $T_e = 1.5 \times 10^4$, we find $N_{\rm LyC} \sim 8 \times 10^{51}$ s^{-1}, equivalent to the ionizing radiation of roughly 800 O7 stars. We derive a comparable value of $N_{\rm LyC} \sim 7 \times 10^{51}$ s^{-1} using the 3.6cm continuum flux of MIR1, $S_{3.6{\rm cm}} = 9.2$ mJy (N1569-13; Chomiuk & Wilcots 2009). The visual reddening in the NW star-forming region is $E(B-V) \simeq 0.8$, corresponding to extinction at 4.05μm

Table 4.1: Properties of the two Br α sources identified in Fig. 4.2 and 4.3.

Source	Offset[a]	$\Delta\theta_{FWHM}$[b]	$F_{\rm tot}[10^{-17}$ W m$^{-2}]$[c]	$V_{\rm hel}$[km s^{-1}][d]	ΔV[km s^{-1}][e]
Br-S	0.0	2.2 ± 0.2	20 ± 4	-85 ± 1	42 ± 2
Br-N	3.1	1.2 ± 0.3	4 ± 1	-73 ± 2	45 ± 5
$F_n/F_{\rm tot}$[f]	$V_{\rm n}$[km s^{-1}][g]	$\Delta V_{\rm n}$[km s^{-1}][h]	$F_b/F_{\rm tot}$[i]	$V_{\rm b}$[km s^{-1}][j]	$\Delta V_{\rm b}$[km s^{-1}][k]
0.55	-85 ± 1	32 ± 3	0.45	-88 ± 3	74 ± 12
.....	.....	.....	.....	.....	.....

[a] Spatial offset (along slit, north is positive) from the brightest source, Br-S (Fig. 4.3). [b] Angular size of source (FWHM) from the best-fit single Gaussian profile to the 1D spatial profile (Fig. 4.2). [c] Br α line flux derived from the best-fit model of the 1D spectra (Fig. 4.3) extracted within a $2\farcs2$ aperture; for Br-S, the total flux of both fit components. [d] Heliocentric centroid velocity from a single-component fit of the Br α emission (Fig. 4.3). [e] Br α velocity line width (FWHM) of the single-component fit to the spectrum. [f] Fraction of total flux in the narrow component from the best-fit two-component spectrum (Fig. 4.3). [g] Heliocentric centroid velocity of the narrow fit component. [h] Br α velocity line width (FWHM) of the narrow fit component (Fig. 4.3). [i] Fraction of total flux in the broad component from the best-fit two-component spectrum (Fig. 4.3). [j] Heliocentric centroid velocity of the broad fit component. [k] Br α velocity line width (FWHM) of the broad fit component.

of $A_{\rm Br\alpha} = 0.2$ (Rieke & Lebofsky 1985), where we have adopted a $R_V = 4.05$ (Calzetti 1997). Correcting for this extinction yields an ionizing photon rate of $N_{\rm LyC} \sim 10^{52}$ s^{-1} or around $\gtrsim$1000 O7 stars, corresponding to a stellar luminosity of $L_{\rm OB} \sim 5 \times 10^8 {\rm L}_\odot$. This extinction corrected value still accounts for less than half of the the MIR-derived luminosities of MIR1+MIR2 (Tokura et al. 2006), suggesting that most of the ionized gas in this region is indeed entirely obscured and that MIR1 contributes the bulk of Br α emission we detect as Br-S.

Northern source Br-N has no clear counterpart identified in the literature but is apparent in the radio continuum. The closest published objects are radio sources M-a from Greve et al. (2002) and NGC1569-15 from Chomiuk & Wilcots (2009), offset $\sim 2''$ to the NW and NE, respectively. With an observed (uncorrected) flux of $F_{\rm Br\alpha} = (4 \pm 1) \times 10^{-17}$ W m^{-2}, the ionizing photon rate for a temperature $T_e = 1.5 \times 10^4$ is $N_{\rm LyC} \sim 10^{51}$ s^{-1}.

4.4.2 Dynamical Constraints

In the last few years, theoretical work on forming massive clusters have found that a cluster's ability not only to survive feedback from its first generation of stars but also to retain enough gas to form a second stellar generation is closely linked to its initial mass concentration M/R (e.g., Krause et al. 2016; Silich & Tenorio-Tagle 2018; Elmegreen 2018). Using the Br α line width we

can estimate the concentration of the clusters powering Br-S, more likely to be a lower limit due to the high obscuration of the more massive cluster MIR2. Observed IR hydrogen recombination line widths result from the convolution of thermal Doppler broadening $\Delta V_{thermal} = \sqrt{k_B T_e / m_H}$ and non-thermal turbulent broadening due to gravity or feedback. Assuming $T_e = 1.5 \times 10^4$, the single-component line width $\Delta V_{\rm obs} = 42 \pm 2$ km s^{-1} corresponds to a turbulent width $\Delta V_{\rm turb} = 31 \pm 3$, where we have also subtracted the instrumental line width in quadrature. If the turbulent width is solely due to gravity we can estimate the compactness using the virial theorem (MacLaren et al. 1988): $M/R = 190(\Delta V_{\rm turb})^2 \sim 2 \times 10^5\ M_\odot$ pc^{-1}, assuming a $1/r$ density profile. These values are consistent with kinematic measurements of of SSCs in NGC 5253, II Zw 40, He 2-10, the Antennae (e.g., Henry et al. 2007; Beck et al. 2013, 2015; Turner et al. 2003; Cohen et al. 2018). We note that if we instead use the narrow, broad component line widths of the two-component fit (Fig. 4.3), we estimate $M/R \sim 10^5 M_\odot$ pc^{-1} and $M/R \sim 10^6 M_\odot$ pc^{-1}.

The mass concentration and observed size ($R_{cl} \sim 1'' = 16$ pc) imply a cluster mass of $M_{cl} \sim 3 \times 10^6$ M$_\odot$. A more realistic estimate is $M_{cl} \sim 2 \times 10^5$ M$_\odot$, using $R_{cl} = 1$ pc– a size that is typical of embedded SSCs and consistent with the compact nature of the core of Br-S (Sec. 4.3.1). This is an upper limit to the mass of MIR1, as the turbulent line width may include contributions from ionized stellar winds and other non-gravitational effects. In this case, a more appropriate mass might be that derived from the narrow component line width, $M_{cl} \sim 4 \times 10^4$ M$_\odot$ (assuming $R = 1$ pc). However, the symmetry of the line strongly suggests that gravitational motions comprise the dominant contribution to the non-thermal line width. Indeed, the extinction-corrected ionizing photon luminosity derived above results in a mass of $M_{cl} \sim 3 \times 10^5$ M$_\odot$.

4.5 Summary

We have observed the Br α emission line across the embedded star-forming region in NGC 1569, at the location of the galaxy's brightest H II region and two candidate SSCs. We find:

1. The recombination line flux of the H II region complex is dominated by a bright source with size $\Delta\theta \simeq 2\farcs2 = 35$ pc, which we label Br-S. The spatial profile strongly suggests that Br-S actually comprises a compact, unresolved core and an extended envelope to its south.

2. The Br α line width is extremely symmetric and narrow, only 42 km s^{-1} FWHM, comparable to Galactic hyper-compact H II regions. Both the flux and line width implies a mass of $\sim 10^5$ within a $R_{cl} \sim 1$ pc cluster. At the very least, the gas is heavily influenced by gravity and may be bound.

3. The Br α flux predicted by MIR measurements (Tokura et al. 2006) is much larger than the measured flux of Br-S, indicating the presence of an even more massive embedded SSC that is optically thick to the radiation of its H II regions.

Overall, the Br α results indicate H II 2 is ionized by a $\sim 10^5$ M$_\odot$ embedded cluster, MIR1, which exhibits no clear evidence for explosive feedback. Furthermore, the gas ionized by MIR1 is potentially physically linked with a second, more massive proto-cluster (MIR2) ~ 25 pc away, whose deeply embedded H II regions are entirely obscured. These clusters are excellent candidates to form multiple populations, and possibly even merge to become a giant globular-cluster like object.

Keck: II(NIRSPEC)

CHAPTER 5

Buried Treasure in the Hidden Galaxy: Br α Spectroscopy of Maffei 2

This chapter is from a paper in-preparation for submission on the ionized gas velocity structure in the nuclear starburst of the "hidden galaxy" Maffei 2. Prior to this study kinematics have only been measured for molecular gas, which shows evidence of a molecular outflow from the starburst along with a central nuclear bar.

We present measurements of the kinematic structure of ionized gas across the central starburst within the "hidden" galaxy Maffei 2, an obscured barred spiral and one of the closest starbursts. To investigate the feeding and feedback of its nuclear starburst, we measured the velocity structure from $\sim$20 km s^{-1} resolution spectroscopy of the Br α emission line obtained with NIRSPEC. Br α emission in the starburst resolves into a handful of compact sources, likely H II regions powered by forming SSCs, concentrated at the ends of a r $\sim$100 pc nuclear bar. We find clear evidence for gas flow along the nuclear bar. A central redshifted source with bright line and continuum indicates a candidate forming nuclear star cluster and site of a SMBH. More work should reveal the complex dynamical nature in the starburst and its context within galaxy growth.

5.1 Introduction

Nonaxisymmetric structures such as bars play a vital role in the formation and evolution of galaxies. Bars are often found in hosts with intense nuclear star formation or starbursts, suggesting they can promote gas inflow into a galactic nucleus. The interplay between such bar-induced gas flow and the gas motions driven by feedback from star formation and AGN determines the central mass

evolution of spiral galaxies (e.g., Kormendy & Kennicutt 2004).

Observations of barred galaxies commonly find super star clusters (SSCs) forming at the ends of nuclear bars or rings (e.g., Athanassoula 1984; Buta & Combes 1996; Buta & McCall 1999; Böker et al. 2008; Comerón et al. 2010). As forming SSCs convert inflowing gas into dense collections of massive stars, they can the drive multi-phase, large-scale galactic winds observed nearly ubiquitously in starburst galaxies (e.g., Heckman 2001). Such feedback is intimately tied to the growth of a central SMBH, and AGN feedback can in turn regulate star formation to determine the mass evolution of galactic bulges (e.g., Renaud et al. 2013; Athanassoula et al. 2013; Carles et al. 2016; Li et al. 2015; Robichaud et al. 2017; Seo et al. 2019). High-resolution observations of the central $\lesssim 1$ kpc starbursts in disk galaxies are key to completing this puzzle.

Maffei 2 is one of the closest starburst systems ($D = 3.5$ Mpc; Table 5.1), but is entirely obscured ($A_V \gtrsim 5$; Maffei 1968). Aptly called the "hidden galaxy", Maffei 2 is a strongly barred spiral galaxy with evidence for a recent interaction that could explain the bright nuclear starburst (Hurt et al. 1993, 1996; Buta & McCall 1999). The central $\lesssim 0\farcs5$ hosts intense knots of star formation, likely forming SSCs, identified in the radio continuum and in CO (Turner & Ho 1994; Tsai et al. 2006; Meier & Turner 2012). The molecular gas kinematics and chemistry were investigated in Meier & Turner (2012), hereafter MT12. These authors find conclusive evidence for a nuclear bar of radius $r \sim 110$ driving a 0.7 $M_\odot$ yr^{-1} central inflow that can easily fuel the star formation (0.3 $M_\odot$ yr^{-1}). In addition to gas flow tracing the mass structure, MT12 identify a potential signature of molecular gas entrained in a starburst-driven outflow, appearing in their maps as lobes of C_2H along the minor axis. A full picture of the Maffei 2 starburst cannot be established without measurements of the ionized gas kinematics.

In this project, the goal was to determine kinematic structure of ionized gas in the Maffei 2 starburst for the first time. We used NIRSPEC to observe the Br α emission line, which is bright and less affected by extinction than Br γ. By obtaining slit-spectra across the nucleus and astrometrically registering the slits to GAIA sources, we were able to construct a Br α cube of the central $\sim 20''$ region along the nuclear bar and line of compact radio sources.

Table 5.1: Properties of Maffei 2 and its nuclear starburst.

$(\alpha, \delta)_{\rm J2000}$	$2^{\rm h}41^{\rm m}55.017^{\rm s}$, $+59°36'15\farcs41$
Hubble class	SBb(s) pec[(1)]
Distance; scale	3.5 Mpc; $1'' = 17$ pc[(2)]
Major axis PA	206°[(1)]
Inclination angle	67°[(1)]
Bar PA	29°[(1)]
V_{sys} (helio)	-30 km s^{-1}[(3)]
$M_{\rm H_2}(r \lesssim 300$ pc)	2×10^7M$_\odot$[(3)]
$M_{dyn}(r \lesssim 300$ pc)	7×10^8M$_\odot$[(3)]
Nuclear $N_{\rm LyC}$	2.6×10^{52} s^{-1}[(3)]
Nuclear SFR	0.26 M$_\odot$ yr^{-1}[(3)]
Nuc bar radius	110 pc[(3)]
Nuc bar pattern speed	135 km s^{-1} kpc^{-1} [(3)]
Nuc bar inflow rate	$\lesssim 0.7$ M$_\odot$yr^{-1}[(3)]

[(1)] Hurt et al. (1996). [(2)] Wu et al. (2014).
[(3)] Meier et al. (2008), Meier & Turner (2012).

5.2 Observations

We observed the $\lesssim 30'' = 500$ pc nuclear starburst in Maffei 2 with NIRSPEC on Dec 7, 2017 (Fig. 5.1). High-resolution echelle spectra in the KL-band were acquired through a $0\farcs432 \times 24''$ slit initially oriented roughly N-S (PA=358°) and positioned along the bright compact radio continuum sources, potential SSCs (Tsai et al. 2006). We acquired 8 120s exposures as the slit PA drifted due to the Earth's rotation, resulting in a final PA of 342°. Sky spectra were acquired by offsetting away from Maffei 2 after the 4th science exposure. Calibration star HD12365 was observed at a similar airmass prior to the Maffei 2 observations. Images of the slit on the sky in the K band were simultaneously acquired using the NIRSPEC Slit-Viewing Camera (SCAM). The echelle and cross-disperser angles were set to 64.42° and 34.3° to observe Br α (4.052 μm) in the 19th order. Average seeing was $0\farcs8 \simeq 14$ pc, varying between $0\farcs7$-$1\farcs0$ during the observations.

Each slit position yielded a 2D echelle spectrum which we rectified, reduced, and calibrated. The reduction process first involved subtracting raw NIRSPEC images by sky spectra after cleaning cosmic rays. A normalized flat-field image was then divided into the spectra prior to rectification. To map the curved Br α echelle order onto orthogonal spatial and spectral axes, we used

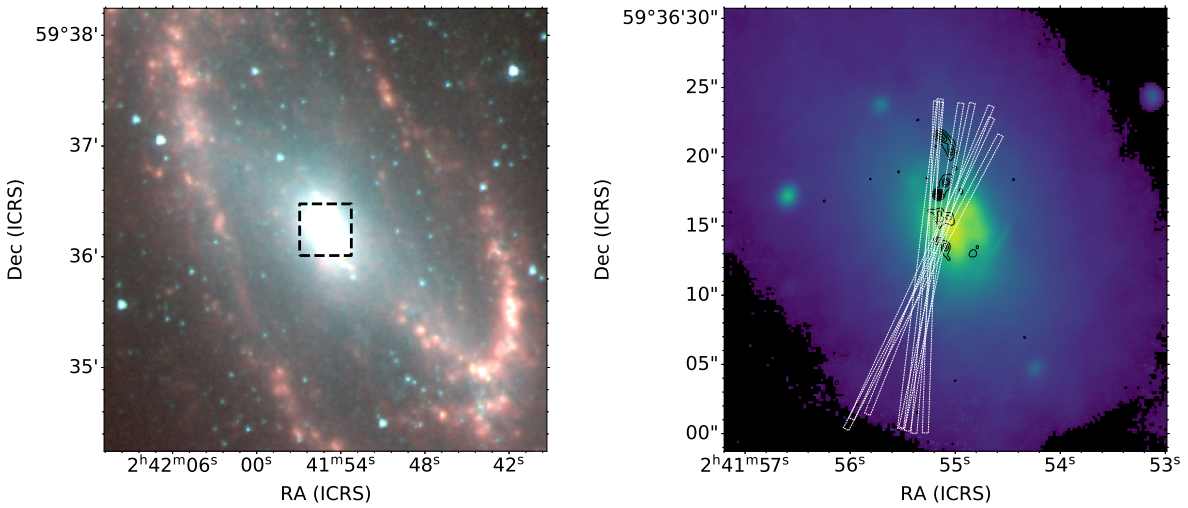

Figure 5.1: The nuclear region of Maffei 2. *Left*) Spitzer IRAC three-color image: red is 5.8μm, green is 4.5μm, and blue is 3.6μm. The large-scale bar ($\sim$3 kpc) converges to the $\lesssim 0.5$ kpc nuclear starburst. The black box gives the NIRSPEC field of view. *Right*) NIRSPEC SCAM image of the starburst's KL-band continuum with NIRSPEC slit positions illustrated by the white regions. Black contours show the 6cm radio continuum, which resolves into compact sources, potential embedded SSCs, distributed across the center along an S-shaped curve (Tsai et al. 2006). The resolution is $\sim 1'' \simeq 16$ pc at $D = 3.5$ Mpc.

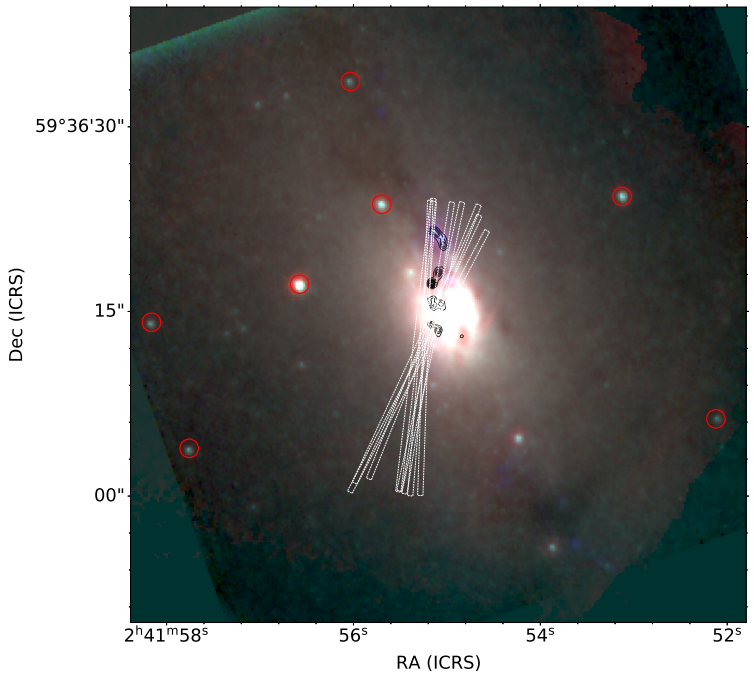

Figure 5.2: Astrometric registration of the NIRSPEC slits. Red circles mark positions of sources from the GAIA DR2 catalog(Gaia Collaboration et al. 2018) that were detected in the SCAM imaging and used for astrometric calibration. Registered slit positions (white rectangles) are accurate to $\sim 0\farcs1$. The background image shows archival HST IR imaging in the green and blue channels and SCAM KL band in red. Contours give the 6cm continuum.

the SPATMAP and SPECMAP procedures within the REDSPEC reduction code[1]. Following rectification, fringe interference patterns were removed by identifying and filtering out associated peaks in the power spectrum. Fig. 5.3 (left) shows the reduced 2D spectra for each position, which have spatial and spectral axes along x and y, respectively. Each pixel has a size of 5.482×10^{-5} μm along the spectral axis and $0\farcs152$ along the spatial axis. The nominal spectral resolution 3 pix $\simeq$ 12 km s^{-1}.

5.2.1 Registration of the Slits with GAIA Sources and Radio Continuum

Accurate astrometry of the slits on the sky is vital for understanding the relation between Br α velocity structure and compact radio sources along with the molecular gas (Fig. 5.2). To perform astrometric calibration, we first combined sky-subtracted SCAM images for each of the eight on-target positions, and measured the pixel positions of bright IR sources detected within each image. The SCAM IR sources were then matched to sources with ICRS coordinates in the Gaia DR2 catalog (Gaia Collaboration et al. 2016, 2018). These matched sources are marked in Fig. 5.2 along with the registered slit positions. Best-fit astrometric solutions are accurate to within $\sim 0\farcs1$ (rms). The registered images were aligned and combined into the slit-free IR continuum image (pixel scale $0\farcs175$) shown in the right panel of Figure 5.1 and as the red channel in Fig. 5.2.

5.2.2 The NIRSPEC Cube

Following the same procedure that we implemented for NGC 253 in Cohen et al. (2020), we combined the eight registered spectra into a spectral cube with RA/DEC on the x- and y-axes and velocity along z. To derive the mapping between pixel coordinates in each 2D spectrum and celestial coordinates, we measured the position of the brightest Br α source in each spectrum and identified its associated radio continuum source.

The cube was then produced by interpolating each echelle spectrum across the slit width, assuming a constant light profile, and projecting the data from each pixel in each wavelength slice onto the coordinate frame of the cube. The sparse data was then smoothed and interpolated onto

[1] https://www2.keck.hawaii.edu/inst/nirspec/redspec.html

the final grid with pixel size 0.″1. A Brackett emission cube was generated by fitting continuum-only pixels with a first order polynomial and subtracting this contribution from the data cube. The Br α cube visualized with channel maps in Figure 5.4.

5.3 Preliminary Results

Maffei 2 exhibits complex kinematic structure in all slit positions, with six bright knots of Br α seemingly connected to each other by an extended component (Fig. 5.3). The knots are associated with the thermal radio continuum sources A-J identified in Tsai et al. (2006). The brightest Br α source is most likely linked to radio sources D and A.

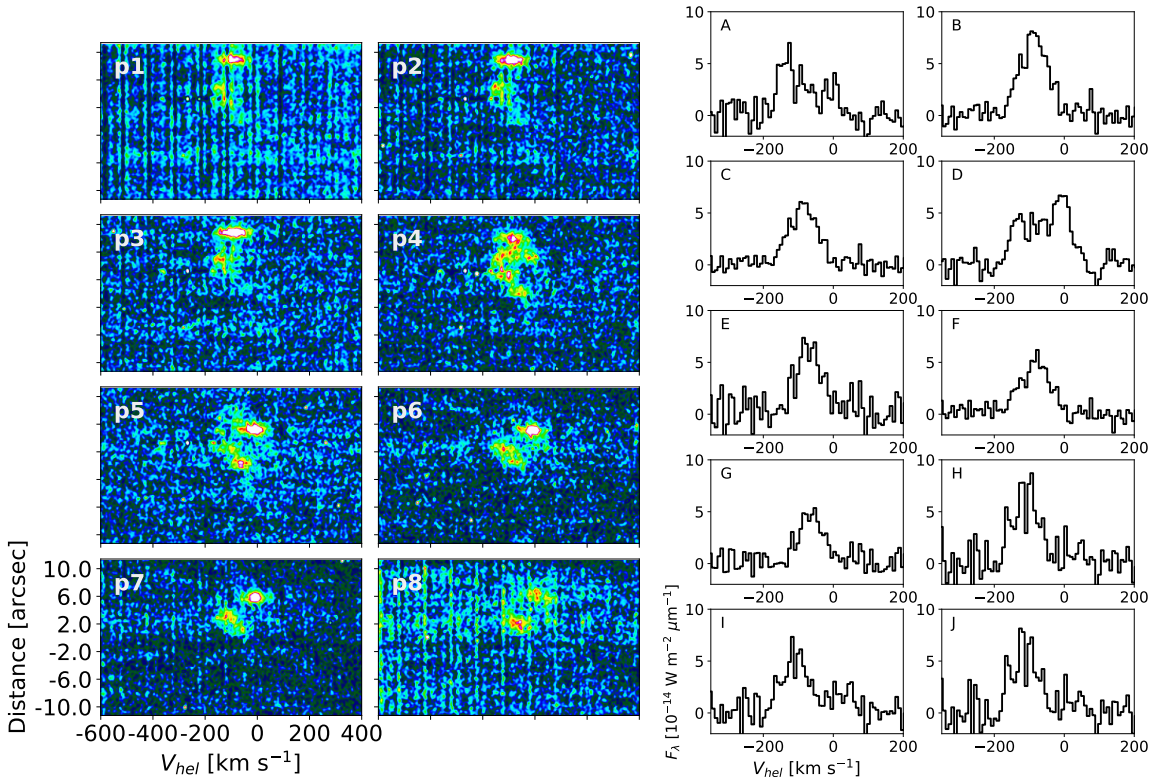

Figure 5.3: Br α spectra of the Maffei 2 starburst from NIRSPEC, corresponding to the slit positions shown in Fig. 5.1. *Left*) Two-dimensional spectra are ordered by decreasing slit PA from the top-left (PA=178°) to bottom-right (PA=152°). Slit distance increases to the north. *Right*) One-dimensional spectra extracted at the positions of radio continuum sources (Tsai et al. 2006). The Br α emission exhibits a complex, rich kinematic structure with both compact and extended features.

Line profiles extracted from a $r = 0.''5$ aperture at the positions of the Tsai et al. (2006) radio sources are shown in Fig 5.3, right. A wide ($\Delta V > 200$ km s^{-1}) double-peaked line structure is

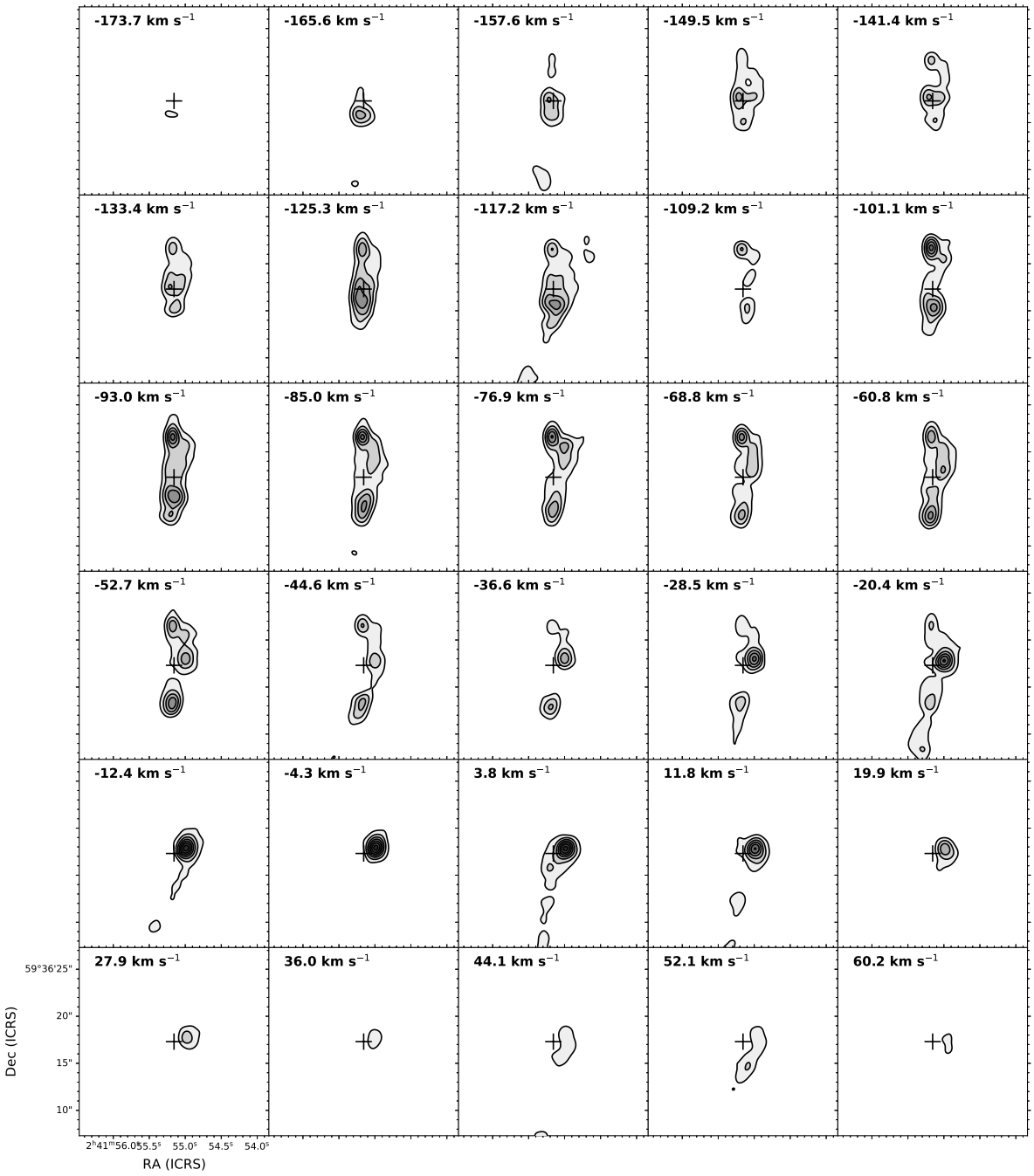

Figure 5.4: Channel maps produced from the NIRSPEC Br α spectral cube, shown at velocity intervals of 8 km s^{-1}. The crosshair marks radio continuum source A from Tsai et al. (2006). Bright, compact H II regions appear to be connected by a ring of diffuse emission.

observed for the bright nuclear source (A+D), with peaks separated by ~ 115 km s^{-1}. When fit with only a single Gaussian profile, the centroid velocity is $V = -33 \pm 4$ km s^{-1}, close to systemic (Table 5.1).

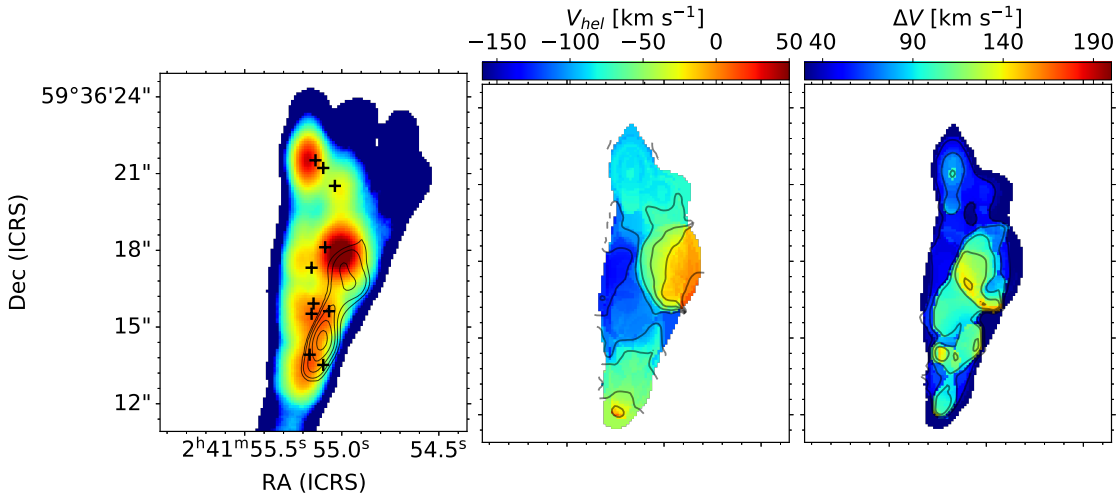

Figure 5.5: Integrated intensity (left), line-of-sight velocity field (middle), and line FWHM (right) maps across the center of Maffei 2. The maps were generated from the Br α cube using pixels at 1.5σ for the intensity map and 4σ for the velocity maps. The black contours within the Br α intensity image show the 4μm continuum intensity. Crosshairs mark radio continuum sources in the intensity map (Tsai et al. 2006).

The channel maps in Fig. 5.4 reveal a clear pattern of gas motions along a path connecting the bright Br α sources. The pattern bears some similarities to the molecular gas structure found in Meier et al. (2008), the most basic of which are a double-peaked morphology in many of the blue channels, and the presence of a bright central source which first peaks in our maps at -52.7 km s^{-1}, dips, then increases in brightness and reaches an absolute maximum near $V \sim 0$ km s^{-1}. Much of the difference between the observed Br α structure and that reported in Meier et al. (2008) may be attributed simply to our lack of coverage in the southwest region. Meier et al. (2008) modelled the nuclear region with a central, ~ 200 pc bar along which gas may flow into the central region. The northern-most source, associated with radio continuum source B is very close to the intersection of the large-scale bar's x_2 orbits and the nuclear ring (MT12). Fig. 5.4 appears to exhibit the pattern of an expanding, edge-on ring from $V = -165.6$ km s^{-1} to $V = -36.6$ km s^{-1}, with the compact radio knots distributed along its circumference and in its center. The first brightness peak of the central source is at the red end of the ring, but its main peak is apparently separate. It is currently unclear if the model from Meier et al. (2008) can explain the bulk of the Br α velocity structure.

Figure 5.5 gives the Br α integrated intensity map along with the velocity field and FWHM map. The 4μm integrated continuum intensity is shown as contours on the Br α intensity map. The continuum is detected as two lobes near the brightest nuclear Br α source along with the

southern Br α sources, with a slight spatial offset relative to the line. The velocity field shows a clear structure of curved contours wrapping around the bright central source, with ~ -100 km s^{-1} blue-shifted emission directly to its east. The line width peaks between the continuum lobes, on the southeast side of the central source between radio sources D and A.

Further analysis is required to determine how much of the velocity structure may be attributed to gas flows along a nuclear bar/ring, or to outflow from feedback. MT12 finds evidence for an entrained molecular outflow, appearing as C_2H lobes extending along the minor-axis. The NIRSPEC channel maps (Fig. 5.4) exhibit *tentative* evidence of a minor-axis lobe immediately to the SW of the northern-most Br α source, visible in the $V = -133$ to -20 km s^{-1} velocity channels. A more detailed investigation should reveal whether or not this feature may be attributed to the nuclear ring/bar structure.

5.4 Summary & Future Work

The constructed Br α cube, with $1''$ and 12 km s^{-1} resolutions, reveals a nuclear bar and associated knots of star formation in the central $\sim 10''$ of Maffei 2. Further investigation should reveal the dynamical origin of the observed velocity features. In particular:

1. The velocity field will be fit with models of pure circular motion to obtain a residual, non-circular velocity field. This residual field will be used to constrain the bar properties and look for signs of outflow. Inflow properties will be estimated and compared to the $\sim 0\farcs7$ M$_\odot$ yr^{-1} molecular inflow found in MT12.

2. Star formation properties will be estimated from the line fluxes and widths and compared to the gas inflow.

3. The brightest Br α source is the dominant source in channels redward of systemic, exhibits curved velocity contours and corresponds to the maximum line width in the region. Its line profile appears double-peaked. The nature of this mysterious source will be investigated further.

4. By directly relating the Br α to the molecular gas MT12, we will develop the first empirically-based multi-phase gas model of the central starburst in Maffei 2. We can compare to the NGC 253 starburst (Cohen et al. 2020) to determine how the results fit into the current theory of central mass growth in galaxies.

CHAPTER 6

Parsec-scale Ionized Gas Motions in the Forming Galactic Center of NGC 253 with NIRSPAO

This chapter reports preliminary results from NIRSPAO observations across the galactic center of NGC 253 acquired in Aug 2019. Analysis for this project, which is follow-up work on Ch. 3, is ongoing. By constructing a cube and measuring the velocity field, we aim to constrain the mass content and growth of the nuclear star cluster and potential SMBH.

Using NIRSPEC behind AO (NIRSPAO), we investigate ionized gas kinematics at $\sim 0\farcs1 \simeq 2$ pc resolution near the radio-bright galactic center of NGC 253. The target region hosts a r $\sim$50 pc nuclear bar associated with forming super star clusters along with the bright non-thermal radio peak, a candidate SMBH. We have used GAIA sources to derive astrometry of KL-band continuum imaging acquired with the Slit-Viewing Camera, allowing us to produce an AO mosaic of the central $\sim$ $8'' = 150$ pc region in addition to registering the NIRSPAO slit positions. The Br α spectra in the region is extended, rather than concentrated to bright compact clumps, suggesting that the observations are tracing structure. A clear $\sim$50 km s^{-1} arcsec^{-1} gradient likely reflects motions associated with the nuclear bar, and may be used to constrain the central mass structure.

6.1 Introduction

Galactic nuclei are diverse, complex environments: massive star clusters, supermassive black holes (SMBHs), and nuclear star clusters are key elements in the evolution of galactic nuclei and their potential for galactic-scale feedback. The Galactic Center contains a SMBH and some of the largest clusters in the Galaxy, including a nuclear cluster. How these structures evolve and affect

each other is a subject of active investigation (e.g., Do et al. 2013; Stolte et al. 2015; Do et al. 2017; Petts & Gualandris 2017). Nearby galaxies give different views of nuclear clusters and SMBHs, but requires spatial resolutions of $\lesssim$0.1″to separate cluster-scale dynamical structure.

NGC 253 is one of the closest (4 Mpc) starburst galaxies with an active starburst forming many large nuclear super star clusters (SSCs). An unusually bright radio source, TH2 (Turner & Ho 1985; Antonucci & Ulvestad 1988, hereafter TH85;), resides near the kinematic center of the galaxy (Rosenberg et al. 2013). TH2 is distinctive in that it is undetected in the IR continuum in AO imaging (Fernández-Ontiveros et al. 2009). Its non-thermal radio continuum suggests two possibilities: an unusually bright supernova remnant (SNR) or, given its location near the galaxy's kinematic center, a faint AGN. If TH2 were a SNR, it would be 100 times brighter than the Galaxy's brightest SNR, Cas A. The lack of an X-ray counterpart (Müller-Sánchez et al. 2010; Rosenberg et al. 2013) along with the presence of high-J CO, HCN, and dust emission(e.g., Meier et al. 2015; Leroy et al. 2018; Mangum et al. 2019) suggests very high extinctions ($A_V \gtrsim 20$). If TH2 is indeed a weak AGN, it would be a valuable nearby example of the starburst-AGN interaction. Molecular outflows have been resolved in ALMA images of NGC 253(Bolatto et al. 2013; Krieger et al. 2019), but their role in suppressing or regulating star formation is not clear. While the outflows appear to originate to the southwest of the nucleus, one can argue for a nuclear origin as well.

We previously observed NGC 253 at $\sim$1″ resolution in a half-night NIRSPEC run, from which we generated a Br α spectral cube to probe the velocity structure of the clusters near the molecular outflows (Cohen et al. 2020, hereafter C20). Our observations detected three Br α sources. Source SW1 is a giant star-forming region located at the starburst's IR peak (Kornei & McCrady 2009). The subject of this paper is the more likely candidate for the galactic center: Brackett source NE1 at the radio core, containing non-thermal source TH2 and nearby SSCs.

The line profile of NE1 is complex, with clear asymmetry and evidence of at least 3 distinct components (C20). Even at $\sim$1″ resolution these line components exhibit significant variation over the source's extent. Of particular interest is the potential outflow component suggested by the broad (ΔV $\sim$350 km s^{-1},FWHM) blue wing and dipole structure in the velocity field. The estimated outflow velocities are v $\gtrsim$100-175 km s^{-1} (de-projected); if extinction is suppressing the far side flow, the velocities are larger.

In this project we present observations of the central Br α region NE1 in NGC 253 with NIRSPAO (LGS) in echelle mode. Work on this project is on-going. We have generated a mosaic from Slit-Viewing Camera images of the KL-band and derived its astrometric calibration, yielding accurate celestial positioning of the NIRSPAO slits. The echelle spectra have been reduced and calibrated, and partially analyzed. Our primary goal is to measure the velocity field and derive properties of the nuclear bar, outflows from SSCs, or other dynamical influences. To this end, we will combine the spectra into a cube and create a virtual "IFU", similar to our method in C20.

6.2 Observations and Data

NGC 253 was observed with NIRSPAO (LGS) during the second half-night of August 14th, 2019. The $2.26'' \times 0.0407''$ slit was oriented at position angle PA$\sim$45°, aligned along the nuclear bar major axis (C20) and line of bright, compact radio continuum sources (TH85). The slit was initially positioned at the approximate location of the radio source TH2, which has no IR counterpart that could be used to center the slit. Sporadic cloud cover created additional difficulty in acquiring bright tip-tilt reference objects and resulted in a $\sim$1$''$ offset between the desired target position and the observed slit position. Nonetheless, we stepped the slit across the $\sim$4$''$ around the radio core, obtaining 13 spectra of the Br α line in the KL-band (Fig. 6.1). Sky spectra were obtained after the 4th and 7th on-target exposures.

To reduce the NIRSPAO spectra, we first applied spatial and spectral rectification to all raw NIRSPEC images using the `SPATMAP` and `SPECMAP` routines from the REDSPEC pipeline[1]. A dispersion solution (wavelength calibration) is produced during the final step of rectification, resulting in a 2D spectrum on a linear wavelength grid that is orthogonal to the spatial axis (also linear). This process involved use of arc lamp frames that we acquired at the beginning of the observing run along with spectra of standard star HD225200 (class A0V) taken prior to the science target. The rectified spectra were sky-subtracted and divided by a median-normalized flat-field image, and hot/cold pixels were removed. The reduced spectra, which have pixel scales 0.″012 pix^{-1} along the slit and 3.652×10^5 μm along the dispersion axis, are shown in Fig. 6.3. The

[1] `https://www2.keck.hawaii.edu/inst/nirspec/redspec.html`

spatial and spectral resolutions are $0\farcs15$ (measured in the SCAM image) and ~ 12 km s$^{-1}\simeq 5$ pix, respectively.

6.3 AO Imaging of the 4μm Continuum and Registration to Optical Clusters

A Slit-Viewing Camera (SCAM) mosaic image was constructed to study the IR morphology near the radio nucleus at high-resolution and determine the celestial positions of the slits with respect to TH2. SCAM images of the slit on the sky were simultaneously acquired during spectral integrations. To reduce these images we first subtracted the on-target SCAM images by SCAM blank sky imaging and combined all valid frames obtained at each indiviual slit position. We then performed source detection in each of these combined images and measured the pixel positions of bright IR sources. These IR sources were then matched to sources with ICRS coordinates in the GAIA DR2 catalog (Gaia Collaboration et al. 2018), likely optical clusters, and a best-fit astrometric solution was determined for the SCAM image at each slit position. The astrometry is accurate to $\sim 0\farcs05$ (rms residual). The calibrated images were registered and combined into the mosaic shown in Fig. 6.1 with the matched GAIA sources identified (pixel scale $0\farcs015$). Fig. 6.1 also shows an archival HST IR image for comparison.

The three-color image in Fig. 6.2 gives a multi-wavelength picture of the obsered region near the radio core in NGC 253, with red showing the SCAM 4μm continuum, green showing the H-band continuum from HST, and blue showing CO(3–2) from an archival ALMA map ($\sim 0\farcs3$ beam). Dashed grey contours overlayed on this image show the velocity field of Br α from C20 measured at $\sim$1$''$ resolution. The 2cm radio continuum ($\sim 0\farcs2$ beam) is shown as black solid contours, and the position of radio source TH2 is marked.

Generally the molecular gas appears to be anti-correlated with the IR continuum continuum. In particular, the $\sim$2$''\simeq$30 pc hole in the IR emission is filled with a CO cloud which resolves into star-forming cores in higher-resolution ALMA maps (Leroy et al. 2018; Mangum et al. 2019). The velocity contours curve across a bridge of molecular gas between the large cloud and TH2 (immediately to the NE of TH2), indicative of a $r \sim 50$ pc nuclear bar. This region may represent inflow into the radio nucleus along a nuclear bar, feeding the formation of a giant nuclear star

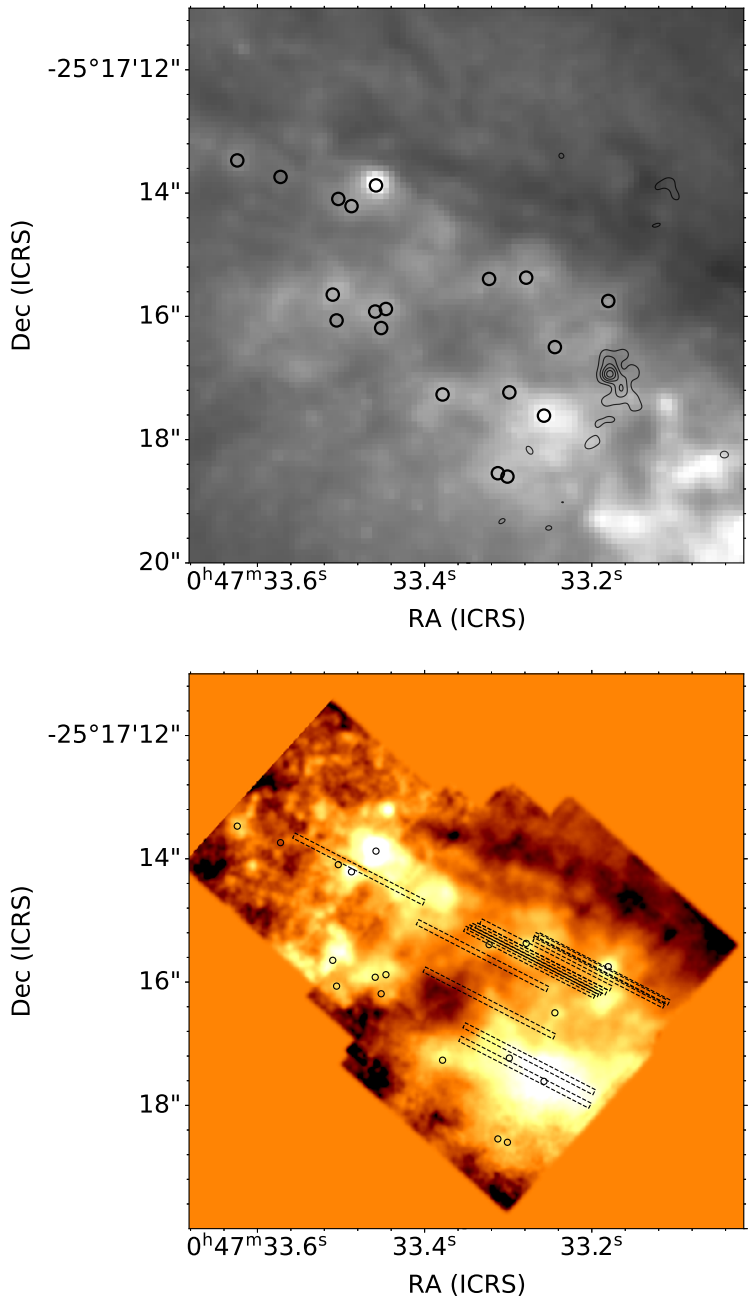

Figure 6.1: NIRSPAO SCAM imaging near the starburst core in NGC 253. *Top*) shows NIR imaging from HST WFC3, with contours showing 2cm continuum. Black circles mark sources in GAIA DR2 (Gaia Collaboration et al. 2018) that were matched to KL-band sources. *Bottom*) SCAM KL-band mosaic of NGC 253 with $\sim 0\farcs1 \simeq 2$ pc resolution. NIRSPAO slit positions ($0\farcs041 \times 2\farcs26$) are shown as the black rectangles.

cluster along with a potential SMBH or weak AGN. The radio nucleus appears to be NGC 253's forming galactic center.

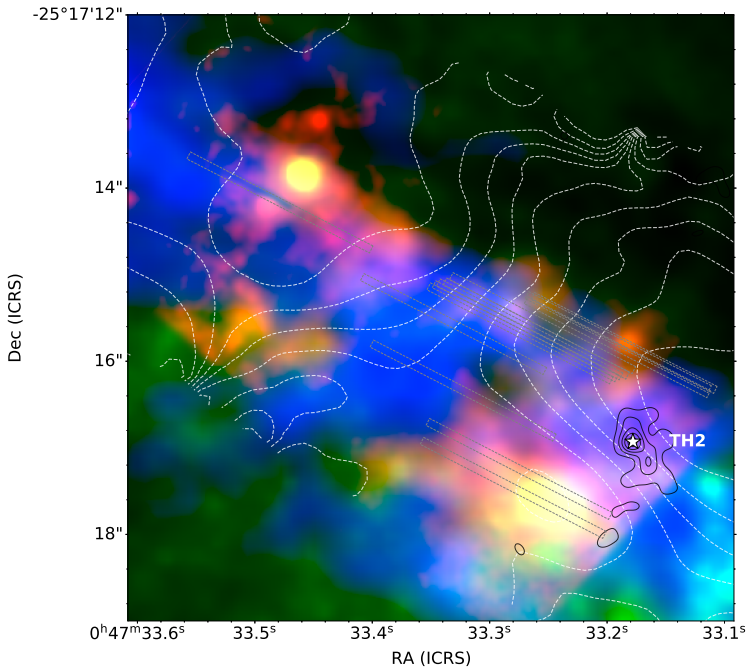

Figure 6.2: Three-color image of the center of NGC 253: the red, green, and blue channels show NIRSPAO SCAM, HST WFC3, and ALMA CO(3–2) imaging, respectively. The NIRSPAO slits (grey rectangles) span the top of the nuclear bar found in lower resolution observations in Cohen et al. (2020). The lower resolution velocity field is shown here by the grey contours, which curve near the ends of the bar. The nuclear bar could be funneling gas to non-thermal radio source TH2 at the galactic center of NGC 253 (Turner & Ho 1985). With the NIRSPAO spectra, we hope to constrain this potential nuclear inflow along with feedback from nuclear SSCs and TH2.

6.4 Preliminary Results from Spectroscopy

Although the slits missed target TH2, spectra were successfully acquired across the potential bar-induced central inflow, the molecular "bridge" to TH2, extending to the bright IR source to the SE of TH2 (Fig. 6.2). We can thus produce a velocity field at $\sim$2 pc resolution and constrain inflow into the galactic center induced by the bar potential and constrain the influence of feedback from forming clusters and/or TH2 on the potential inflow.

Fig. 6.3 shows the reduced 2D echelle spectra from NIRSPEC in which Br α and/or continuum is detected. The majority of slit positions detect both line and continuum. Br α is detected as extended emission throughout the observed region, rather than concentrated to bright compact cores as might be expected of SSCs. SSCs in this region are thus likely to be extremely young and obscured.

For the slits in the candidate bar-inflow region, the Br α exhibits a clear linear gradient apparent

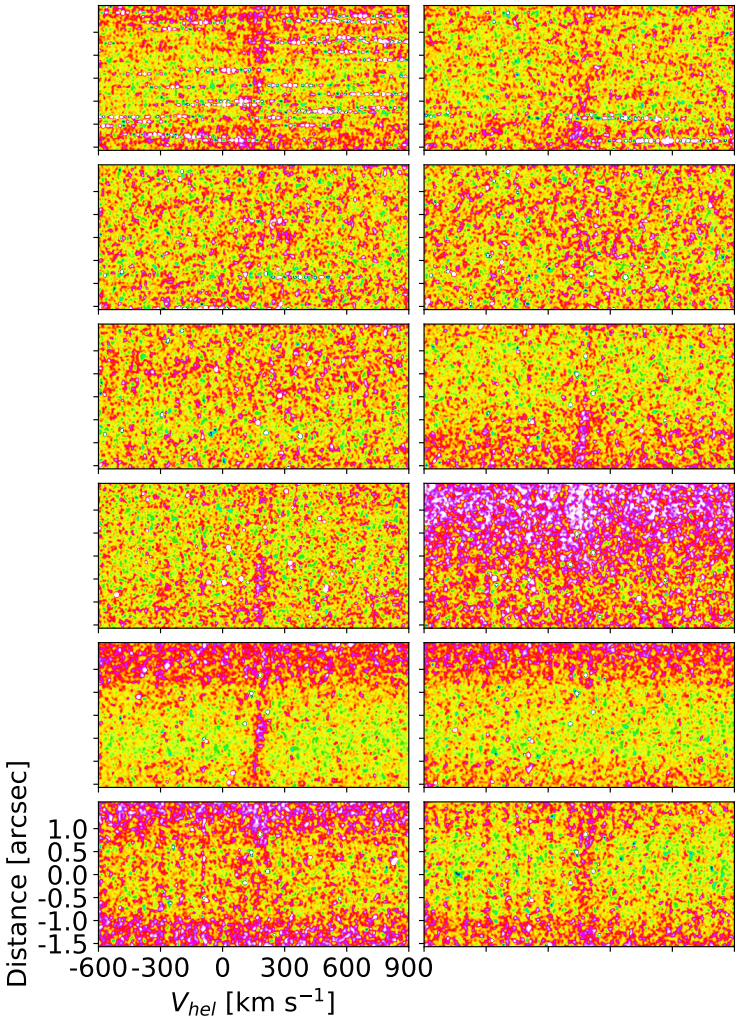

Figure 6.3: NIRSPAO spectra of Br α in the NGC 253 starburst, corresponding to the slit positions shown in Fig. 6.1. In these spectra the distance axis from bottom to top runs NE to SW. Br α is detected in the majority of positions. The observed Br α is extended rather than concentrated to compact knots, while the continuum appears localized to certain positions. A velocity gradient as large as $\sim +50$ km s^{-1} arcsec^{-1} or 3 km s^{-1} pc^{-1} is found along the slit axis at slit positions near the top of the bar.

in Fig. 6.3 slanting across the slit direction. The gradient is $\sim 30 - 50$ km s^{-1} arcsec^{-1} or 2-3 km s^{-1} pc^{-1}. This is consistent with our lower resolution measurements of the velocity field, and roughly consistent with the nuclear bar model (Das et al. 2001), and generally consistent with flow along bar arms.

The closest slit position to TH2 where the gradient persists is about $0\farcs7 \simeq 12$ pc-projected away. The dynamical mass estimated from the observed gradient is $M_{\rm dyn}(r \lesssim 12\,{\rm pc}) \gtrsim 1-3\times10^6$ M$_\odot$, consistent with the masses of nuclear star clusters. Much of the mass could be a SMBH responsible for powering the non-thermal emission from TH2. The predicted sphere of influence of

a candidate SMBH is $\sim$8 pc, comparable to but perhaps just short of our closest slit position (C20). More work is required to constrain the central mass structure and inflow properties, including bar parameters and the relation to the $\sim$30 pc GMC adjacent to the radio nucleus. In particular, combining the 2D spectra into a cube will yield a higher S/N ratio, and allow us to measure and investigate the velocity structure and potential curvature or non-linear deviations of the gradient.

6.5 Summary & Future Work

We have observed the radio nucleus in NGC 253 with NIRSPAO to investigate the fine structure of gas motions (2 pc resolutio) near its forming nuclear star cluster and SMBH. Thus far, we have generated a 4μm continuum AO image and derived its astrometry, allowing a multi-wavelength perspective of the starburst core and an accurate registration of the NIRSPAO slits. A comparison with high-resolution CO mapping suggests a channel of gas inflow, possibly linked to a GMC $\sim 40-50$ pc from TH2 (in-projection). Reduced spectra, which were mapped across the 4$''$region, exhibit extended Br α with a clear NE-SW velocity gradient of $\sim$ 30 km s^{-1} arcsec^{-1}. This is consistent with radial flow along a nuclear bar.

Completing the picture of kinematics in the NGC 253 will involve the construction and analysis of a NIRSPAO cube. This process should be immediately possible, as we have already derived the astrometry of the slits. Once we have generated the cube we will extract the velocity field and perform dynamical modeling to constrain the nuclear bar and associated inflow along with feedback from the heavily embedded nuclear star cluster.

CHAPTER 7

Conclusions and Future Outlook

In this dissertation we have uncovered a diverse range of processes in starburst galaxies forming SSCs. With its high-spectral and spatial resolution and its ability to observe the Br α emission line, NIRSPEC proved to be an ideal tool for observing embedded H II regions near giant forming clusters. Our investigations yield the following insight into the formation mechanisms of massive clusters and role of starbursts in galaxies:

1. The process of gas clearing in the most massive clusters, SSCs and GCs, is *not* an extrapolation of that observed for less-massive stellar clusters ($\lesssim 10^3$ M$_\odot$). In dwarf galaxy NGC 5253 we have found a conclusive *absence* of a cluster wind or any explosive ionized outflow launched by the $\gtrsim 10^5$ M$_\odot$ embedded SSC. The narrow line width ($\Delta V \sim 75$ km s^{-1}) is comparable to the SSC's escape velocity, and not much larger than line widths of compact Galactic H II regions. We have discovered another excellent candidate for feedback suppression in dwarf starburst NGC 1569. Its giant H II region, powered by two embedded SSCs, has a line width of only $\Delta V \sim 45$ km s^{-1}. The findings support the theory that extreme pressures within the densest SSCs may confine ionized wind regions and suppress massive star feedback, greatly slowing gas dispersal (Silich et al. 2020).

2. Environment, including the mechanism fueling cluster formation, appears to play a vital role in determining the influence of feedback. The ongoing formation of SSCs in NGC 5253 and possibly NGC 1569 is likely fueled by giant circumgalactic filaments of gas flowing into highly concentrated regions with extreme pressures, perfect environments for forming long-lived GC-like objects. The star formation efficiency is extremely high ($\gtrsim 50\%$) in such systems. NGC 253 and Maffei 2, on the other hand, are building central bulges and galactic centers within. Our work suggests that ~ 100 pc nuclear mass structures, bars in particular,

regulate the inflow and central mass growth. A forming galactic center may power intense feedback that prevents inflow. Indeed, star formation is inefficient in these systems, requiring a huge gas inward mass flux required to sustain the formation of massive clusters.

3. Starbursts, such as those in the centers of NGC 253 and Maffei 2, exhibit diverse behavior with varying degree of influence on their host galaxies. The connection between environment and feedback is complex. The center of NGC 253 appears to host one concentrated region of feedback which may power its entire galactic wind. Maffei 2 on the other hand hosts concentrations of forming clusters potentially indicative of explosive events, and at the least stirring up the gas kinematics. Observing more starbursts with NIRSPEC will be vital in uncovering the underlying physical processes determining the influence of starbursts and how they shape galaxy evolution.

The work presented here represents only the beginning of a rich future for observational study of super star clusters. A major aspect of this observing program will be expanding the sample of embedded SSCs observed with NIRSPEC. We were awarded a half-night in April 2020 to observe new targets Mrk 71, Haro 2, NGC 3125 along with follow-up in NGC 1569, however the observing run was cancelled due to the coronavirus pandemic. These sources will be priority targets in future NIRSPEC proposals.

A complete physical picture of extreme star formation must encompass not only the ionized gas but also the dense molecular gas, neutral gas, and dust associated with embedded massive clusters. ALMA and the VLA, will be utilized to obtain complimentary data necessary for understanding multi-phase gas dynamics. The synthesis of such observations with high-resolution IR data from NIRSPEC and other cutting-edge instruments should shed light on some of the most long-standing mysteries surrounding star formation and the evolution of massive stellar systems through cosmic time.

Bibliography

Allison, R. J., S. P. Goodwin, R. J. Parker, S. F. Portegies Zwart, & R. de Grijs. 2010, MNRAS, 407, 1098

Alonso-Herrero, A., T. Takagi, A. J. Baker, G. H. Rieke, M. J. Rieke, M. Imanishi, & N. Z. Scoville. 2004, ApJ, 612, 222

Anantharamaiah, K. R. & W. M. Goss. 1996, ApJ, 466, L13

Ando, R., K. Nakanishi, K. Kohno, T. Izumi, S. Martín, N. Harada, S. Takano, N. Kuno, N. Nakai, H. Sugai, K. Sorai, T. Tosaki, K. Matsubayashi, T. Nakajima, Y. Nishimura, & Y. Tamura. 2017, ApJ, 849, 81

Antonucci, R. R. J. & J. S. Ulvestad. 1988, ApJ, 330, L97

Arnaboldi, M., M. Capaccioli, E. Cappellaro, E. V. Held, & B. Koribalski. 1995, AJ, 110, 199

Arribas, S., L. Colina, E. Bellocchi, R. Maiolino, & M. Villar-Martín. 2014, A&A, 568, A14

Astropy Collaboration, T. P. Robitaille, E. J. Tollerud, P. Greenfield, M. Droettboom, E. Bray, T. Aldcroft, M. Davis, A. Ginsburg, A. M. Price-Whelan, W. E. Kerzendorf, A. Conley, N. Crighton, K. Barbary, D. Muna, H. Ferguson, F. Grollier, M. M. Parikh, P. H. Nair, H. M. Unther, C. Deil, J. Woillez, S. Conseil, R. Kramer, J. E. H. Turner, L. Singer, R. Fox, B. A. Weaver, V. Zabalza, Z. I. Edwards, K. Azalee Bostroem, D. J. Burke, A. R. Casey, S. M. Crawford, N. Dencheva, J. Ely, T. Jenness, K. Labrie, P. L. Lim, F. Pierfederici, A. Pontzen, A. Ptak, B. Refsdal, M. Servillat, & O. Streicher. 2013, A&A, 558, A33

Athanassoula, E. 1984, , 114, 319

—. 1992, MNRAS, 259, 345

Athanassoula, E. & M. Bureau. 1999, ApJ, 522, 699

Athanassoula, E., R. E. G. Machado, & S. A. Rodionov. 2013, MNRAS, 429, 1949

Barth, A. J., B. D. Boizelle, J. Darling, A. J. Baker, D. A. Buote, L. C. Ho, & J. L. Walsh. 2016, ApJ, 822, L28

Bastian, N. & S. P. Goodwin. 2006, MNRAS, 369, L9

Baumgardt, H., P. Kroupa, & G. Parmentier. 2008, MNRAS, 384, 1231

Beck, S., J. Turner, J. Lacy, & T. Greathouse. 2015, ApJ, 814, 16

Beck, S., J. Turner, J. Lacy, T. Greathouse, & O. Lahad. 2013, ApJ, 767, 53

Beck, S. C. 2008, A&A, 489, 567

Beck, S. C., J. H. Lacy, J. L. Turner, A. Kruger, M. Richter, & L. P. Crosthwaite. 2012, ApJ, 755, 59

Beck, S. C., J. L. Turner, P. T. P. Ho, J. H. Lacy, & D. M. Kelly. 1996, ApJ, 457, 610

Bendo, G. J., R. J. Beswick, M. J. D'Cruze, C. Dickinson, G. A. Fuller, & T. W. B. Muxlow. 2015, MNRAS, 450, L80

Bendo, G. J., R. E. Miura, D. Espada, K. Nakanishi, R. J. Beswick, M. J. D'Cruze, C. Dickinson, & G. A. Fuller. 2017, MNRAS, 472, 1239

Böker, T., J. Falcón-Barroso, E. Schinnerer, J. H. Knapen, & S. Ryder. 2008, AJ, 135, 479

Bolatto, A. D., S. R. Warren, A. K. Leroy, F. Walter, S. Veilleux, E. C. Ostriker, J. Ott, M. Zwaan, D. B. Fisher, A. Weiss, E. Rosolowsky, & J. Hodge. 2013, Nature, 499, 450

Buta, R. & F. Combes. 1996, , 17, 95

Buta, R. J. & M. L. McCall. 1999, ApJS, 124, 33

Calzetti, D. 1997, AJ, 113, 162

Calzetti, D., G. R. Meurer, R. C. Bohlin, D. R. Garnett, A. L. Kinney, C. Leitherer, & T. Storchi-Bergmann. 1997, AJ, 114, 1834

Calzetti, D., K. E. Johnson, A. Adamo, J. S. Gallagher, III, J. E. Andrews, L. J. Smith, G. C. Clayton, J. C. Lee, E. Sabbi, L. Ubeda, H. Kim, J. E. Ryon, D. Thilker, S. N. Bright, E. Zackrisson, R. C. Kennicutt, S. E. de Mink, B. C. Whitmore, A. Aloisi, R. Chandar, M. Cignoni, D. Cook, D. A. Dale, B. G. Elmegreen, D. M. Elmegreen, A. S. Evans, M. Fumagalli, D. A. Gouliermis, K. Grasha, E. K. Grebel, M. R. Krumholz, R. Walterbos, A. Wofford, T. M. Brown, C. Christian, C. Dobbs, A. Herrero, L. Kahre, M. Messa, P. Nair, A. Nota, G. Östlin, A. Pellerin, E. Sacchi, D. Schaerer, & M. Tosi. 2015, ApJ, 811, 75

Cantó, J., A. C. Raga, & L. F. Rodríguez. 2000, ApJ, 536, 896

Carles, C., H. Martel, S. L. Ellison, & D. Kawata. 2016, MNRAS, 463, 1074

Chevalier, R. A. & A. W. Clegg. 1985, Nature, 317, 44

Chomiuk, L. & E. M. Wilcots. 2009, AJ, 137, 3869

Clark, D. M., S. S. Eikenberry, S. N. Raines, N. Gruel, R. Elston, R. Guzman, G. Boreman, & P. E. Glenn. 2013, MNRAS, 428, 2290

Cohen, D. P., J. L. Turner, & S. M. Consiglio. 2020, MNRAS, 493, 627

Cohen, D. P., J. L. Turner, S. M. Consiglio, E. C. Martin, & S. C. Beck. 2018, ApJ, 860, 47

Combes, F., S. García-Burillo, A. Audibert, L. Hunt, A. Eckart, S. Aalto, V. Casasola, F. Boone, M. Krips, S. Viti, K. Sakamoto, S. Muller, K. Dasyra, P. van der Werf, & S. Martin. 2019, A&A, 623, A79

Comerón, S., J. H. Knapen, J. E. Beckman, E. Laurikainen, H. Salo, I. Martínez-Valpuesta, & R. J. Buta. 2010, MNRAS, 402, 2462

Consiglio, S. M. 2018, PhD thesis, UCLA

Consiglio, S. M., J. L. Turner, S. Beck, & D. S. Meier. 2016, ApJ, 833, L6

Consiglio, S. M., J. L. Turner, S. Beck, D. S. Meier, S. Silich, & J.-H. Zhao. 2017, ArXiv e-prints, arXiv:1710.10282

Conti, P. S. 1991, ApJ, 377, 115

Cresci, G., L. Vanzi, M. Sauvage, G. Santangelo, & P. van der Werf. 2010, A&A, 520, A82

Das, M., K. R. Anantharamaiah, & M. S. Yun. 2001, ApJ, 549, 896

Davidge, T. J. 2016, ApJ, 818, 142

Davis, T. A., M. Bureau, K. Onishi, M. Cappellari, S. Iguchi, & M. Sarzi. 2017, MNRAS, 468, 4675

Davis, T. A., M. Bureau, K. Onishi, F. van de Voort, M. Cappellari, S. Iguchi, L. Liu, E. V. North, M. Sarzi, & M. D. Smith. 2018, MNRAS, 473, 3818

de Grijs, R., P. Anders, E. Zackrisson, & G. Östlin. 2013, MNRAS, 431, 2917

De Pree, C. G., D. J. Wilner, & W. M. Goss. 2011, AJ, 142, 177

De Pree, C. G., D. J. Wilner, W. M. Goss, W. J. Welch, & E. McGrath. 2000, ApJ, 540, 308

De Pree, C. G., D. J. Wilner, A. J. Mercer, L. E. Davis, W. M. Goss, & S. Kurtz. 2004, ApJ, 600, 286

Di Teodoro, E. M. & F. Fraternali. 2015, MNRAS, 451, 3021

Do, T., J. R. Lu, A. M. Ghez, M. R. Morris, S. Yelda, G. D. Martinez, S. A. Wright, & K. Matthews. 2013, ApJ, 764, 154

Do, T., A. Ghez, M. Morris, J. Lu, S. Chappell, A. Feldmeier-Krause, W. Kerzendorf, G. D. Martinez, N. Murray, & N. Winsor. 2017, in IAU Symposium, Vol. 322, The Multi-Messenger Astrophysics of the Galactic Centre, ed. R. M. Crocker, S. N. Longmore, & G. V. Bicknell, 222–230

Dreher, J. W., K. J. Johnston, W. J. Welch, & R. C. Walker. 1984, ApJ, 283, 632

Dyson, J. E., R. J. R. Williams, & M. P. Redman. 1995, MNRAS, 277, 700

Elmegreen, B. G. 2018, ApJ, 869, 119

Engelbracht, C. W., M. J. Rieke, G. H. Rieke, D. M. Kelly, & J. M. Achtermann. 1998, ApJ, 505, 639

Fernández-Ontiveros, J. A., M. A. Prieto, & J. A. Acosta-Pulido. 2009, MNRAS, 392, L16

Font, J., J. E. Beckman, J. Zaragoza-Cardiel, K. Fathi, B. Epinat, & P. Amram. 2014, MNRAS, 444, L85

Forbes, D. A., E. Polehampton, I. R. Stevens, J. P. Brodie, & M. J. Ward. 2000, MNRAS, 312, 689

Gaia Collaboration, T. Prusti, J. H. J. de Bruijne, A. G. A. Brown, A. Vallenari, C. Babusiaux, C. A. L. Bailer-Jones, U. Bastian, M. Biermann, D. W. Evans, & et al. 2016, A&A, 595, A1

Gaia Collaboration, A. G. A. Brown, A. Vallenari, T. Prusti, J. H. J. de Bruijne, C. Babusiaux, C. A. L. Bailer-Jones, M. Biermann, D. W. Evans, L. Eyer, & et al. 2018, A&A, 616, A1

Ginsburg, A., W. M. Goss, C. Goddi, R. Galván-Madrid, J. E. Dale, J. Bally, C. D. Battersby, A. Youngblood, R. Sankrit, R. Smith, J. Darling, J. M. D. Kruijssen, & H. B. Liu. 2016, A&A, 595, A27

Goodwin, S. P. & N. Bastian. 2006, MNRAS, 373, 752

Gray, W. J., M. S. Oey, S. Silich, & E. Scannapieco. 2019, ApJ, 887, 161

Greve, A., A. Tarchi, S. Hüttemeister, R. de Grijs, J. M. van der Hulst, S. T. Garrington, & N. Neininger. 2002, A&A, 381, 825

Grocholski, A. J., R. P. van der Marel, A. Aloisi, F. Annibali, L. Greggio, & M. Tosi. 2012, AJ, 143, 117

Günthardt, G. I., M. P. Agüero, J. A. Camperi, R. J. Díaz, P. L. Gomez, G. Bosch, & M. Schirmer. 2015, AJ, 150, 139

Günthardt, G. I., R. J. Díaz, M. P. Agüero, G. Gimeno, H. Dottori, & J. A. Camperi. 2019, AJ, 158, 115

Hamann, F. & M. Simon. 1986, ApJ, 311, 909

Harris, W. E. 1996, AJ, 112, 1487

He, C.-C., M. Ricotti, & S. Geen. 2020, MNRAS, 492, 4858

Heckman, T. M. 2001, in Astronomical Society of the Pacific Conference Series, Vol. 240, Gas and Galaxy Evolution, ed. J. E. Hibbard, M. Rupen, & J. H. van Gorkom, 345

Hénault-Brunet, V., M. Gieles, C. J. Evans, H. Sana, N. Bastian, J. Maíz Apellániz, W. D. Taylor, N. Markova, E. Bressert, A. de Koter, & J. T. van Loon. 2012, A&A, 545, L1

Henry, A. L., J. L. Turner, S. C. Beck, L. P. Crosthwaite, & D. S. Meier. 2007, AJ, 133, 757

Ho, P. T. P., S. C. Beck, & J. L. Turner. 1990, ApJ, 349, 57

Hoare, M. G., S. E. Kurtz, S. Lizano, E. Keto, & P. Hofner. 2007, in Protostars and Planets V, ed. B. Reipurth, D. Jewitt, & K. Keil, 181

Hollenbach, D., D. Johnstone, S. Lizano, & F. Shu. 1994, ApJ, 428, 654

Hunt, L., S. Bianchi, & R. Maiolino. 2005, A&A, 434, 849

Hunter, D. A., R. W. O'Connell, J. S. Gallagher, & T. A. Smecker-Hane. 2000, AJ, 120, 2383

Hurt, R. L., K. M. Merrill, I. Gatley, & J. L. Turner. 1993, AJ, 105, 121

Hurt, R. L., J. L. Turner, & P. T. P. Ho. 1996, ApJ, 466, 135

Iodice, E., M. Arnaboldi, M. Rejkuba, M. J. Neeser, L. Greggio, O. A. Gonzalez, M. Irwin, & J. P. Emerson. 2014, A&A, 567, A86

Jaffe, D. T. & J. Martín-Pintado. 1999, ApJ, 520, 162

Johnson, M., D. A. Hunter, S.-H. Oh, H.-X. Zhang, B. Elmegreen, E. Brinks, E. Tollerud, & K. Herrmann. 2012, AJ, 144, 152

Kamann, S., T.-O. Husser, S. Dreizler, E. Emsellem, P. M. Weilbacher, S. Martens, R. Bacon, M. den Brok, B. Giesers, D. Krajnović, M. M. Roth, M. Wendt, & L. Wisotzki. 2018, MNRAS, 473, 5591

Kepley, A. A., L. Chomiuk, K. E. Johnson, W. M. Goss, D. S. Balser, & D. J. Pisano. 2011, ApJ, 739, L24

Kim, J.-G., W.-T. Kim, & E. C. Ostriker. 2016, ApJ, 819, 137

Kobulnicky, H. A., E. D. Skillman, J.-R. Roy, J. R. Walsh, & M. R. Rosa. 1997, ApJ, 477, 679

Kormendy, J. & J. Kennicutt, Robert C. 2004, ARA&A, 42, 603

Kornei, K. A. & N. McCrady. 2009, ApJ, 697, 1180

Krause, M., C. Charbonnel, T. Decressin, G. Meynet, N. Prantzos, & R. Diehl. 2012, A&A, 546, L5

Krause, M. G. H., C. Charbonnel, N. Bastian, & R. Diehl. 2016, A&A, 587, A53

Krieger, N., A. D. Bolatto, F. Walter, A. K. Leroy, L. K. Zschaechner, D. S. Meier, J. Ott, A. Weiss, E. A. C. Mills, R. C. Levy, S. Veilleux, & M. Gorski. 2019, ApJ, 881, 43

Kroupa, P. & C. M. Boily. 2002, MNRAS, 336, 1188

Kroupa, P., C. Weidner, J. Pflamm-Altenburg, I. Thies, J. Dabringhausen, M. Marks, & T. Maschberger. 2013, The Stellar and Sub-Stellar Initial Mass Function of Simple and Composite Populations, ed. T. D. Oswalt & G. Gilmore, 115

Lacy, J. H., D. T. Jaffe, Q. Zhu, M. J. Richter, M. A. Bitner, T. K. Greathouse, K. Volk, T. R. Geballe, & D. M. Mehringer. 2007, ApJ, 658, L45

Lada, C. J. & E. A. Lada. 2003, ARA&A, 41, 57

Lada, C. J., M. Margulis, & D. Dearborn. 1984, ApJ, 285, 141

Lee, Y.-N. & P. Hennebelle. 2016, A&A, 591, A30

Leroy, A. K., A. D. Bolatto, E. C. Ostriker, E. Rosolowsky, F. Walter, S. R. Warren, J. Donovan Meyer, J. Hodge, D. S. Meier, J. Ott, K. Sandstrom, A. Schruba, S. Veilleux, & M. Zwaan. 2015, ApJ, 801, 25

Leroy, A. K., A. D. Bolatto, E. C. Ostriker, F. Walter, M. Gorski, A. Ginsburg, N. Krieger, R. C. Levy, D. S. Meier, E. Mills, J. Ott, E. Rosolowsky, T. A. Thompson, S. Veilleux, & L. K. Zschaechner. 2018, ApJ, 869, 126

Li, Z., J. Shen, & W.-T. Kim. 2015, ApJ, 806, 150

Lizano, S., J. Canto, G. Garay, & D. Hollenbach. 1996, ApJ, 468, 739

López-Sánchez, Á. R., C. Esteban, J. García-Rojas, M. Peimbert, & M. Rodríguez. 2007, ApJ, 656, 168

MacLaren, I., K. M. Richardson, & A. W. Wolfendale. 1988, ApJ, 333, 821

Maffei, P. 1968, PASP, 80, 618

Mangum, J. G., A. G. Ginsburg, C. Henkel, K. M. Menten, S. Aalto, & P. van der Werf. 2019, ApJ, 871, 170

Mapelli, M. 2017, MNRAS, 467, 3255

Marín-Franch, A., A. Aparicio, G. Piotto, A. Rosenberg, B. Chaboyer, A. Sarajedini, M. Siegel, J. Anderson, L. R. Bedin, A. Dotter, M. Hempel, I. King, S. Majewski, A. P. Milone, N. Paust, & I. N. Reid. 2009, ApJ, 694, 1498

Martín-Hernández, N. L., D. Schaerer, & M. Sauvage. 2005, A&A, 429, 449

Matzner, C. D. 2002, ApJ, 566, 302

McLean, I. S., E. E. Becklin, O. Bendiksen, G. Brims, J. Canfield, D. F. Figer, J. R. Graham, J. Hare, F. Lacayanga, J. E. Larkin, S. B. Larson, N. Levenson, N. Magnone, H. Teplitz, & W. Wong. 1998, in Proc. SPIE, Vol. 3354, Infrared Astronomical Instrumentation, ed. A. M. Fowler, 566–578

Meier, D. S. & J. L. Turner. 2012, ApJ, 755, 104

Meier, D. S., J. L. Turner, & S. C. Beck. 2002, AJ, 124, 877

Meier, D. S., J. L. Turner, & R. L. Hurt. 2008, ApJ, 675, 281

Meier, D. S., F. Walter, A. D. Bolatto, A. K. Leroy, J. Ott, E. Rosolowsky, S. Veilleux, S. R. Warren, A. Weiß, M. A. Zwaan, & L. K. Zschaechner. 2015, ApJ, 801, 63

Merritt, D. 2004, in Coevolution of Black Holes and Galaxies, ed. L. C. Ho, 263

Mohan, N. R., K. R. Anantharamaiah, & W. M. Goss. 2002, ApJ, 574, 701

Monreal-Ibero, A., J. M. Vílchez, J. R. Walsh, & C. Muñoz-Tuñón. 2010, A&A, 517, A27

Müller-Sánchez, F., O. González-Martín, J. A. Fernández-Ontiveros, J. A. Acosta-Pulido, & M. A. Prieto. 2010, ApJ, 716, 1166

Oey, M. S., C. N. Herrera, S. Silich, M. Reiter, B. L. James, A. E. Jaskot, & G. Micheva. 2017, ApJ, 849, L1

Oliva, E., L. Origlia, J. K. Kotilainen, & A. F. M. Moorwood. 1995, A&A, 301, 55

Onishi, K., S. Iguchi, K. Sheth, & K. Kohno. 2015, ApJ, 806, 39

Paglione, T. A. D., O. Yam, T. Tosaki, & J. M. Jackson. 2004, ApJ, 611, 835

Pasquali, A., A. Bik, S. Zibetti, N. Ageorges, W. Seifert, W. Brandner, H. W. Rix, M. Jütte, V. Knierim, P. Buschkamp, C. Feiz, H. Gemperlein, A. Germeroth, R. Hofmann, W. Laun, R. Lederer, M. Lehmitz, R. Lenzen, U. Mall, H. Mandel, P. Müller, V. Naranjo, K. Polsterer, A. Quirrenbach, L. Schäffner, C. Storz, & P. Weiser. 2011, AJ, 141, 132

Peng, R., S. Zhou, J. B. Whiteoak, K. Y. Lo, & E. C. Sutton. 1996, ApJ, 470, 821

Persson, S. E., T. R. Geballe, P. J. McGregor, S. Edwards, & C. J. Lonsdale. 1984, ApJ, 286, 289

Petts, J. A. & A. Gualandris. 2017, MNRAS, 467, 3775

Piotto, G., A. P. Milone, L. R. Bedin, J. Anderson, I. R. King, A. F. Marino, D. Nardiello, A. Aparicio, B. Barbuy, A. Bellini, T. M. Brown, S. Cassisi, A. M. Cool, A. Cunial, E. Dalessandro, F. D'Antona, F. R. Ferraro, S. Hidalgo, B. Lanzoni, M. Monelli, S. Ortolani, A. Renzini, M. Salaris, A. Sarajedini, R. P. van der Marel, E. Vesperini, & M. Zoccali. 2015, AJ, 149, 91

Portegies Zwart, S. F., S. L. W. McMillan, & M. Gieles. 2010, ARA&A, 48, 431

Regan, M. W. & P. Teuben. 2003, ApJ, 582, 723

Rekola, R., M. G. Richer, M. L. McCall, M. J. Valtonen, J. K. Kotilainen, & C. Flynn. 2005, MNRAS, 361, 330

Renaud, F., F. Bournaud, E. Emsellem, B. Elmegreen, R. Teyssier, J. Alves, D. Chapon, F. Combes, A. Dekel, J. Gabor, P. Hennebelle, & K. Kraljic. 2013, MNRAS, 436, 1836

Renzini, A. 2013, , 84, 162

Rieke, G. H. & M. J. Lebofsky. 1985, ApJ, 288, 618

Rigliaco, E., B. Wilking, M. R. Meyer, R. D. Jeffries, M. Cottaar, A. Frasca, N. J. Wright, A. Bayo, R. Bonito, F. Damiani, R. J. Jackson, F. Jiménez-Esteban, V. M. Kalari, A. Klutsch, A. C. Lanzafame, G. Sacco, G. Gilmore, S. Randich, E. J. Alfaro, A. Bragaglia, M. T. Costado, E. Franciosini, C. Lardo, L. Monaco, L. Morbidelli, L. Prisinzano, S. G. Sousa, & S. Zaggia. 2016, A&A, 588, A123

Robichaud, F., D. Williamson, H. Martel, D. Kawata, & S. L. Ellison. 2017, MNRAS, 469, 3722

Rodríguez-Rico, C. A., W. M. Goss, J. L. Turner, & Y. Gómez. 2007, ApJ, 670, 295

Rodríguez-Rico, C. A., W. M. Goss, J.-H. Zhao, Y. Gómez, & K. R. Anantharamaiah. 2006, ApJ, 644, 914

Rosenberg, M. J. F., P. P. van der Werf, & F. P. Israel. 2013, A&A, 550, A12

Sakai, S., L. Ferrarese, R. C. Kennicutt, Jr., & A. Saha. 2004, ApJ, 608, 42

Sakamoto, K., P. T. P. Ho, D. Iono, E. R. Keto, R.-Q. Mao, S. Matsushita, A. B. Peck, M. C. Wiedner, D. J. Wilner, & J.-H. Zhao. 2006, ApJ, 636, 685

Schaerer, D., T. Contini, D. Kunth, & G. Meynet. 1997, ApJ, 481, L75

Scoville, N. Z., B. T. Soifer, G. Neugebauer, J. S. Young, K. Matthews, & J. Yerka. 1985, ApJ, 289, 129

Seo, W.-Y., W.-T. Kim, S. Kwak, P.-Y. Hsieh, C. Han, & P. F. Hopkins. 2019, ApJ, 872, 5

Sewilo, M., E. Churchwell, S. Kurtz, W. M. Goss, & P. Hofner. 2004a, ApJ, 605, 285

—. 2004b, ApJ, 605, 285

Shlosman, I. 2002, arXiv e-prints, astro

Silich, S. & G. Tenorio-Tagle. 2017, MNRAS, 465, 1375

—. 2018, MNRAS, 478, 5112

Silich, S., G. Tenorio-Tagle, S. Martínez-González, & J. Turner. 2020, MNRAS, 494, 97

Silich, S., G. Tenorio-Tagle, & C. Muñoz-Tuñón. 2003, ApJ, 590, 791

Silich, S., G. Tenorio-Tagle, & A. Rodríguez-González. 2004, ApJ, 610, 226

Smith, L. J., V. Bajaj, J. Ryon, & E. Sabbi. 2020, arXiv e-prints, arXiv:2004.14976

Smith, L. J., P. A. Crowther, D. Calzetti, & F. Sidoli. 2016, ApJ, 823, 38

Smith, R., S. Goodwin, M. Fellhauer, & P. Assmann. 2013, MNRAS, 428, 1303

Sormani, M. C., E. Sobacchi, F. Fragkoudi, M. Ridley, R. G. Treß, S. C. O. Glover, & R. S. Klessen. 2018, MNRAS, 481, 2

Stolte, A., B. Hußmann, C. Olczak, W. Brandner, M. Habibi, A. M. Ghez, M. R. Morris, J. R. Lu, W. I. Clarkson, & J. Anderson. 2015, A&A, 578, A4

Strickland, D. K., T. M. Heckman, K. A. Weaver, C. G. Hoopes, & M. Dahlem. 2002, ApJ, 568, 689

Taylor, C. L., S. Hüttemeister, U. Klein, & A. Greve. 1999, A&A, 349, 424

Tenorio-Tagle, G. 1979, A&A, 71, 59

Tenorio-Tagle, G., C. Muñoz-Tuñón, S. Silich, & S. Cassisi. 2015, ApJ, 814, L8

Tenorio-Tagle, G., S. Silich, S. Martínez-González, C. Muñoz-Tuñón, J. Palouš, & R. Wünsch. 2013, ApJ, 778, 159

Tokunaga, A. T. 2000, Infrared Astronomy, ed. A. N. Cox, 143

Tokura, D., T. Onaka, H. Takahashi, T. Miyata, S. Sako, M. Honda, Y. Okada, I. Sakon, Y. Y. Tajiri, H. Kataza, Y. K. Okamoto, T. Yamashita, & T. Fujiyoshi. 2006, ApJ, 648, 355

Tsai, C.-W., J. L. Turner, S. C. Beck, L. P. Crosthwaite, P. T. P. Ho, & D. S. Meier. 2006, AJ, 132, 2383

Tsai, C.-W., J. L. Turner, S. C. Beck, D. S. Meier, & S. A. Wright. 2013, ApJ, 776, 70

Turner, J. L. 2009, Astrophysics and Space Science Proceedings, 10, 215

Turner, J. L. & S. C. Beck. 2004, ApJ, 602, L85

Turner, J. L., S. C. Beck, D. J. Benford, S. M. Consiglio, P. T. P. Ho, A. Kovács, D. S. Meier, & J.-H. Zhao. 2015, Nature, 519, 331

Turner, J. L., S. C. Beck, L. P. Crosthwaite, J. E. Larkin, I. S. McLean, & D. S. Meier. 2003, Nature, 423, 621

Turner, J. L., S. C. Beck, & P. T. P. Ho. 2000, ApJ, 532, L109

Turner, J. L., S. M. Consiglio, S. C. Beck, W. M. Goss, P. T. P. Ho, D. S. Meier, S. Silich, & J.-H. Zhao. 2017, ApJ, 846, 73

Turner, J. L. & P. T. P. Ho. 1983, ApJ, 268, L79

—. 1985, ApJ, 299, L77

—. 1994, ApJ, 421, 122

Turner, J. L., P. T. P. Ho, & S. C. Beck. 1998, AJ, 116, 1212

Ulvestad, J. S. & R. R. J. Antonucci. 1997, ApJ, 488, 621

Vanzi, L. & M. Sauvage. 2004, A&A, 415, 509

Veilleux, S., G. Cecil, & J. Bland-Hawthorn. 2005, ARA&A, 43, 769

Waller, W. H. 1991, ApJ, 370, 144

Walsh, J. R. & J.-R. Roy. 1989, MNRAS, 239, 297

Walter, F., A. D. Bolatto, A. K. Leroy, S. Veilleux, S. R. Warren, J. Hodge, R. C. Levy, D. S. Meier, E. C. Ostriker, J. Ott, E. Rosolowsky, N. Scoville, A. Weiss, L. Zschaechner, & M. Zwaan. 2017, ApJ, 835, 265

Watson, A. M., J. S. Gallagher, III, J. A. Holtzman, J. J. Hester, J. R. Mould, G. E. Ballester, C. J. Burrows, S. Casertano, J. T. Clarke, D. Crisp, R. Evans, R. E. Griffiths, J. G. Hoessel, P. A. Scowen, K. R. Stapelfeldt, J. T. Trauger, & J. A. Westphal. 1996, AJ, 112, 534

Weaver, K. A., T. M. Heckman, D. K. Strickland, & M. Dahlem. 2002, ApJ, 576, L19

Westmoquette, M. S., B. James, A. Monreal-Ibero, & J. R. Walsh. 2013, A&A, 550, A88

Westmoquette, M. S., L. J. Smith, J. S. Gallagher, & K. M. Exter. 2007, MNRAS, 381, 913

Westmoquette, M. S., L. J. Smith, & J. S. Gallagher, III. 2011, MNRAS, 414, 3719

Wood, C. M., C. A. Tremonti, D. Calzetti, C. Leitherer, J. Chisholm, & J. S. Gallagher. 2015, MNRAS, 452, 2712

Wood, D. O. S. & E. Churchwell. 1989, ApJS, 69, 831

Wu, P.-F., R. B. Tully, L. Rizzi, A. E. Dolphin, B. A. Jacobs, & I. D. Karachentsev. 2014, AJ, 148, 7

Wünsch, R., J. Palouš, G. Tenorio-Tagle, & S. Ehlerová. 2017, ApJ, 835, 60